

Dynamical Evolution of Star Clusters
with Many Primordial Binaries

Ataru Tanikawa

November 25, 2008

Contents

| | | |
|----------|---|-----------|
| 1 | Introduction | 9 |
| 1.1 | Clusters with primordial binaries | 12 |
| 1.2 | N -body simulation of a star cluster | 15 |
| 1.3 | This thesis | 17 |
| 2 | A New Code GORILLA | 23 |
| 2.1 | Basic concept | 23 |
| 2.2 | Basic algorithm | 25 |
| 2.3 | How to use GORIMO | 29 |
| 2.4 | Test simulation | 32 |
| 2.5 | Reliability | 32 |
| 2.5.1 | Generation process of large energy error | 32 |
| 2.5.2 | Optimal criteria of isolation | 36 |
| 2.5.3 | Influence of energy error on structural parameters | 37 |
| 2.6 | Comparison with other codes | 38 |
| 3 | Effect of Hardness of Primordial Binaries on Evolution of Star Clusters | 59 |
| 3.1 | Simulation methods | 59 |
| 3.2 | Core evolution and binary properties | 60 |
| 3.3 | Interpretation | 63 |
| 3.3.1 | Soft range | 64 |
| 3.3.2 | Intermediate hard range | 64 |
| 3.3.3 | Super hard range | 65 |
| 3.4 | Comparison of core size between theoretical estimate and simulation results | 65 |
| 3.4.1 | Theoretical formula | 65 |
| 3.4.2 | Instant of halt of core contraction | 70 |
| 3.4.3 | After halt of core contraction | 71 |
| 3.5 | The initial mass fraction of the primordial binaries | 73 |
| 3.6 | Comparison with previous studies | 74 |
| 3.7 | High-velocity escapers | 74 |

| | | |
|----------|--|------------|
| 4 | Example of Application to Astrophysics: Estimate of Double Neutron Star Merger Rate | 103 |
| 4.1 | Evolution of neutron stars in globular clusters | 103 |
| 4.2 | Previous works on DNS merger rate | 103 |
| 4.3 | Our model for DNS evolution | 105 |
| 4.4 | Results | 106 |
| 4.5 | Comparison with previous works | 107 |
| 5 | Summary | 109 |
| A | Algorithm of GORILLA | 111 |
| A.1 | Time integrator part | 111 |
| A.2 | GORIMO | 113 |

Abstract

The dynamical evolution of globular clusters is complicated even if all their stars are assumed to be single stars. The presence of primordial binaries in the globular clusters further complicates their evolution. Regardless of many parameters of the primordial binaries, such as mass fraction, binding energy distribution, and eccentricity distribution, the dependence of the cluster evolutions on these parameters is not investigated, except the mass fraction until now.

In this thesis, I investigate the dependence of the cluster evolutions and population of escapers on the distribution of the binding energies of the primordial binaries. Since the hardening and heating rate of the binaries greatly depends on their binding energies, the hardness of the binaries affects the core size at and after the halt of the core contraction, and population of the escapers.

By means of N -body simulations, I systematically investigate the dynamical evolution of star clusters with primordial binaries whose initial mass fractions, $f_{b,0}$, are different, and whose initial distributions of binding energies are different. I set initial mass fraction $f_{b,0} = 0.03, 0.01, 0.3$, and the initial distributions of the binding energies to be δ functions, $\delta(x - E_{b,0})(E_{b,0}) = 1, 3, 10, 30, 100, 300kT_0$, where $E_{bin,0}$ is the binding energy of the binaries at the initial time, and $1.5kT_0$ is the stellar average kinetic energy in the cluster at the initial time.

In $f_{b,0} = 0.1$, I find that in both soft ($E_{bin,0} = 1kT_0$, and $3kT_0$) and hard ($E_{bin,0} = 300kT_0$) hardness, the clusters experiences deep core collapse. On the other hand, in $E_{bin,0} = 10kT_0, 30kT_0$, and $100kT_0$, core collapse stops halfway. Deep core collapse in the $E_{bin,0} = 1kT_0$ and $3kT_0$ models is due to the fact that the primordial binaries are destroyed, and can generate no or not enough energy heating the core. Deep core collapse in the $E_{bin,0} = 300kT_0$ model is due to the fact that single stars and binaries heated by binary-single and binary-binary encounters are ejected from the cluster, and carry away the energy generated by the binaries.

In $f_{b,0} = 0.3$, core collapse of the cluster with $E_{bin,0} = 3kT_0$ stops halfway. Each binary with $E_{b,0} = 3kT_0$ generates small energy, however, the sum of the energy generated by the $3kT_0$ binaries is sufficient for the halfway halt of core collapse, if $f_{b,0} \geq 0.3$.

Furthermore, I estimate a double-neutron-star merger rate in one globular cluster using my simulation results. The merger rate has little dependence on the distribution of the binding energies of the primordial binaries, and is

limited by the number of neutron stars retained by the globular clusters. From my estimate, 200 double neutron stars which merge within a Hubble time are formed in one globular cluster. Since 150 globular clusters are in our Galaxy, 3×10^4 double neutron stars merge within a Hubble time in our Galaxy, which is comparable to Kim et al. (2005)'s estimate which is 15 per 10^6 years in our Galaxy.

I perform the above N -body simulations by means of a new N -body simulation code equipped with special treatments for binaries. The name is GORILLA. In GORILLA, we approximate the internal motions of two particles isolated enough from the other particles as two-body motions. We can separate the part of the special treatment for the binaries as a module from GORILLA. I call the module for the special treatment for the binaries, GORIMO (GORilla MOdule). By means of GORILLA, we can follow the dynamical evolution of clusters after gravothermal core collapse oscillations within energy error $\sim 1\%$ in almost all case. Sometimes, long-lived hierarchical triple systems appear. The integrations of their orbits generate large energy errors, and the total energy errors exceed 1% .

Acknowledgement

I am grateful for Dr. Fukushige, at K & F Computing Research, to suggest theme of this investigation, set a plan of investigation, and help writing this thesis. He suggested the basic idea of GORILLA, which are my N -body simulation code for star clusters. When I developed GORILLA, he advised me about the algorithm of GORILLA. For the purpose of test of GORIMO, he give me sticky8, which is his time integrator. He spent his precious time improving my thesis. He also supported me mentally. When I lost my confidence about my ability for research, he gave spurs to me.

I am also grateful for Prof. Makino, at National Astronomical Observatory of Japan, for many helpful advices. He advised me about the consistent explanation of the core evolution in my simulations with the theoretical estimates, and the estimate of double-neutron-star merger rate. Furthermore, he improved the quality of my presentation at International Astronomical Union Symposium 246.

I would like to thank for Prof. Hachisu, at University of Tokyo, not only to help my investigation and give me advice in astro colloquium but also to deal with troublesome procedure about my interim, and my thesis.

This thesis is completed owing to the support of many people. I am thankful for Mr. Ishiyama to work for GRAPE-6A cluster. He constructed my file server and backup server. I am also thankful for Ms. Hisaga to deal with many affairs. Special thanks to Prof. Daisaka, and Dr. Sekiguchi, who encouraged me so tired from this work. Japan Society for the Promotion of Science support me financially. My parents help me not only financially but also mentally.

Finally, I thank many people for setting the enjoyable environment for my research life, and list their names: Yoko Funato, Hideki Yahagi, Junko Daisaka, Hidenori Matsui, and Masaki Iwasawa, Keigo Nitadori, Michiko Fujii, Kuniaki Koike, Takahiko Senuma, Sangyong An, Yusuke Tsukamoto, Shoichi Oshino, Seiji Harikae, and Nobuhisa Kakurai.

Chapter 1

Introduction

Globular clusters consist of about 10^5 stars, distributed almost spherically. In our Galaxy, about 150 globular clusters are observed not only in the disk, but also in the halo. The globular clusters are observed in any type of galaxy, such as ellipticals, spirals, and irregulars, with wide variety of its specific frequency, S_N , the number of the globular clusters per unit galaxy luminosity (e.g. Harris 2001).

The globular clusters are well modelled as self-gravitational many-body systems which consist of only point-mass particles. This is because most masses of the globular clusters consist of those of stars. The mass-to-light ratios of the globular clusters are about 2 in the units of M_\odot/L_\odot , where M_\odot and L_\odot are, respectively, solar mass and solar luminosity (Harris 1996), and those of the main-sequence stars in the globular clusters is also about 2. The masses of such stars are less than $0.8M_\odot$, since the ages of the globular clusters are more than 10^{10} years. The sizes of the stars are much smaller than those of the globular clusters by about 8 order of magnitudes. Assuming that the mass of each star is $0.8M_\odot$, its radius is about 0.004AU . On the other hand, the typical sizes of the globular clusters, such as their half-mass radii, are about $1 - 10\text{pc}$ (Harris 1996).

During 10^6 years, the globular clusters are likely to be in dynamical equilibrium. The dynamical equilibrium is defined as the situation where globular clusters keep their gravitational potentials steady, while individual stars are orbiting. Assuming that the distributions of surface brightness of the globular clusters reflect their mass distributions, their mass distributions can be well fitted to theoretical cluster models in dynamical equilibrium (e.g. King 1966). The velocity distributions of the globular clusters are also in good agreement with those of the models (e.g. Gunn, Griffin 1979).

On much longer timescale, the globular clusters never stay in the dynamical equilibrium. The orbital energies of the stars, i.e. the sum of their kinetic and potential energies, fairly change due to a series of two-body interactions with other stars. This process is called two-body relaxation. Typical two-body relaxation timescale in the globular clusters are about $10^8 - 10^9$ years, which

are sufficiently smaller than the ages of the globular clusters (10^{10} years). The typical two-body relaxation time is usually represented by half-mass relaxation time, which is two-body relaxation time at a half-mass radius, expressed as

$$t_{\text{rh}} = \frac{0.138M^{1/2}r_{\text{h}}^{3/2}}{G^{1/2}\bar{m}\log(0.4N)}, \quad (1.1)$$

where G is the gravitational constant, M is the total mass of a cluster, N is its total number of stars, r_{h} is its half-mass radius, and \bar{m} is the average mass of its stars (Spitzer 1987).

The dynamical evolutions of clusters are one of interesting topics in terms of the nonexistence of thermodynamical equilibrium. Since velocity dispersions in the clusters usually increase inward, energy flows outward through two-body relaxation. Then, the velocity dispersions in inner regions of the clusters decrease, and the inner regions contract. Vice versa in outer regions of the clusters. When the inner regions contract and become sufficiently dense, cores of the clusters by itself become self-gravitational systems. Such cores contract, and the velocity dispersions in the cores increase, when energy flows outward from the cores. Since the increase of the velocity dispersions in the cores lead to further energy outflow, runaway contractions of the cores occur. Such runaway process is called gravothermal core collapse (Antonov 1962; Lynden-Bell, Wood 1968; Hachisu, Sugimoto 1978).

On the course of the gravothermal core collapse, encounters among three single stars become rapidly frequent at a given density. This is because the rate of the encounters depends on cube of number density, whereas the rate of two-body encounters depends on square of number density. Through such an encounter, one star carries away energy, and the remaining stars compose a binary (Aarseth 1971). The binary is called three-body binary.

The three-body binaries further complicate the dynamical evolutions of the clusters. Despite of the small number of the three-body binaries, they may affect the dynamical evolutions of whole clusters, since one binary can provide energy for the surrounding stars infinitely in principle (Heggie 1975). On average, hard binaries become harder through the interactions with the surrounding stars, and consequently the surrounding stars gain energy, where hard and soft binaries have the binding energy more and less than the kinetic energy of the surrounding stars, respectively. The hardening rate of the hard binaries keeps constant, even if they are infinitely hard. The hardening of the hard binaries per one interaction is proportional to their binding energies, and the rate of the interactions is inversely proportional to their binding energies. Both are canceled.

The binaries in the collapsing core interact with the surrounding stars. Consequently, the surrounding stars gain energy, and spread their energy all over the core. When such energy exceeds the energy which flows outward from the core, the gravothermal core collapse stops. Hénon (1975) first demonstrated this process by means of Monte Carlo simulation, although he introduced artificial energy sources in the cluster center. The orbital interaction of binaries can not be solved by its method. The reason why he considered such energy

source as binaries is that binaries are found in the center of the clusters after core contraction by N -body simulations at that time (Aarseth 1971; Aarseth 1975; Wielen 1974; Wielen 1975).

The dynamical evolution of the core is not finished. The core expands, and the velocity dispersion in the core becomes lower than its surroundings, when the energy generated by the binaries exceeds the energy outflowing from the core. The energy flows from the surroundings to the core, and the core furthermore expands. This is the opposite mechanism to the gravothermal core collapse. The core stops expanding, and shrinks again when the core expansion does not increase the energy of the core due to low energy of its surrounding stars. This is called gravothermal oscillations, and was first shown by Sugimoto and Bettwieser (1983), and Bettwieser and Sugimoto (1984) by means of gas model simulations. The gravothermal oscillation is demonstrated by the other methods (Fokker-Planck simulations by Cohn et al. 1989; N -body simulations by Makino 1996).

The dynamical evolutions of clusters with primordial binaries are greatly different from those of the clusters without primordial binaries. Previous studies showed that the cores of the clusters with primordial binaries stop contracting before the onset of the gravothermal core collapse. The core radii at the halt of the core contraction are larger than those of the clusters without primordial binaries at the halt of the gravothermal core collapse by order of magnitudes as reviewed in detail in section 1.1. Many primordial binaries provide the stars in the core with enough energy to stop the core contraction, even when the densities of the cores are comparatively low. The amount of energy generated by the primordial binaries is proportional to the sum of the product of the densities of single stars and the binaries, and the square of the density of the binaries, compared with the amount of energy generated by the three-body binaries which is proportional to the cube of the density of single stars.

The clusters with primordial binaries are possible. It is likely that the globular clusters contain primordial binaries. Many binaries are observed in the solar neighborhood (e.g. α Canis Majoris; α Canis Minoris; α Scorpii). Since the stars in the solar neighborhood rarely interact with each other, most of binaries are considered not to be formed dynamically, but to be formed at the moment of star formation. Such primordial binaries may be formed also in the globular clusters.

For following the dynamical evolution of a star cluster with binaries, N -body simulation is the most powerful method. This is because the N -body simulation has the least number of approximations. For the N -body simulations, we need codes with the special treatment of binaries. If we perform N -body simulations naively without any treatment, we have to spend most time calculating the orbits of the binaries, and lose the accuracy of the orbits of the binaries. This is because the periods of binaries are smaller than the dynamical time of typical star in these clusters by several order of magnitudes, and the sizes of binaries are also smaller than those of these clusters by several order of magnitudes.

Two codes equipped with the special treatments of binaries are published, which are NBODY4 (e.g. Aarseth 2003), and kira (e.g. McMillan, Hut 1996;

Portegies Zwart et al. 2001). However, as described in detail in section 1.2, these published codes are complicated in the treatments. It is hard for other than the developers to refine these codes for dealing with unique troubles in their studies. The helps of the developers are vital.

In this thesis work, I describe a new N -body simulation code with simpler treatments for binaries, which I call GORILLA. In section 1.2, I review the merits and difficulty of N -body simulations, and describe how the published codes keep the advantages of N -body simulation, and overcome its difficulty. In the first half of section 1.3, I analyze the reason for the complications of the published codes, and describe how I develop my simpler code based on the analysis.

The purpose of this thesis work is to investigate one of the dependences of the dynamical evolutions of the clusters on many parameters of primordial binaries by means of GORILLA. We have to set the parameters of primordial binaries for the initial conditions of the clusters. However, previous studies cover only a part of the dependences of the dynamical evolutions of the clusters on these parameters. In section 1.1, I review previous studies on the dynamical evolutions of clusters with primordial binaries. In the last half of section 1.3, I point out the dependences that remain to be investigated, and describe the dependence I investigate.

1.1 Clusters with primordial binaries

Spitzer and Mathieu (1980) pioneered the studies of the dynamical evolution of clusters with primordial binaries. They performed Monte Carlo simulations. They showed that the time when gravothermal core collapse stops is more delayed in these clusters than in the clusters without primordial binaries, and the depths of their core collapse are the same as those of clusters without primordial binaries. The simulations have not extended further (e.g. chapter 7 in Spitzer 1987).

In 1980s, the evolutions of clusters with primordial binaries have been studied by means of N -body simulations, although the number of particles is small (< 500). Aarseth (1980) has treated the clusters with $N = 250$, and with 8 primordial binaries. Giannone and Molteni (1985) has treated the clusters with $N = 300$, and with 60 primordial binaries. Leonard and Duncan (1988; 1990) have performed the clusters with $N = 45$, and with 15 primordial binaries. The difference between the clusters and clusters without primordial binaries is not distinct.

Goodman and Hut (1989) (hereafter GH89) first showed theoretical estimates that the core of the cluster with primordial binaries at the halt of core contraction is larger than that of the cluster without primordial binaries by order of magnitudes. Their theoretical estimates is based on the model that the cluster core stop contracting when energy generated by the primordial binaries is balanced with energy outflowing from the inner region of the cluster to the outer region. Here, the core is assumed to be gravothermally stable.

The primordial binaries generate enough energy to stop the core contraction even if the core radius is relatively large, i.e. the number density at the cluster center, around which most interactions between binaries and single stars, and two binaries occur, is relatively small. This is because, in the cluster with the primordial binaries, the rate of the energy generation is proportional to the sum of product of the central number densities of single stars and binaries, and square of the central number density of the binaries. On the other hand, in the cluster without the primordial binaries, the rate is proportional to cube of the central number density of the single stars, since only three-body binaries generate energy.

McMillan et al. (1990; 1991) first performed N -body simulations of clusters with primordial binaries in which the number of particles is more than 1000. The mass fraction of the primordial binaries is about 20 %. Due to its large number of particles, they can clearly show that the cluster cores stop contracting at the larger cores than those without primordial binaries. Binary-binary encounters largely contributed to the energy generated from binaries after the halts of core contractions, since the binaries occupy the cluster center due to mass segregation. The binaries is depleted through the binary-binary encounters.

By means of Fokker-Planck simulations, Gao et al. (1991) investigated the dynamical evolutions of clusters with primordial binaries. The clusters have 3×10^5 particles including 3×10^4 primordial binaries. They showed that the cluster cores slowly contract after rapid core contraction, not stop contracting. The gravothermal oscillations occur, after the slow core contraction continues for a long time, about several ten half-mass relaxation times. The large number of particles enables their simulations to show the gravothermal oscillations. The results of their simulations become standard other than N -body simulations (Giersz, Spurzem 2000; Fregeau et al. 2003).

Heggie and Aarseth (1992) performed N -body simulations of clusters with 2000 particles that contain 6 or 12 % primordial binaries in mass. They made clear the reason for the difference of the rates of the above core contractions. The rapid core contraction occurs due to energy outflow from the inner region of the cluster to the outer region. On the other hand, the slow core contraction is due to the depletion of the primordial binaries. The smaller number of the binaries has to generate enough energy to be balanced with the energy loss due to the escape of stars, so that the mass density at the cluster center increases.

The above studies investigate difference of the dynamical evolutions between clusters with and without primordial binaries. Hereafter, I review previous studies focusing on the dynamical evolutions of clusters with primordial binaries that have different initial conditions.

Aarseth and Heggie (1993) performed N -body simulations of clusters with 4000 particles that have mass spectrum. The core radius of the cluster at the halt of the core contraction is smaller than those of clusters with equal-mass stars. This is because the binaries in the cluster are less concentrated than those in the clusters with equal-mass stars. If single stars have larger mass than binaries, the single stars more preferentially fall into the cluster center than the binaries.

Vesperini and Chernoff (1994) (hereafter VC94) investigated the dependence of core radii at the halt of core contraction on the core mass fraction of primordial binaries and the distribution of the binding energies of the binaries. Their theoretical estimates are based on those of GH89. They refined the model of GH89, adding the dependence of energy generated from the binaries on their binding energies as follows. As the binding energies become larger (or smaller), the binaries are easier to generate (or absorb) energy. The boundary between large and small binding energies is $1.5kT_c$, where $1.5kT_c$ is the average kinetic energy of single stars in the core. Since binaries with larger binding energies generate more energy, single stars or binaries themselves involved with encounters immediately are ejected from the cluster before they give other stars energy. This critical binding energy is about $100kT_c$, which is derived from the escape energy from the cluster center, and the amount of energy generated from binaries per one encounter.

They set the core mass fraction to be 0 – 60 %, the distribution function to be $f(E_{\text{bin}}) \propto E_{\text{bin}}^{n-2}$ ($n = 0, 1, 2$), the upper limit to be $30 - 250kT_c$, and the lower limit to be $5 - 15kT_c$. When the core mass fraction is 10 %, and the upper and lower limits are, respectively, $10kT_c$ and $100kT_c$ in the binding energy distribution $n = 1$, the core radius is larger than that of the cluster without primordial binaries by order of magnitudes. When they change the core mass fraction to 60 %, and fix the other parameters, the core radius increases by a factor of three. When they change the upper and lower limit as above, respectively, the core radii changes only in the range of several ten %. When they change the binding energy distribution, the core radii are rarely different.

Heggie et al. (2006) made clear the dependence of the dynamical evolutions of clusters with primordial binaries on the mass fraction in the whole clusters by means of N -body simulations. The clusters have 4000 particles that contain 0 – 100 % primordial binaries in mass. Some clusters have more than ten thousands, but the clusters contain only 0 and 20 % primordial binaries. When clusters contain more than 20 % primordial binaries in mass, the core radii at the halt of core contraction hardly depends on the mass fraction of the primordial binaries. The core mass fraction of the primordial binaries are not significantly different among the cluster models, since the binaries become more concentrated than at the initial time due to mass segregation.

I summarize the previous studies about the evolutions of clusters with primordial binaries. The core radii of clusters with primordial binaries at the halt of rapid core contraction are larger than those of clusters without primordial binaries at the halt of the gravothermal core collapse by order of magnitudes. Then, the core slowly contracts, and gravothermal oscillations follow.

The core radii at the halt of the rapid core contraction depends on the core mass fraction of primordial binaries, however they weakly depends on the mass fraction in the whole cluster when the mass fraction is more than 20 %. The distribution of the binding energy of primordial binaries slightly affect the core radii at the halt of the rapid core contraction. Stellar mass spectrum makes core radii at the halt of the rapid core contraction smaller.

1.2 N -body simulation of a star cluster

In clusters, each particle obey the equation of motion as follows:

$$m_i \frac{d^2 \mathbf{r}_i}{dt^2} = - \sum_{j \neq i}^N G m_i m_j \frac{\mathbf{r}_i - \mathbf{r}_j}{|\mathbf{r}_i - \mathbf{r}_j|^3} \quad (i = 1, 2, \dots, N), \quad (1.2)$$

where t is time, G is the gravitational constant, N is the number of the particles, \mathbf{r}_i and \mathbf{r}_j are, respectively, the positions of i -th and j -th particles, and m_i and m_j are, respectively, the masses of i -th and j -th particle. In N -body simulations, equation (1.2) is directly solved. N -body simulations have the least assumptions.

In other than N -body simulation, the orbits of particles (or superparticles represented by groups of particles) are approximated as follows. At a given time, cluster potential is calculated by assuming that its potential is spherically symmetric. During two-body relaxation time, the particles are orbiting in the cluster potential fixed. Just one time, the particles are deflected by perturbation as which two-body relaxation is modelled. Cluster potential is calculated again in the same way as above.

The energy generated from primordial binaries is approximated in the following two methods. First one (Gao et al. 1991; Giersz, Spurzem 2000; Fregeau et al. 2003) uses cross section of binary-single encounters as a function of generated energy, which based on previous three-body scattering experiments, and total cross section of binary-binary encounters and the average generated energy per one encounter. These cross section depends on local density and velocity dispersion. The generated energy is derived from these cross section and Monte Carlo methods. Second one (Giersz, Spurzem 2003; Fregeau, Rasio 2006) decides whether binary-single and binary-binary encounters occur, using their total cross sections. When these encounters occurs, the generated energy is derived from direction integration of three-body and four-body scattering experiments.

N -body simulations are very hard due to the absence of the approximation, such as the above. N -body simulations have the following three difficulties.

The first difficulty is the large calculation cost of gravitation. Equation (1.2) is calculated for each particle per about its dynamical time. The calculation cost is order of N^2 . In the approximate methods, potential of each particle is calculated per about two-body relaxation time of the cluster. The calculation cost of all the potentials is order of N . Potential of each particle is determined by the distance from the cluster center, assuming that particles are distributed spherically.

N -body simulations with the large number of particles require the acceleration of the calculation of gravitation. It is appropriate to use GRAPE (e.g. Makino et al. 2003), which is a special purpose computer for accelerating the calculation of gravitation, or to parallelize the calculation of gravitation. Among N -body simulations in which the dynamical evolutions of clusters are followed during $\sim 10^{10}$ years, the largest number of particles is $\sim 10^5$. All the N -body

simulations use GRAPE (e.g. Baumgardt, Makino 2003; Baumgardt et al. 2004; Baumgardt et al. 2005; Shara, Hurley 2006).

The second difficulty is the large deflections of the orbits of particles through close encounters. The timescale on which the accelerations of particles change during the close encounters is sometimes smaller than that at the usual time by 8 order of magnitudes. We need skillful time integration scheme, and timestepping schemes. It is commonly performed to combine fourth-order Hermite scheme of individual timestep scheme (Makino, Aarseth 1992) with block timestep scheme (McMillan 1986; Makino 1991b).

In an individual timestep scheme, timestep of each particle may be changed and separately determined. The reason why this scheme is used for N -body simulations of clusters is that the timescale on which the accelerations of particles change has a wide range in every particle.

In a block timestep scheme, all the timesteps are permitted to be power of two. This scheme enables us to calculate the acceleration and its time derivatives of multiple particles. This scheme is useful when GRAPE is used, or the calculation of gravitation is parallelized. In GRAPE, the acceleration of multiple particles is calculated at the same time. In parallelization of the calculation, the number of communication among computers for information of particles that act gravitation is decreased.

Hermite scheme is time integration scheme, and simplifies algorithm that tends to become complicated due to individual timestep scheme. In Hermite scheme, particles keep only their current data, such as their positions, velocities, accelerations, and its time derivatives, for obtaining their data at the next time. However, in Aarseth-type scheme (Aarseth 1963), each particle keep its data also at previous time for the integration of itself. In Runge-Kutta scheme, some particles have to keep their data at previous time for the integration of other particles.

Fourth-order Hermite scheme is commonly used, since the calculation cost at each timestep is believed to be well balanced with the size of its timestep. This is shown by Makino (1991a), although he adopted Aarseth-type scheme for time integration scheme. It has been recently reported that in Hermite scheme, sixth- and eighth-order schemes are more efficient than fourth-order scheme (Nitadori, Makino 2008). So, these higher-order schemes may be replaced with fourth-order scheme in the near future.

The third difficulty is the presence of binaries. The size of the binary, such as its semi-major axis, may be smaller than the size of the cluster by more than 9 order of magnitudes. This is the case where the binary components are contact if they have $0.8M_{\odot}$, i.e. their separation is 0.004AU, and the cluster size is 10pc. In this case, the periods of the binaries are smaller than the dynamical time of the typical particle by about 10 order of magnitudes. If we perform N -body simulations naively, we may follow the orbits of the binary components to an accuracy of at most 7 digits, expressing the positions of particles as double-precision floating-point number. Furthermore, we have to spend most time calculating the orbits of the binary components due to their small periods.

Two published N -body simulation codes, NBODY4 (e.g. Aarseth 2003), and

kira (e.g. McMillan, Hut 1996; Portegies Zwart et al. 2001), deal with the above two problems, in other words, the differences of the sizes and timescales in the following way. I first describe the solution for the difference of the sizes. The coordinates of the binary components are transformed into the coordinates of the center of mass of the binaries, and the relative coordinates between the binary components. Both the coordinates are expressed as double-precision floating-point number. This enables us to follow the orbits of the binary components to an accuracy of at most 16 digits.

Next, I describe the solution for the difference of the timescale. In the above transformation of coordinates, all we need is to device time integration of the relative coordinate between binary components. The timestep of the relative coordinate has to be small, however that of the center of mass of the binary is not necessarily small. The change of the acceleration of the former coordinate is large due to the gravitation between the binary components. On the other hand, that of the latter coordinate is relatively small due to the absence of the gravitation between the binary components. The gravitation between the binary components is much larger than those which other particles act on the binary components.

The calculation cost of the time integration of the relative coordinate between the binary components may be reduced by omitting the calculation of gravitations which other particles act on the binary components. The omission is as follows. We ignore the gravitations of particles whose contributions to the acceleration of the relative coordinate is small. We judge whether the contribution is small or not by comparing the gravitation between the binary components with the gravitations of other particles on the center of mass of the binary.

In NBODY4, the relative motions of the binaries are regularized by various regularization methods, such as Kustaanheimo-Stiefel method (Kustaanheimo, Stiefel 1965). The smoothing orbit by these methods enables the timestep of particles to become large. The smoothing of the orbits is due to the disappearance of singularity where the distance between the binary components is zero.

1.3 This thesis

In this thesis work, I describe an N -body simulation code for a star cluster from scratch, whose name is GORILLA. The reason why I develop this code by myself is that I need a simpler code than the two published codes, and that I want to comprehend the special treatment for the binary by myself.

In the two published codes, the treatments of binaries are most complicated. Among these treatments, for the integration of the relative coordinate between binary components, it is hard to omit the gravitations of particles other than the binary that are sufficiently smaller than the gravitation between the binary components. Usually, the discrimination whether each particle is omitted or not is performed once per multiple timestep. Each binary has to keep the

discrimination.

In the treatment of binaries of GORILLA, the relative motions of relatively isolated binaries are approximated as two-body motions. This corresponds to the omission of the gravitation of all the other particles on the binaries. In other words, there are only two treatments of binaries that the gravitations of all the other particles is considered or not.

In GORILLA, we can separate the part of the special treatment for the binaries as a module from other parts. I call the module GORIMO (GORilla MOdule). If you combine your fourth-order Hermite scheme with individual and block timestep schemes and GORIMO, you can perform N -body simulations of clusters.

The purpose of this thesis work is to investigate one of the dependences of the dynamical evolution of clusters on many parameters of primordial binaries by means of GORILLA.

If we limit equal-mass particles, the population of primordial binaries is characterized by the parameters, such as the mass fraction, and the distributions of the binding energies and eccentricities. All of them are not well-known observationally and theoretically.

However, previous numerical studies only focused the dependence of the mass fraction (Heggie et al. 2006), and did not so the dependence of the distribution of the binding energies. The distribution is usually fixed as uniform in logarithmic scale.

In this thesis, I pay attention to the dependence of the evolution of the cluster core on the distribution of the binding energies of the primordial binaries. I expect that the evolutions of the core are different according to the distribution of the binding energies. This is because the heating rate of the binaries is greatly different between their binding energies. Soft binaries do not heat the clusters due to their destruction through binary-single and binary-binary encounters. Intermediate hard binaries efficiently heat the clusters. Hard binaries do not heat the clusters due to the ejections of themselves and single stars involved by binary-single and binary-binary encounters with the binaries.

I also expect that the population of escapers from the clusters depends on the distribution of the binding energies. As the population of harder binaries is larger, the number of the escapers is larger. This is because single stars and binaries involved by binary-single and binary-binary encounters gain larger energy as the binaries are harder. The population of binary escapers is important for investigating the contribution of the binary escapers to compact binaries on galactic fields. Most binary escapers are hard, since large energy is required for the ejection of the binaries, and the large energy comes only from binary-single and binary-binary encounters involving hard binaries.

VC94 investigated the dependence of the core radii at the halt of core contraction on the distributions of the binding energies of the primordial binaries. However, they did not cover all the distribution of the binding energies of the primordial binaries. According to their model of the amount of energy from the primordial binaries to the cluster, these binaries are divided into three hardness groups. First hardness group is soft binaries ($< 1.5kT_c$) that can not give the

cluster energy due to their destructions. Second hardness group is intermediate hard binaries ($1.5kT_c < E_{\text{bin}} < 100kT_c$) that can give the cluster energy. Third hardness group is super hard binaries ($E_{\text{bin}} > 100kT_c$) that can not give the cluster energy due to their ejections. Their distributions always contain the intermediate hard binaries. This may be the reason why the core radii at the halt of the core contraction weakly depend on the distribution of the binding energy of the primordial binaries.

Furthermore, since VC94 adopted theoretical estimates, they can not follow the evolution of the clusters after the halt of the core contraction. Binary-single and binary-binary encounters after the halt of the core contraction are more frequent than those before the halt of the core contraction due to its higher core density. The distributions of the binding energies of the primordial binaries are greatly changed, and many single stars and binaries are ejected.

I investigate the effect of each hardness group of the primordial binaries on the dynamical evolutions of clusters by means of N -body simulations. For this purpose, I set the distribution functions that consist of the primordial binaries with equal hardness. In other words, these are δ function, $\delta(x - E_{\text{bin},0})$, where $E_{\text{bin},0}$ is the initial binding energies of the primordial binaries. I adopt $E_{\text{bin},0} = 1, 3, 10, 30, 100, 300kT_0$, where $1.5kT_0$ is the average kinetic energy of particles in the whole cluster at the initial time, and $1kT_0$ is about $0.6kT_{c,0}$, where $kT_{c,0}$ is the average kinetic energy of particles in the cluster core at the initial time. I set the mass fraction to be 10 %. Furthermore, I change the mass fraction to 3 and 30 % in $E_{\text{bin},0} = 3, 30, 300kT_0$ cluster models.

By these investigation, we can constrain the range of the variety of the cluster evolutions and population of escapers due to the difference between the distributions of the binding energies. The core evolutions and populations of escapers in clusters with wide distributions of the binding energies of primordial binaries should be intermediate among those of my cluster models with the binding energies $E_{\text{bin},0}$ which sandwich and included in the wide distribution.

All of my cluster models with primordial binaries do not experience the shallower core collapse due to heat generation from the binaries. If clusters have only softer primordial binaries, such as less than $1kT_0$, the binaries will be destroyed at the early phase of evolution. Then, the clusters experience deep core collapse as in the case without primordial binaries. On the other hand, if clusters have only much harder primordial binaries, such as more than $300kT_0$, the clusters will not be heated by released energy of the binaries. This is because the energy released by the binaries is large enough to eject single stars and binaries involved with binary interactions from the cluster. Therefore, the clusters also experience deep core collapse.

After the halt of the core contraction in the clusters with intermediate hard primordial binaries ($E_{\text{bin},0} = 10kT_0, 30kT_0, 100kT_0$), the core radii slightly decrease in $E_{\text{bin},0} = 10kT_0$ and $30kT_0$ models, and is not changed in $E_{\text{bin},0} = 100kT_0$, while the half-mass radii are expanding. The decrease of the ratio of the core radii to the half-mass radii is due to the overall hardening of the binaries. The overall hardening results from the decrease of the average stellar kinetic energy in the clusters due to the energy generated by the primordial

binaries. The slight decrease of the core radii themselves in $E_{\text{bin},0} = 10kT_0$ and $30kT_0$ models is due to the hardening of the primordial binaries through binary-single and binary-binary encounters. This is the first work that shows the relation between the evolution of the core radii and the distribution of the binding energy consistently.

Finally, as one of examples of the applications of my simulation results to astrophysics, I estimate the merger rate of double neutron stars (DNSs) formed in one globular cluster. Mergers of DNSs are important for observations of gravitational wave. Furthermore the DNSs are one of candidates of progenitors of short-gamma ray bursts. The DNS merger rate in the universe may be dominated by DNSs dynamically formed in globular clusters through binary-single and binary-binary encounters involving exchanges between neutron stars and other stars.

Previously, Grindlay et al. (2006) and Ivanova et al. (2008) estimated the DNS merger rates. Grindlay et al. (2006) semi-analytically estimated the DNS merger rate, using a modelled evolution of stellar number density in the cluster center until core collapse, the assumed number of binaries including one neutron star, and cross section of such binaries for encounters with single neutron stars in which the single neutron stars replace the binary component other than the neutron stars, which is derived from three-body scattering experiments. The number of the DNSs merging within a Hubble time is 12 in one post-collapse cluster. Since 40 post-collapse clusters are in our Galaxy, they estimated that 480 DNSs are in our Galaxy.

Ivanova et al. (2008) estimated the DNS merger rate, using a cluster model with fixed stellar number density in the core, modelled mass segregation, and binary-single and binary-binary encounters which occur stochastically obeying assumed cross section. They suggested that 0.2 DNSs which merge within a Hubble time are in one cluster.

It seems that the number of the DNSs is underestimated in both models. Grindlay et al. (2006) assumed that the progenitor of the DNSs is only binaries with one neutron star. However, binaries without neutron stars can be also a progenitor of the DNSs. Since the neutron stars are most massive star in globular clusters, it is highly likely that such binaries become the DNSs after such binaries encounter with single neutron stars two times. The encounters of such binaries with single neutron stars are frequent in the core, since neutron stars are concentrated on the cluster core due to mass segregation.

Ivanova et al. (2008) modelled mass segregation, assuming that the probability of a star with mass m to enter the core after a time t is a Poisson distribution: $p(t) = (1/t_{\text{sc}}) \exp(-t/t_{\text{sc}})$, where t_{sc} is a characteristic mass segregation timescale inversely proportional to m . In this modelling, neutron stars are less concentrated in the core.

When I estimate DNS merger rate, I need to model the motion of neutron stars in clusters, since in my cluster models stars have equal mass, and I can not directly estimate DNS merger rate from my simulation results. Due to mass segregation, only single neutron stars and binaries in the cluster core, where such binaries have any type star. Such binaries become DNS after several encoun-

ters with single neutron stars. Eventually, these DNSs are ejected as a result of binary-single and binary-binary encounters. Since almost these encounters involve neutron stars, almost high-velocity single and binary escapers consist of only neutron stars until the neutron stars in the clusters are completely depleted.

Using the number and binding energy distribution of high-velocity binary escapers in my simulation results, I estimate the number of the DNSs which merge within a Hubble time. Then, the number of the DNSs is 200 in one globular cluster, and subsequently the number of the DNSs is 3×10^4 in our Galaxy, since 150 globular clusters are in our Galaxy. The merger rate is comparable to Kim et al. (2005)'s estimate, 1.5×10^5 , which is based on observations of DNSs in our Galaxy.

The structure of this thesis is as follows. I describe a new simulation code, GORILLA, in section 2. In section 3, I describe my investigation of the effect of the hardness of primordial binaries on the dynamical evolution of clusters. In section 4, I show the example of application of my simulation results to astrophysics: estimate of double neutron star merger rate. I summarize this thesis in section 5.

Chapter 2

A New Code GORILLA

In this section, I describe a new code N -body simulation code named GORILLA, which I develop from scratch. GORILLA is equipped with the special treatment of binaries by which relatively isolated binaries are approximated as two-body motions. In section 2.1, I simply estimate the improvements of the accuracy and efficiency of the N -body simulations owing to the treatment. In section 2.2, I show an algorithm of the treatment, which is incorporated into the fourth-order Hermite scheme with individual and block timestep schemes. I separate the part of the special treatment for the binaries as a module from other parts, and the module part is named GORIMO. In section 2.3, I describe how to combine GORIMO with your codes. In section 2.4, as test simulations of GORILLA, I follow the dynamical evolutions of ten $N = 1024$ clusters without primordial binaries during longer than three core collapse times. The energy errors at the terminal times are $\sim 1\%$ in nine of the ten clusters, and $\sim 10\%$ in one cluster. These energy errors look bad for studies of the cluster cores in which particles have $1 - 10\%$ energy of the clusters. I show the reliability for structural parameters of the clusters in the simulations by means of GORILLA in section 2.5. Finally, I show comparison between simulation results by means of GORILLA, and other N -body simulation codes, i.e. NBODY4, and kira in section 2.6.

2.1 Basic concept

I estimate the improvements of the accuracy and efficiency of N -body simulations owing to the special treatment of binaries. In the special treatment, the relative motions of relatively isolated binaries are approximated as two-body motions.

For this purpose, I consider a relatively simple cluster in which only one binary exists, and is sufficiently isolated from the other stars. I set the standard N -body units (Heggie, Mathieu 1986), such that $G = M = -E = 1$, where M is the total mass of the cluster, E is the energy that the total binding energy of

binaries is excluded from the total energy of the cluster. In this units, the virial radius of the cluster, which can be regarded as typical cluster size, is 1. I set that the cluster consists of $N = 1 \times 10^4$ stars, and the semi-major axis of the binary is 1×10^{-6} . If I transform this units into astronomical units, assuming that all the stars have $1M_{\odot}$, and the semi-major axis of the binary is 0.5AU, the virial radius, and the average velocity dispersion of the cluster are, respectively, 1pc, and 3km/s.

Consider that we perform N -body simulation of the cluster without the special treatment. An energy error from the orbital integration of the binary components dominates those from the orbital integration of the other stars.

The binding energy of the binary, and orbital energies of the stars except the binary components and the center of mass of the binary depend, respectively, on a separation between the binary components, and the distances from the cluster center at which the origin of a coordinate system of the N -body simulation is, where the orbital energies are the sum of kinetic and potential energies of these stars. Even when the positions of the stars are expressed as double-precision floating-point number, the effective digit of the separation between the binary components is only 10, since the semi-major axis of the binary is 10^{-6} , and the typical distance between a star and the cluster center is 1. On the other hand, the effective digits of their distances from the cluster center are 16.

When we integrate all the stars by one timestep, their distances from the cluster center deviate from their true distances by much less than 10^{-8} due to truncation or round off errors. The deviations must be less than 10^{-8} by several order of magnitudes, otherwise it is meaningless to express the positions of the stars as double-precision floating-point number. Since their distances from the cluster center is typically 1, the error of the orbital energy of each star are much less than 10^{-8} in the unit of each orbital energy. On the other hand, the separation between the binary components deviate from the true separation by at least $\sim 10^{-16}$ due to round off error. Since their separation is 10^{-6} , the error of the binding energy is at least 10^{-10} in the unit of the binding energy. The error of the binding energy of the binary grows faster than that of the orbital energy of each star by several order of magnitude at each timestep.

Average timestep of typical single star is a fraction of the dynamical time at the virial radius, ~ 3 , and those of the binary components are a fraction of the binary period, $\sim 10^{-7}$. We assume that both the fractions are equal, and denoted by ϕ . The fraction ϕ depends on the accuracy needed for simulations, and is typically from several tenth part to several hundredth part. The error of the orbital energy of the typical single star is much less than $3/\phi \times 10^{-9}$ in the unit of its orbital energy at each time unit, and the binding energy of the binary is $1/\phi \times 10^{-3}$ in the unit of the binding energy at each time unit, assuming that the errors are systematically accumulated step by step. If the signs of the errors in the orbital energies of all the single stars are the same, which is overestimate, the sum of the errors in the orbital energy of all the single stars is $3/\phi \times 10^{-5}$ in the unit of the total orbital energy.

Since the total orbital energy is -0.25 , the error of the total orbital energy is $8/\phi \times 10^{-6}$ in N -body standard units at each time unit. On the other hand,

since the binding energy of the binary is -0.005 , the error of the binding energy is $5/\phi \times 10^{-6}$ at each time unit.

When we include the special treatment in the N -body simulation of the cluster, we directly integrate not the binary components, but the center of mass of the binary, and analytically solve the relative motion of the binary components as two-body motion. The binding energy of the binary is perfectly conserved, which is a good approximation, since the binary is sufficiently isolated from the other stars. Then, total energy error is the sum of the errors of the orbital energies of the stars other than the binary components, and the center of mass of the binary. These errors grow much more slowly than that of the binding energy of the binary without the special treatment as estimated above. Therefore, the accuracy of the energy conservation increases.

If we again perform N -body simulation of the cluster without the special treatment, we spend most time calculating the motion of the binary. The number of gravitational forces on the binary components that we have to calculate is much larger than the total number of gravitational forces on other stars. The number of gravitational forces on each star at each time unit, n_{gf} , that we have to calculate is estimated as follows:

$$n_{\text{gf}} \sim \frac{N}{\bar{\Delta}t}, \quad (2.1)$$

where $\bar{\Delta}t$ is average timestep of each star during each time unit. In the typical star, $n_{\text{gf}} \sim 3 \times 10^3/\phi$, and in each binary component, $n_{\text{gf}} \sim 1 \times 10^{11}/\phi$. The sum of n_{gf} of all the single stars, whose number is $\sim 10^4$, is $\sim 3 \times 10^7/\phi$, while the sum of n_{gf} of the binary components, whose number is 2, is $\sim 2 \times 10^{11}/\phi$.

We again include the special treatment in the N -body simulation of the cluster. We integrate not the orbit of each binary component, but the orbit of the center of mass of the binary. The average timestep $\bar{\Delta}t$ of the center of mass of the binary is its dynamical time, which is typically the dynamical time at the virial radius, ~ 3 . The number of gravitational forces on the binary components, n_{gf} , decreases to $3 \times 10^3/\phi$. The sum of n_{gf} of all the stars including the binary also decreases from $2 \times 10^{11}/\phi$ to $3 \times 10^7/\phi$, owing to the special treatment.

2.2 Basic algorithm

I describe how to separate the integration of the relative motions of the binaries from that of the other particles. GORILLA consists of time integrator part and GORIMO. The time integrator part solves the equation of motion of individual particles expressed as equation (1.2), using the fourth-order Hermite integration scheme with individual timestep scheme (Makino, Aarseth 1992), and block timestep scheme (McMillan 1986). In the time integrator part, each particle has its own time, t_i , its timestep, Δt_i , its position $\mathbf{r}_i(t_i)$, and so on. Among all the particles, particles with the minimum $t_i + \Delta t_i$ are selected. The number of the selected particles is not always one, since the time integrator part adopts block timestep scheme. The time integrator part evaluates the force and solves

equation (1.2) of the selected particles. The time integrator part are required to send all the particle data to GORIMO at *every block step*, illustrated in figure 2.1.

The procedures of GORIMO are as follows.

- (a) GORIMO searches for two particles isolated enough from the other particles.
- (b) If such two particles (particles k and l) are found, GORIMO transforms the position of the two particles to that of their center of mass and their relative distance expressed as

$$\mathbf{r}_{\text{cm},kl} = \frac{m_k \mathbf{r}_k + m_l \mathbf{r}_l}{m_k + m_l}, \quad (2.2)$$

and

$$\mathbf{r}_{\text{rel},kl} = \mathbf{r}_k - \mathbf{r}_l, \quad (2.3)$$

where $\mathbf{r}_{\text{cm},kl}$ is the position of the center of mass of particles k and l , and $\mathbf{r}_{\text{rel},kl}$ is the relative distance between particles k and l .

- (c) GORIMO sends back data associated with motion of center of mass, $\mathbf{r}_{\text{cm},kl}$, to the time integrator part. The time integrator part integrates orbit of the center of mass to the next block step as single particle whose mass is $m_k + m_l$, using the approximated equation of motion as

$$\begin{aligned} (m_k + m_l) \frac{d^2 \mathbf{r}_{\text{cm},kl}}{dt^2} &= - \sum_{j \neq k,l}^N \left\{ \frac{G m_j}{|\mathbf{r}_{\text{cm},kl} - \mathbf{r}_j|^2} \left[m_k \frac{\mathbf{b}_{kl,j}}{|\mathbf{b}_{kl,j}|^3} + m_l \frac{\mathbf{b}_{lk,j}}{|\mathbf{b}_{lk,j}|^3} \right] \right\} \\ &\simeq - \sum_{j \neq k,l}^N \left[G(m_k + m_l) m_j \frac{\mathbf{r}_{\text{cm},kl} - \mathbf{r}_j}{|\mathbf{r}_{\text{cm},kl} - \mathbf{r}_j|^3} \right], \end{aligned} \quad (2.4)$$

where

$$\mathbf{b}_{kl,j} = \frac{\mathbf{r}_{\text{cm},kl} - \mathbf{r}_j}{|\mathbf{r}_{\text{cm},kl} - \mathbf{r}_j|} + \frac{m_l}{m_k + m_l} \frac{\mathbf{r}_{\text{rel},kl}}{|\mathbf{r}_{\text{cm},kl} - \mathbf{r}_j|}, \quad (2.5)$$

and

$$\mathbf{b}_{lk,j} = \frac{\mathbf{r}_{\text{cm},kl} - \mathbf{r}_j}{|\mathbf{r}_{\text{cm},kl} - \mathbf{r}_j|} - \frac{m_k}{m_k + m_l} \frac{\mathbf{r}_{\text{rel},kl}}{|\mathbf{r}_{\text{cm},kl} - \mathbf{r}_j|}. \quad (2.6)$$

Here, I use $|\mathbf{r}_{\text{cm},kl} - \mathbf{r}_j| \gg |\mathbf{r}_{\text{rel},kl}|$, and obtain $\mathbf{b}_{kl,j} \simeq (\mathbf{r}_{\text{cm},kl} - \mathbf{r}_j) / |\mathbf{r}_{\text{cm},kl} - \mathbf{r}_j|$, and $\mathbf{b}_{lk,j} \simeq (\mathbf{r}_{\text{cm},kl} - \mathbf{r}_j) / |\mathbf{r}_{\text{cm},kl} - \mathbf{r}_j|$. We call this approximation isolation.

- (d) Using Kepler solution, GORIMO solves, to the next block step, the ap-

proximated equation of motion for relative distance, $\mathbf{r}_{\text{rel},kl}$, expressed as

$$\begin{aligned}
m_{\text{reduce},kl} \frac{d^2 \mathbf{r}_{\text{rel},kl}}{dt^2} &= -\frac{Gm_1 m_2}{|\mathbf{r}_{\text{rel},kl}|^2} \\
&\times \left[\frac{\mathbf{r}_{\text{rel},kl}}{|\mathbf{r}_{\text{rel},kl}|} - \frac{m_j}{m_k + m_l} \sum_{j \neq k,l} \frac{|\mathbf{r}_{\text{rel},kl}|^2}{|\mathbf{r}_{\text{cm},kl} - \mathbf{r}_j|^2} \left(\frac{\mathbf{b}_{kl,j}}{|\mathbf{b}_{kl,j}|^3} - \frac{\mathbf{b}_{lk,j}}{|\mathbf{b}_{lk,j}|^3} \right) \right] \\
&\simeq -Gm_k m_l \frac{\mathbf{r}_{\text{rel},kl}}{|\mathbf{r}_{\text{rel},kl}|^3}, \tag{2.7}
\end{aligned}$$

where $m_{\text{reduce},kl}$ is the reduced mass as $m_{\text{reduce},kl} = m_k m_l / (m_k + m_l)$. Here, I also use $|\mathbf{r}_{\text{cm},kl} - \mathbf{r}_j| \gg |\mathbf{r}_{\text{rel},kl}|$, and obtain $\mathbf{b}_{kl,j} \simeq (\mathbf{r}_{\text{cm},kl} - \mathbf{r}_j) / |\mathbf{r}_{\text{cm},kl} - \mathbf{r}_j|$, and $\mathbf{b}_{lk,j} \simeq (\mathbf{r}_{\text{cm},kl} - \mathbf{r}_j) / |\mathbf{r}_{\text{cm},kl} - \mathbf{r}_j|$.

- (e) GORIMO searches for two particles which are no longer isolated enough from the other particles. If the two particles are found, GORIMO inversely transforms equation (2.2) and (2.3).

In GORIMO, the isolation procedure is also applied to the hierarchical triple system. GORIMO searches for the center of mass of two particles already in isolation and one particle which are isolated enough from the other particles. If such center of mass of two particles already in isolation and one particle are found, GORIMO takes steps (b), (c), and (d). Here, either particle in these steps is replaced by the center of mass of two particles already in isolation. Furthermore, GORIMO searches for hierarchical triple systems which are no longer isolated enough from the other particles. If such hierarchical triple systems are found, GORIMO takes step (e). Here, either particle is also replaced by the center of mass of two particles already in isolation.

I set three kinds of isolation conditions. The three isolation conditions for particle k and l are as follow.

Isolation conditions (A)

1. $E_{\text{bin},kl} > 1kT_0$
2. $|\mathbf{r}_3 - \mathbf{r}_{\text{cm},kl}| > \alpha r_{\text{apo},kl}$
3. $r_{\text{peri},kl} > \alpha \max(s_k, s_l)$

Isolation conditions (B) (only for pairs of two particles)

1. Do not satisfy isolation conditions (A), and $E_{\text{bin},kl} > 0$
2. $e_{kl} > 0.95$
3. $|\mathbf{r}_3 - \mathbf{r}_{\text{cm},kl}| > \beta \mathbf{r}_{\text{rel},kl}$
4. $\mathbf{r}_{\text{rel},kl} \cdot \mathbf{v}_{\text{rel},kl} \leq 0$

Isolation conditions (C) (only for pairs of two particles)

1. $E_{\text{bin},kl} \leq 0$

2. $\Delta t_k \leq \Delta t_{\max}/2^{36}$ and $\Delta t_l \leq \Delta t_{\max}/2^{36}$
3. $|\mathbf{r}_3 - \mathbf{r}_{\text{cm},kl}| > \beta \mathbf{r}_{\text{rel},kl}$
4. $\mathbf{r}_{\text{rel},kl} \cdot \mathbf{v}_{\text{rel},kl} \leq 0$

Here, $E_{\text{bin},kl}$ is the binding energy of particles k and l , expressed as

$$E_{\text{bin},kl} = - \left(\frac{1}{2} \frac{m_k m_l}{m_k + m_l} |\mathbf{v}_{\text{rel},kl}|^2 - \frac{G m_k m_l}{|\mathbf{r}_{\text{rel},kl}|} \right), \quad (2.8)$$

where $\mathbf{v}_{\text{rel},kl} = \mathbf{v}_k - \mathbf{v}_l$. Here, \mathbf{r}_3 is the position of the nearest particle (or center of mass of two particles and hierarchical triple systems in isolation) from the center of mass of particles k and l , $\mathbf{r}_{\text{cm},kl}$. The separations between particles k and l at the apocenter, $r_{\text{apo},kl}$, and pericenter, $r_{\text{peri},kl}$, are, respectively, expressed as

$$r_{\text{apo},kl} = a_{kl}(1 + e_{kl}), \quad (2.9)$$

and

$$r_{\text{peri},kl} = a_{kl}(1 - e_{kl}), \quad (2.10)$$

where a_{kl} is the semi-major axis of particles k and l , expressed as

$$a_{kl} = \frac{G m_k m_l}{2|E_{\text{bin},kl}|}, \quad (2.11)$$

and e_{kl} is the eccentricity of particles k and l , expressed as

$$e_{kl} = \sqrt{1 - \frac{E_{\text{bin},kl} |\mathbf{r}_{\text{rel},kl} \times \mathbf{v}_{\text{rel},kl}|}{G^2 m_k m_l (m_k + m_l)}}. \quad (2.12)$$

Here, $\max(s_k, s_l)$ expresses the larger value between s_k and s_l , and s_i ($i = k, l$) is the size of particle (or center of mass of two particles and hierarchical triple system) i . Particle i has $s_i = 0$, and the center of mass of two particles in isolation has s_i equal to the separation at the apocenter between the two particles. Through dimensionless quantities α (called apocentric parameter) and β (called pericentric parameter), I decide the strictness of isolation. I discuss appropriate apocentric and pericentric parameters in section 2.5.2.

In figure 2.2, I illustrate binaries in isolation with conditions (A) (upper panel), and with conditions (B) (lower left panel), and unbound two particles in isolation with condition (C). A binary with components k and l are in isolation with conditions (A), if the other particles are not in the sphere centered on the center of mass of the binary with radius $\alpha r_{\text{apo},kl}$, where α is a dimensionless quantity, and $r_{\text{apo},kl}$ is the separation of the binary components k and l at the apocenter. The binary are in isolation with conditions (B), if the other particles are in the sphere centered on the center of mass of the binary with radius $\alpha r_{\text{apo},kl}$, but are not in the sphere centered on the center of mass of the binary with radius $\beta r_{\text{rel},kl}$, where β is a dimensionless quantity, and $r_{\text{rel},kl}$ is the separation of the binary components k and l . Unbound two particles are also in

isolation with conditions (C), if the other particles are not in the sphere centered on the center of mass of the binary with radius $\beta r_{\text{rel},kl}$, and the timestep of both the particles is sufficiently small as second condition in conditions (C).

The algorithm of GORILLA is described step-by-step in Appendix A.

2.3 How to use GORIMO

I describe application programming interface (API) of GORIMO in this section. GORIMO is currently written in C language. I describe a part of an example code to show how to use GORIMO from the time integrator part as follows.

```

/* initial settings */
(input initial conditions)
gorilla_init(filename, time, dtout, eta, eta_s,
             dtmax, dtmin, eps2, n, ncom, index);
while(t<tend){
  (select minimum dti and set global time)
  (integrate particles with minimum ti + dti)
  /* GORIMO */
  gorilla_main(time, &n, t, dt, m, r0, v0, a0, j0, pot, nmb, ncom,
              grapeflag, delflag, index);
}

```

Initial settings are done outside the while loop, and the while loop includes the time integrator part and GORIMO.

The API of GORIMO is the following two functions:

- `gorilla_init`: sends some parameters, such as output parameters and accuracy parameters, to GORIMO, and receive initial status of isolation.
- `gorilla_main`: sends data of all the particles to GORIMO, and receives the information on the special treatment from GORIMO.

The definition of the function `gorilla_init` is as follows.

```

void gorilla_init(FILE *filename,
                  double time, /* global time */
                  double dtout,
                  double eta, /* accuracy parameter */
                  double eta_s, /* accuracy parameter for start up */
                  double dtmax, /* maximum timestep */
                  double dtmin, /* minimum timestep */
                  double eps2, /* square of softening parameter */
                  int n, /* the number of particles */
                  int ncom[],
                  int index[])

```

Through the function `gorilla_init`, the time integrator part initially sends some parameters to GORIMO. The argument `filename` points to file into which the information on the special treatment is written. The information is divided into two groups. One group is log of isolation: particle indexes for which isolation starts and the time when the isolation starts, and particle indexes for which isolation is finished and the time when the isolation is finished. The other group is the internal information of all the binaries and hierarchical triple systems in isolation, which is output at each `dtout`, the third argument. The arguments `eta` and `eta_s` are accuracy parameters. The arguments `dtmax` and `dtmin` are the maximum and minimum of the timestep of the particles. The argument `eps2` is square of softening parameter. The argument `n` is the number of the particles in the cluster. The argument `index` is the index of the particles assigned by the time integrator at the initial time.

Exceptionally, the time integrator part receives the particle data from GORIMO through the argument `ncom`. The argument `ncom` indicates whether it belongs to particles, or the center of mass of two particles or hierarchical triple systems in isolation. If the argument `ncom` is one, it is a particle, if the argument `ncom` is two, it is the center of mass of two particles in isolation, and if the argument `ncom` is three, it is the center of mass of hierarchical triple systems.

The definition of the function `gorilla_main` is as follows:

```

void gorilla_main(double time,    /* global time */
                  int *n,        /* the number of particles */
                  double t[],    /* particle's time */
                  double dt[],   /* particle's timestep */
                  double m[],    /* mass */
                  double r0[][3], /* position */
                  double v0[][3], /* velocity */
                  double a0[][3], /* acceleration */
                  double j0[][3], /* time derivative of acceleration */
                  double pot[],
                  int nnb[],
                  int ncom[],
                  int grapeflag[],
                  int delflag[],
                  int index[])

```

Through the function `gorilla_main`, the time integrator part sends the global time, `time`, and the data of all the particles to GORIMO. The particle data sent by the time integrator part are their times, `t`, timesteps, `dt`, masses, `m`, positions, `r0`, velocities, `v0`, accelerations, `a0`, time derivatives of the acceleration, `j0`, potential, `pot`, and the indexes of the nearest particles, `nnb`.

The time integrator part also sends `delflag` to GORIMO. The argument `delflag` is a flag whether the particle is deleted by GORIMO or not. If the argument `delflag` of a particle is one, the particle is deleted by GORIMO, otherwise it is not deleted. The deleting of the particles is used for particles which are sufficiently far from the cluster, and seem not to affect the evolution of the cluster any more.

Through the function `gorilla_main`, the time integrator part receives the total number of the particles and the center of mass in the integration list, `n`, which decreases by one when one binary is formed, and the data of all the particles from GORIMO. The particle data received by the time integrator part are their times, `t`, timesteps, `dt`, masses, `m`, positions, `r0`, velocities, `v0`, accelerations, `a0`, time derivatives of the acceleration, `j0`, potential, `pot`, the indexes of the nearest particles, `nnb`, and `ncom`.

Furthermore, the time integrator part receives `grapeflag` and `index` from GORIMO. The argument `grapeflag` shows whether particles pointed by the indexes are changed or not before and after GORIMO is called. If the particles are changed, `grapeflag` is one, and if not, `grapeflag` is zero. The argument `index` shows the initial indexes of the particles pointed by the indexes. The argument `grapeflag` is used for the judgment whether particle data is sent to GRAPE or not. If the indexes of the particles are changed, the particle data should be sent, otherwise should not be sent.

2.4 Test simulation

I perform test simulation of GORILLA. I simulate ten $N = 1024$ equal-mass cluster without primordial binaries. I use Plummer's model to generate the initial distribution of these clusters, and use different random seeds. I adopt N -body standard units (Heggie, Mathieu 1986), such that $G = M = -E = 1$, where M is the total mass of the cluster, E is the energy that the total binding energy of binaries and high-order hierarchical systems is excluded from the total energy of the cluster. I adopt the accuracy parameter $\eta = 0.01$ and $\eta_s = 0.0025$, and the apocentric and pericentric parameters, $(\alpha, \beta) = (10, 100)$. In the $N = 1024$ clusters, $1kT_0 = 1.6 \times 10^{-4}$. For force calculation, I use GRPAE-6A, a special-purpose computer designed to accelerate N -body simulations (Fukushige et al. 2005).

Figure 2.3 shows the time evolution of the total energies of the ten clusters in N -body simulation by means of GORILLA, in which the time when core collapse stops is about 300. The dashed horizontal lines show the energy error 1 %, i.e. -0.2475 , and -0.2525 . In nine runs, the energy errors are about 1 %. However, in one run, the energy error exceeds well over 1 %. This is due to one hierarchical triple system, described in detail in the next section.

2.5 Reliability

As seen in the previous subsection, the energy errors are relatively large: ~ 1 % in nine of the ten simulations, and ~ 10 % in one of the ten simulations. In section 2.5.1, I find that most energy error arises from long-lived hierarchical triple systems in which inner binaries are intermittently in isolation due to the orbits of the third stars. The energy error is generated from the integration of the orbits of the inner binaries when they are not in isolation, and from the approximation of the orbits of the inner binaries in isolation. In section 2.5.2, I find the optimal criteria of isolation such that both energy errors are suppressed as low as possible. Even if we adopt the optimal criteria, the energy errors become relatively large. In section 2.5.3, I discuss the effect of the energy error from the hierarchical triple systems on structural parameters of the clusters.

2.5.1 Generation process of large energy error

Energy error from isolation

Before I show the generation process of large energy error, I describe what generates energy error. There are two causes of energy error. One is the time integration of orbits of particles. The other is isolation of binaries or hierarchical triple systems.

To show the above argument, I perform orbital integrations of a hierarchical triple system, and a binary. In the hierarchical triple system, particles have equal mass, $1/16384$. At the initial time, the inner binary has the binding energy $100kT_0$ and the eccentricity 0.1, and the outer binary has the binding

energy $5kT_0$ and the eccentricity 0.9, where $1kT_0 = 1.0 \times 10^{-5}$ in N -body standard units. The orbit of the outer binary is retrograde with respect to the inner binary. The orbits are drawn in figure 2.6. The binary of which I perform the orbital integration is identical to the inner binary of the hierarchical triple system. I adopt accuracy parameters $\eta = 0.01$ and $\eta_s = 0.0025$. The apocentric parameter is set to be $\alpha = 10$, and $\alpha = \infty$ for the orbital calculation of the hierarchical triple system and the binary, respectively.

Figure 2.4 shows the time evolution of the total energy error (black solid line), the energy error due to isolation (red solid line), and the other energy error (blue solid line) in the simulation of the hierarchical triple system. The error due to isolation is the accumulation of the energy error before and after isolation starts, or isolation is finished. Figure 2.5 shows the time evolution of the other energy error in the simulation of the hierarchical triple system (blue solid line), and the total error multiplied by 0.04 in the simulation of the binary (black solid line).

From figure 2.5, we see that the other energy error in the simulation of the hierarchical triple system (blue solid line) is in good agreement with the total error multiplied by 0.04 in the simulation of the binary (black solid line). The total error in the simulation of the binary is only due to the orbital integration, and the time when the orbit of the inner binary in the hierarchical triple system is integrated is 4 % of that when the orbit of the binary is integrated owing to the isolation of the inner binary. The other energy error in the simulation of the hierarchical triple system is only due to the orbital integration of the inner binary.

Next, I explain only how the isolation generates energy errors, since the former is trivial. In order to show how the isolation generates energy errors, I follow the evolution of the above hierarchical triple system with and without GORILLA. I adopt accuracy parameters $\eta = 0.0025$ and $\eta_s = 0.00125$. The accuracy parameters are smaller than those in the previous N -body simulation. This is because I make the energy errors from the integration sufficiently small, and the energy errors from the isolation become pronounced. Since the inner binary satisfies isolation conditions (A), I change the apocentric parameter $\alpha = 10$, and $\alpha = \infty$ i.e. without GORILLA. We assume that the orbits of the hierarchical triple system are correctly followed by the simulation without GORILLA.

Figure 2.7 shows the total energy of the hierarchical triple system in the N -body simulation with isolation (blue), and without isolation (red). The simulation is finished at the time when the phase of the outer binary returns to the pericenter. The arrows show the time when isolation starts and is finished. The total energy decreases by 1×10^{-6} after the isolation.

When the inner binary is in isolation, the total energy oscillates in the following reason. The total energy of the hierarchical triple system, $E_{3\text{body}}$, consists of the binding energies of the inner binary, E_{bin} , and the outer binary, E_{bout} , and the other energy, E_{other} , as follows:

$$E_{3\text{body}} = E_{\text{bin}} + E_{\text{bout}} + E_{\text{other}}, \quad (2.13)$$

where the velocity of the center of mass of the hierarchical triple system is zero. Suppose that the inner binary components are particle 1, and 2, and the third star is particle 3, the above three energies are expressed as

$$E_{\text{bin}} = \frac{1}{2} \frac{m_1 m_2}{m_1 + m_2} |\mathbf{v}_{\text{rel},12}|^2 - \frac{G m_1 m_2}{|\mathbf{r}_{\text{rel},12}|}, \quad (2.14)$$

and

$$E_{\text{bout}} = \frac{1}{2} \frac{(m_1 + m_2) m_3}{m_1 + m_2 + m_3} |\mathbf{v}_{\text{cm},12} - \mathbf{v}_3|^2 - \frac{G(m_1 + m_2) m_3}{|\mathbf{r}_{\text{cm},12} - \mathbf{r}_3|}, \quad (2.15)$$

and

$$\begin{aligned} E_{\text{other}} &= -\frac{G m_1 m_3}{|\mathbf{r}_{\text{rel},13}|} - \frac{G m_2 m_3}{|\mathbf{r}_{\text{rel},23}|} + \frac{G(m_1 + m_2) m_3}{|\mathbf{r}_{\text{cm},12} - \mathbf{r}_3|} \\ &\simeq -\frac{G}{|\mathbf{r}_{\text{cm},12} - \mathbf{r}_3|} \frac{m_1 m_2 m_3}{m_1 + m_2} \left\{ \frac{3}{2} \frac{[(\mathbf{r}_{\text{cm},12} - \mathbf{r}_3) \cdot \mathbf{r}_{\text{rel},12}]^2}{|\mathbf{r}_{\text{cm},12} - \mathbf{r}_3|^4} - \frac{1}{2} \frac{|\mathbf{r}_{\text{rel},12}|^2}{|\mathbf{r}_{\text{cm},12} - \mathbf{r}_3|^2} \right\} \\ &\simeq -\frac{G |\mathbf{r}_{\text{rel},12}|^2}{|\mathbf{r}_{\text{cm},12} - \mathbf{r}_3|^3} \frac{m_1 m_2 m_3}{m_1 + m_2} \left(\frac{3 \cos^2 \varphi - 1}{2} \right), \end{aligned} \quad (2.16)$$

where the second equality in equation (2.16) is derived, assuming $|\mathbf{r}_{\text{rel},12}|/|\mathbf{r}_{\text{cm},12} - \mathbf{r}_3| \ll 1$, and ignoring higher terms than $|\mathbf{r}_{\text{rel},12}|^2/|\mathbf{r}_{\text{cm},12} - \mathbf{r}_3|^2$, and the third equality in equation (2.16) is derived, using the angle φ is between the vectors $\mathbf{r}_{\text{rel},12}$, and $\mathbf{r}_{\text{cm},12} - \mathbf{r}_3$. When the inner binary is in isolation, its binding energy, E_{bin} , is not changed. The binding energy of the outer binary, E_{bout} , is also not changed, since the relative motion between the center of mass of the inner binary and the third particle is two-body motion. The other energy, E_{other} , oscillates with the rotation of the inner binary. The angle φ runs from $-\pi$ radian through π radian during a period of the inner binary, since that the vector $\mathbf{r}_{\text{cm},12} - \mathbf{r}_3$ is hardly changed on the timescale.

Figure 2.8 shows the time evolution of the binding energies of the inner binary, E_{bin} (top panel), and the outer binary, E_{bout} (middle panel), and the other energy, E_{other} (bottom panel). The colors of the curves are the same as in figure 2.7. The vertical dashed lines show the times when isolation starts and is finished.

The energy error due to isolation arises from the following reason. Unless isolation is used for the inner binary, the binding energy of the inner binary, E_{bin} , oscillates (red lines in top panel of figure 2.8). The oscillations are reactions of the oscillations of the other energy, E_{other} , as shown in equation (2.16). However, if isolation is used, this binding energy, E_{bin} , is not changed when the inner binary is in isolation (blue lines in top and middle panels of figure 2.8). This is because the tidal force of the third particle is ignored. This binding energy at the time when the isolation is finished is different from that at the same time unless isolation is used for the inner binary.

With and without GORILLA, I additionally follow the evolution of the other hierarchical system in which the binary satisfies isolation conditions (B), and

investigate how the isolation generates energy errors. In the hierarchical triple system, all particles have $1/16384$. At the initial time, the inner binary has the binding energy $100kT_0$ and the eccentricity 0.99, and the outer binary has the binding energy $20kT_0$ and the eccentricity 0. The orbits are drawn in figure 2.9. I adopt accuracy parameters $\eta = 0.0025$ and $\eta_s = 0.00125$ for the same reason as in the above simulation. I change the pericentric parameter $\beta = 10$, and $\beta = \infty$ i.e. without GORILLA.

Figure 2.10 shows the time evolution of the total energy of the hierarchical triple system, $E_{3\text{body}}$ (upper left panel), the binding energies of the inner binary, E_{bin} (upper right panel), and the outer binary, E_{bout} (lower left panel), and the other energy, E_{other} (lower right panel). The blue dashed curves and red solid curves show these energies in the N -body simulation with and without isolation, respectively. The vertical dotted lines show the time when isolation starts (left), and the time when isolation is finished (right) in the N -body simulation with isolation.

Similarly to the case of the binary in isolation conditions (A), the energy error due to isolation arises from the difference of the time evolutions of the binding energies of the inner binaries between the cases with and without GORILLA. Despite of the change of the binding energy of the inner binary in the simulation without GORILLA, the binding energy of the inner binary is not changed in the simulation with GORILLA (the upper right panel of 2.10). In the simulation with GORILLA, the increase of the total energy of the hierarchical triple system before and after the isolation is equal to that of the binding energy of the inner binary before and after the isolation (the upper left and right panels of 2.10).

Hierarchical triple systems as large energy error sources

Even if a single particle approaches to a binary once, the energy error both from the integration and isolation of the binary is sufficiently smaller than the total energy of the cluster. However, when the penetrations to the binary are repeated, the situation is changed. The repeat of the penetrations occurs in hierarchical triple systems.

In fact, the 10 % energy error in one of the ten simulations is due to one hierarchical triple system. In order to prove clearly that most energy error is generated from the hierarchical triple system, I show figure 2.11 which draws the time evolution of the total energy of the system (upper left panel), its enlargement at the impulsive increase of the energy error, E_{total} (upper right panel), the total energy, $E_{3\text{body}}$, of a hierarchical triple system present at the time $t \sim 800$ (lower left panel), and the difference between the total energy of the system, and the hierarchical triple system (lower right panel). The difference between E_{total} and $E_{3\text{body}}$ are little changed (lower right panel).

2.5.2 Optimal criteria of isolation

As seen in previous section, most energy errors are generated from long-lived hierarchical triple systems in which inner binaries are intermittently in isolation due to the orbits of the third stars. To suppress the energy errors in the simulations of the clusters is to minimize the energy errors from hierarchical triple systems. In this section, I search for the optimal criteria of isolation which minimize the energy errors from hierarchical triple systems.

For this purpose, I perform orbital integration of typical hierarchical triple systems by means of GORILLA, changing the apocentric and pericentric parameters, α and β , respectively, and find the optimal criteria. After that, I prove the parameters to be optimal criteria, performing N -body simulations of clusters with primordial binaries.

The typical hierarchical triple systems are as follows. The outer binaries have to be robust against the perturbation of the other stars. Therefore, the binding energies of the outer binaries are more than $1kT_0$. The inner binaries have to be harder than the outer binaries by factor of at least ten. The hierarchical triple systems are long-lived only when the inner binaries are rather isolated from the third stars.

I use the two hierarchical triple systems in section 2.5.1 whose orbits are drawn in figure 2.6 and 2.9. They are treatable, since they satisfy either isolation conditions (A) or (B). First, I investigate the former hierarchical triple system for the apocentric parameter, α , and subsequently the latter hierarchical triple system for the pericentric parameter, β .

I perform orbital integration of the hierarchical triple system whose orbits are drawn in figure 2.6 with different apocentric parameter $\alpha = 5, 10, 20$, and 40, and without isolation. I adopt the accuracy parameters $\eta = 0.01$ and $\eta_s = 0.0025$, in which the simulations in section 3 can be finished within acceptable computing time.

Figure 2.12 shows the time evolution of energy errors. As the apocentric parameter α becomes larger, the evolutions of the energy errors become smoother. This is because the energy errors from the integration are generated smoothly, and become dominant as the apocentric parameter α becomes larger. In the apocentric parameter $\alpha = 10$, the energy error is smallest. Figure 2.13 shows the total energy errors, that from isolation, and that from integration at the time when the simulations are finished as a function of the apocentric condition α . The energy errors from isolation, and from integration are balanced at $\alpha = 10$.

Figures 2.12 and 2.13 mean that I should adopt the apocentric parameter $\alpha \leq 10$. If the hierarchical triple system lasts for more than 0.125 time units, the energy error in the apocentric parameter $\alpha = 10$ will be larger than that in the apocentric parameter $\alpha = 5$. This is because the former energy error is more strongly occupied by energy error from the integration, which is systematically accumulated, and less strongly by energy error from the isolation, which is diffusive spread.

I perform orbital integration of the hierarchical triple system whose orbits are drawn in figure 2.9 with the pericentric parameter $\beta = 5, 6, 7, \dots, 999, 1000$

during 1 period of the inner binary. I also adopt the accuracy parameter $\eta = 0.01$, and $\eta_s = 0.0025$. Figure 2.14 shows the total energy error (black), the energy error from integration (blue), and the energy error from isolation (red) as a function of the pericentric parameter β . The total energy error is minimized around $\beta = 100$, in which the energy errors from integration and from isolation are balanced. It is valid that I adopt the pericentric parameter $\beta = 100$.

I perform N -body simulations of clusters to conform whether the above apocentric and pericentric parameters minimizing energy errors is applicable not only to hierarchical triple systems, but also N -body systems. I adopt N -body standard units. The clusters have equal-mass and point-mass particles whose number is 1024, not 16384 unlike in section 3. This is because I perform many runs. The mass fraction of primordial binaries is 10 %, and the binding energies of all the binaries are $300kT_0$ ($1kT_0 = 1.6 \times 10^{-4}$), which is expected to generate the largest energy error among simulations in section 3. The eccentricity distribution of the primordial binaries is thermal distribution, $f(e) = 2e$. The other orbital elements of the primordial binaries, such as the inclination, the longitude of the ascending node, and the argument of pericenter with respect to the clusters and the phase are distributed at random. I use Plummer's model to generate the initial distribution of both single stars and center of mass of primordial binaries in the clusters.

I parameterize the apocentric parameter α , and the pericentric parameter β , and set $(\alpha, \beta) = (5, 100), (10, 100), (20, 100), (10, 10), (10, 1000)$. I adopt the accuracy parameter $\eta = 0.01$ and $\eta_s = 0.0025$. At each pair of the apocentric and pericentric parameters, I perform five runs.

Figure 2.15 shows the time evolution of the energy error, ΔE , of one run at each set of the apocentric and pericentric parameters. The impulsive increases of the energy errors are due to the appearance of hierarchical triple systems. Figure 2.16 shows the time when the energy errors are beyond 1 % in the N -body simulations of the above clusters. Here, the criterion of the energy error is the energy that the total binding energy of binaries and high-order hierarchical systems is excluded from the total energy of the cluster, i.e. $E = -0.25$. Therefore, 1 % of the total energy is 0.0025. In the left panel, the apocentric parameter α is changed, keeping the pericentric parameter β constant, and in the right panel, vice versa. As seen in this figure, the times when the energy errors exceed 1 % are relatively large in the apocentric parameter $\alpha = 10$, and the pericentric parameter $\beta = 100$. This is in good agreement with the case of the above hierarchical triple systems.

2.5.3 Influence of energy error on structural parameters

By means of GORILLA, the accuracy of energy error is at best ~ 1 %. In this section, I describe no dependence of quantities we use in section 3 on energy errors. The quantities are structural parameters of clusters.

I perform N -body simulations of clusters in which $N = 4096$, particles are equal-mass and point-mass, mass fraction of primordial binaries is 10 %, and the binding energy of all the binaries is $300kT_0$. The settings of the other parameters

of the binaries are the same as in the above clusters in which $N = 1024$, mass fraction of primordial binaries is 10 %, and the binding energy of all the binaries is $300kT_0$. I adopt the N -body standard units, the accuracy parameter $\eta = 0.01$ and $\eta_s = 0.0025$, and the apocentric and pericentric parameters, $(\alpha, \beta) = (2, 100), (5, 100), (10, 100)$, and $(10, 10)$. In this units, $1kT_0 = 4.1 \times 10^{-5}$. At each set of the apocentric and pericentric parameters, I perform three runs with different random seeds. I use the clusters with $N = 4096$, since several runs are possible in acceptable computing time, and fluctuations of structural parameters on dynamical timescale are suppressed. Figure 2.17 shows the time evolution of energy errors. The upper left, upper right, lower left, and lower right panels are, respectively, the apocentric and pericentric parameters $(\alpha, \beta) = (2, 100), (5, 100), (10, 100)$, and $(10, 10)$.

I describe about Lagrange radii as an example of structural parameters. Figure 2.18 shows the time evolution of 1, 10, 50, and 80 % Lagrange radii from bottom up. The colors of the curves correspond to those of the curves in figure 2.17. The Lagrange radii of the clusters in the apocentric and pericentric parameters $(\alpha, \beta) = (2, 100)$, and $(10, 10)$ (red and magenta curves, respectively) are not different from those of the clusters in the apocentric and pericentric parameters $(\alpha, \beta) = (5, 100)$, and $(10, 100)$ (blue and aqua curves, respectively) in the respect of the time-averaged size over several ten time units. In the former runs, the energy errors are ~ 10 %, and in the latter runs, less than 1 %.

The time averaged Lagrange radii over several ten time units are independent of the energy errors, even if it is the most inner radius, i.e. 1 % Lagrange radius. The energy error does not affect the structural parameters of clusters very much. This is because a large fraction of the energy errors goes to the binding energy of the inner binaries in the hierarchical triples generating large energy errors as is seen in top panel of figure 2.8, and upper right panel of 2.10).

2.6 Comparison with other codes

I compare simulation results by means of GORILLA with those by means of NBODY4, and kira. For GORILLA, I use the simulation results in section 2.4. For NBODY4 and kira, I use the simulation results of Anders et al. (2007), who have performed ten $N = 1024$ clusters without primordial binaries by means of NBODY4, and thirty $N = 1024$ clusters without primordial binaries by means of kira. Their results are shown in figure 2.20.

In figure 2.19, I show the core radii, r_c , and half-mass radii, r_h , of ten $N = 1024$ clusters in gray dots. I obtain the core radii in the way of Casertano and Hut (1985). Solid lines show the average values over these clusters at each time. Figure 2.20 shows the simulation results of Angers et al. (2007). The times when core collapses stop are ~ 300 in the three codes. The average core radii, half-mass radii, and kinetic energies are, respectively, ~ 0.1 , ~ 3 , and ~ 0.2 at the time when the simulations are finished in the three codes. My results by means of GORILLA agree with those by means of kira and NBODY4.

GORILLA

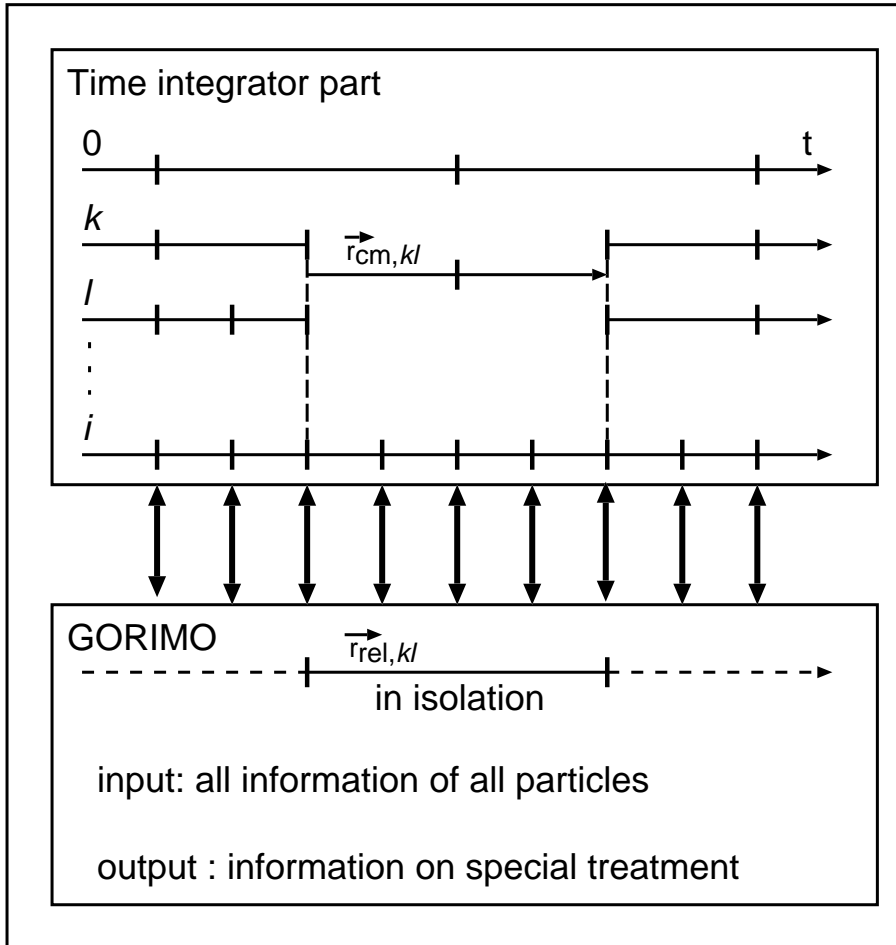


Figure 2.1: Illustration of the structure of GORILLA.

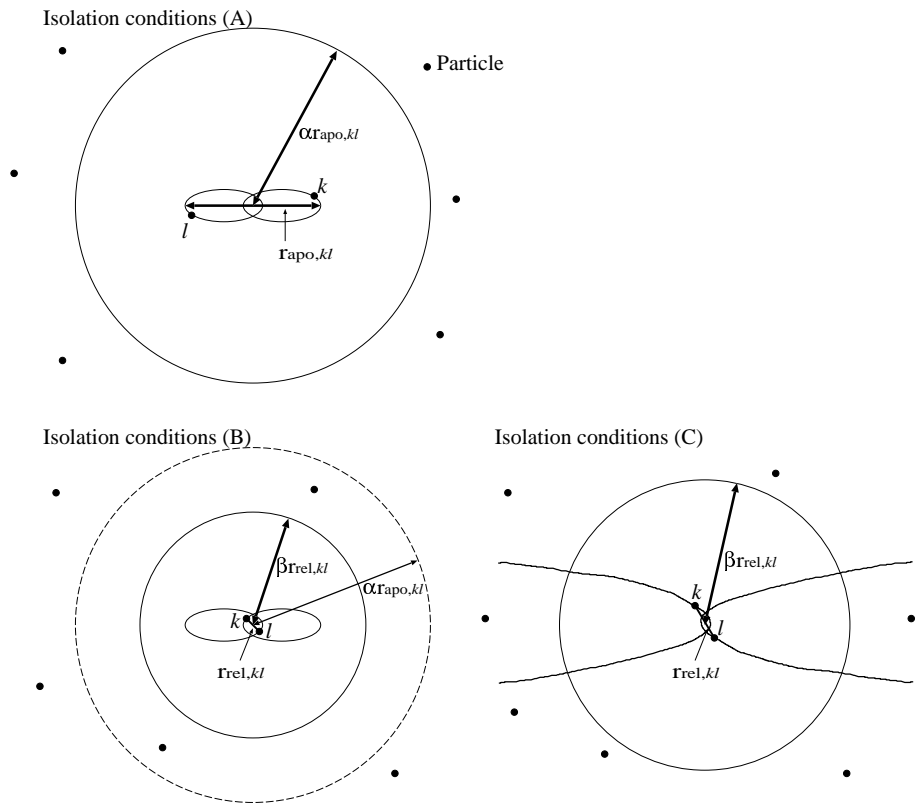


Figure 2.2: Illustration of binaries in isolation with conditions (A) (upper panel), and conditions (B) (lower left panel), and unbound two particles in isolation with conditions (C) (lower right panel).

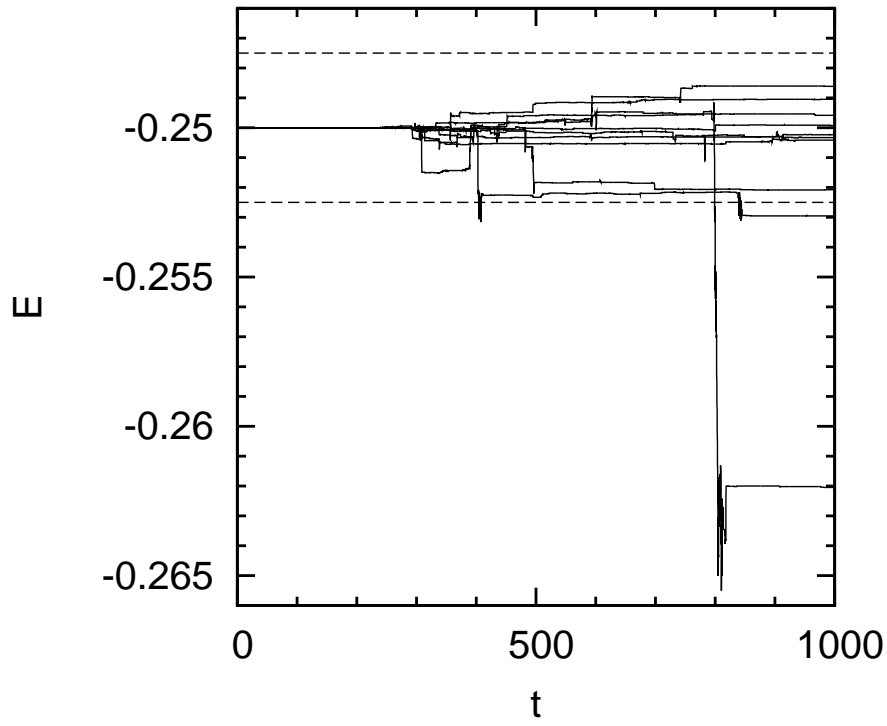


Figure 2.3: Time evolution of the total energies of ten clusters with $N = 1024$ and without primordial binaries.

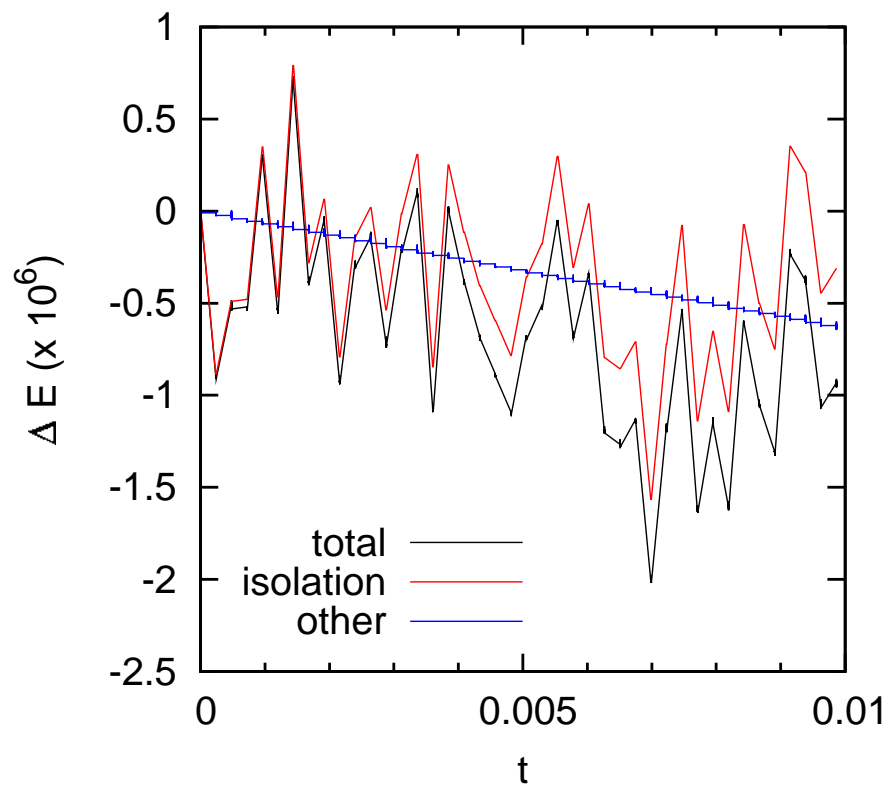


Figure 2.4: Time evolution of the total energy error (black solid line), the energy error due to isolation (red solid line), and the other energy error (blue solid line).

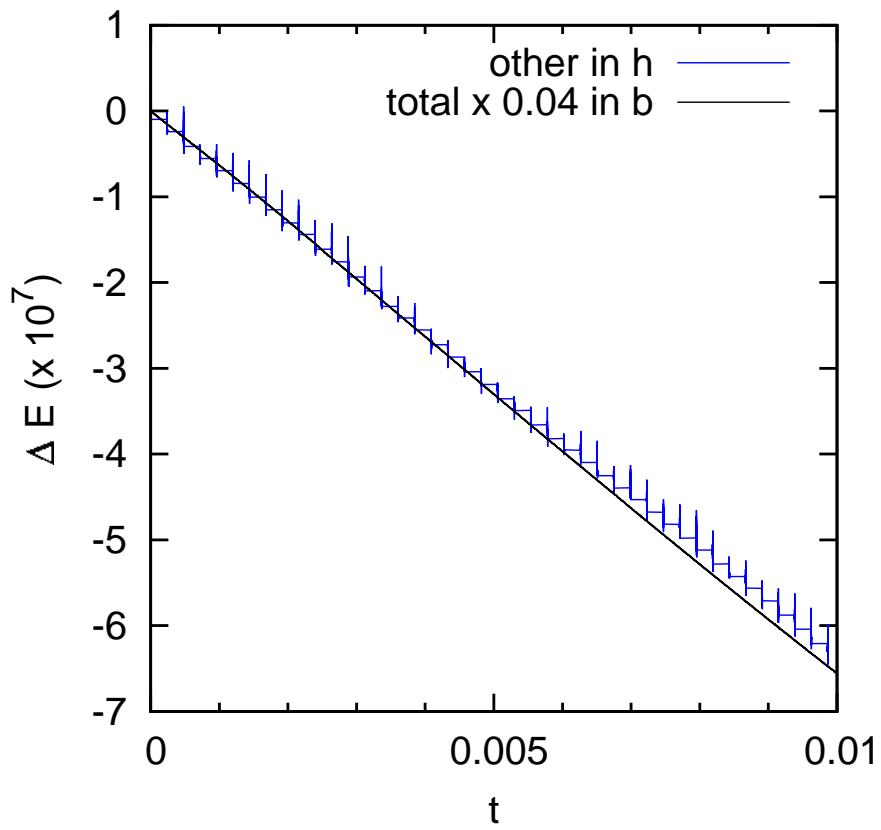


Figure 2.5: The time evolution of the other energy error in the simulation of the hierarchical triple system (blue solid line), and the total error multiplied by 0.04 in the simulation of the binary (black solid line).

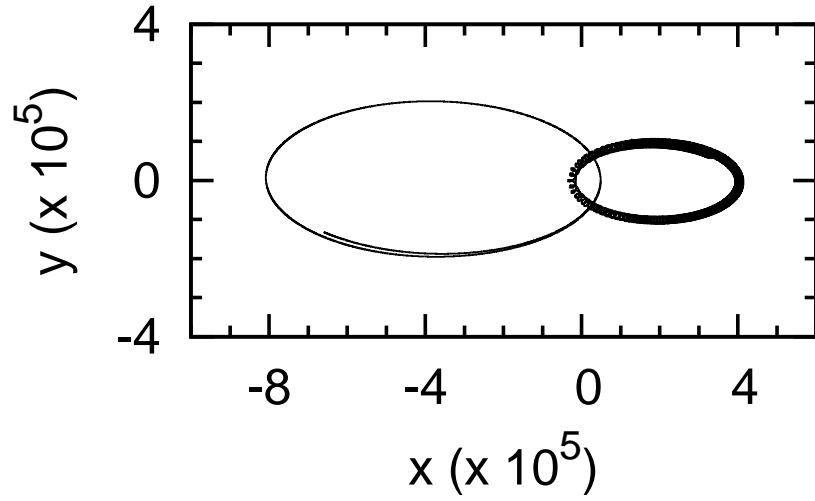


Figure 2.6: The internal motions of the isolated hierarchical triple system which is in isolation in a part of the phase of the outer binary when the apocentric condition $\alpha = 5 \sim 60$.

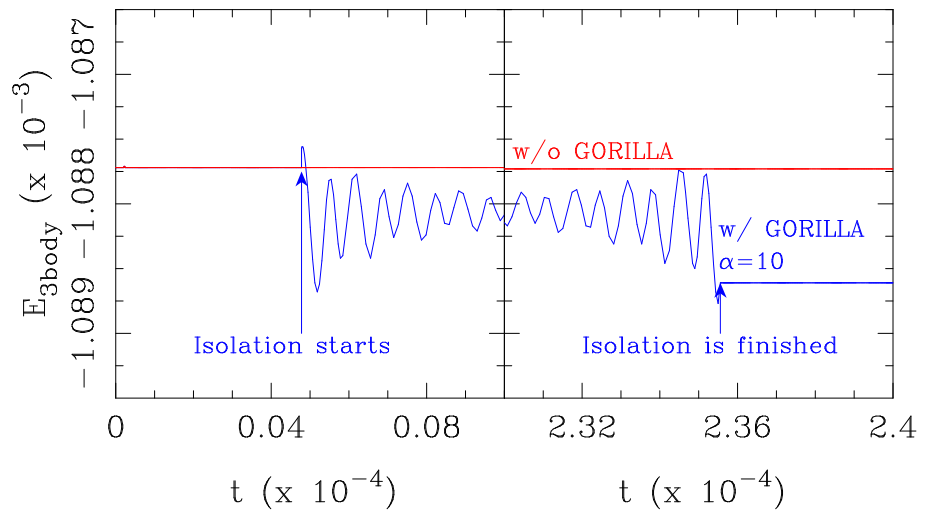


Figure 2.7: The time evolution of the total energy of the hierarchical triple system in figure 2.6 with GORILLA of the apocentric condition $\alpha = 5$ (blue) and without GORILLA (red).

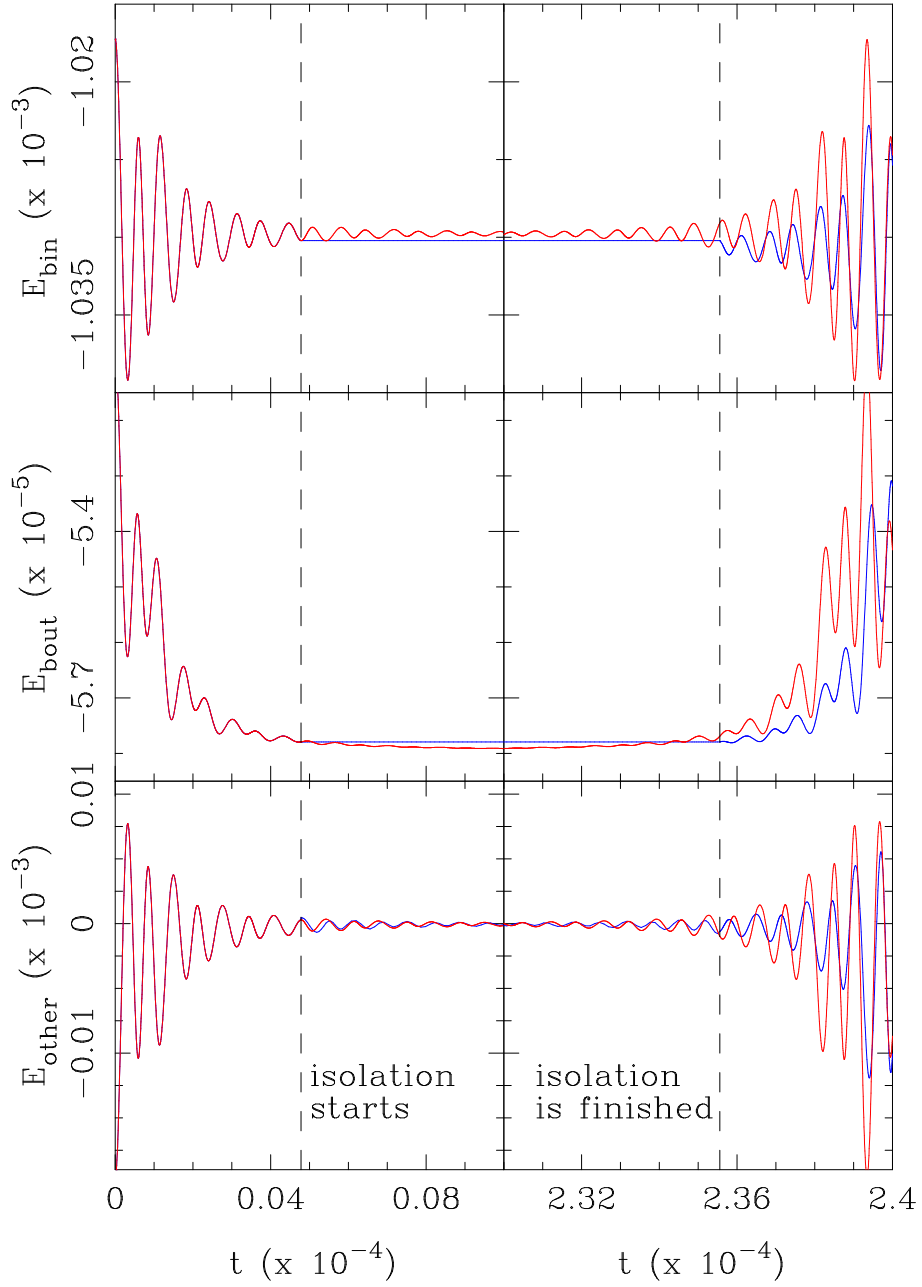


Figure 2.8: The time evolution of the binding energies of the inner binary (upper panel) and the outer binary (middle panel), and the other energy (lower panel), whose definitions are in main text. The blue and red curves are, respectively, calculated with and without GORILLA.

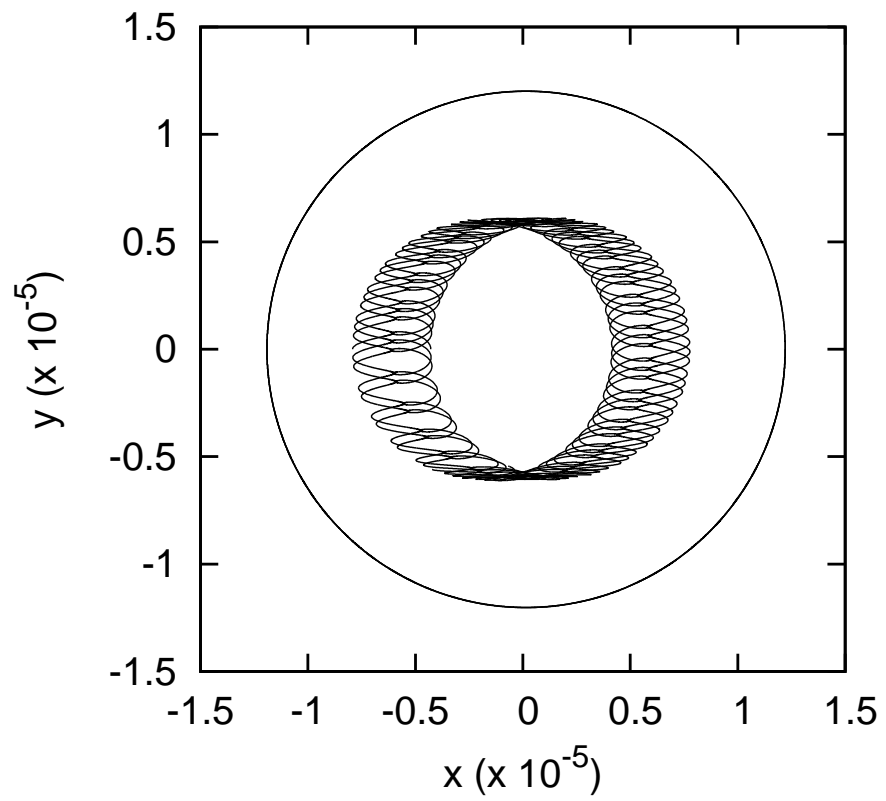


Figure 2.9: The internal motions of the isolated hierarchical triple system which is in isolation around at the pericenter of the inner binary when the pericentric condition $\beta \leq 1000$.

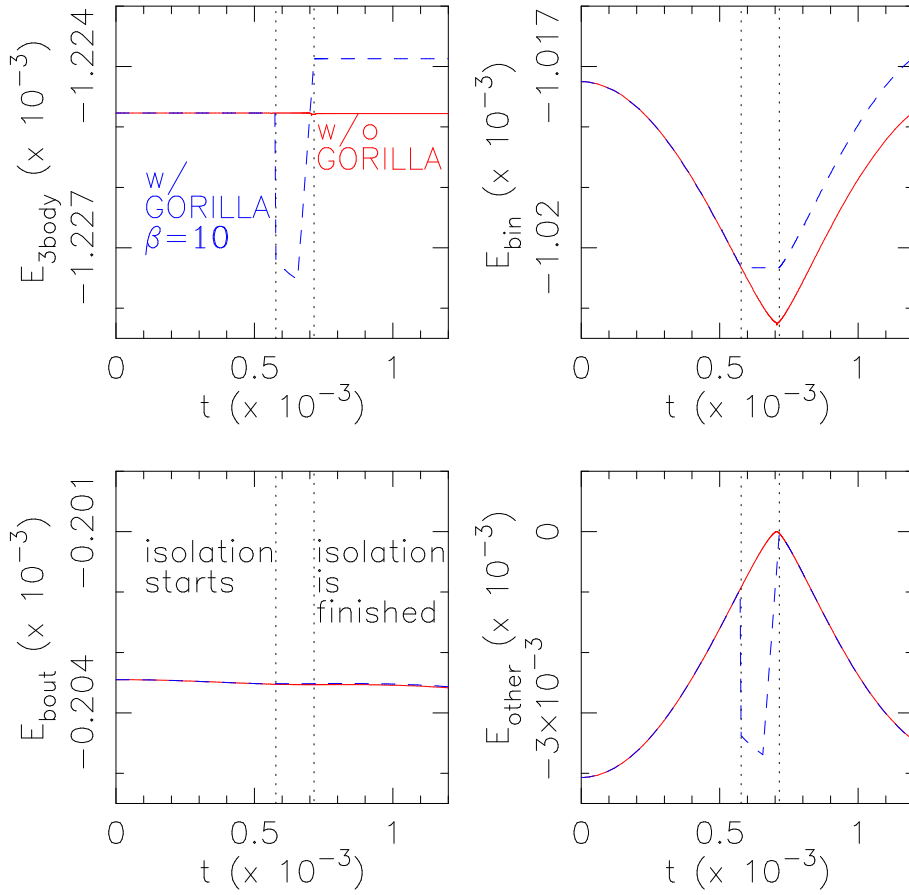


Figure 2.10: The time evolution of the total energy (upper left), the binding energies of the inner binary (upper right) and outer binary (lower left), and the other energy (lower right) in the hierarchical triple system in figure 2.9. The blue dashed curves and red solid curves show these energies in the simulations with isolation and without isolation, respectively. The vertical dotted lines show the time when isolation starts, and when isolation is finished.

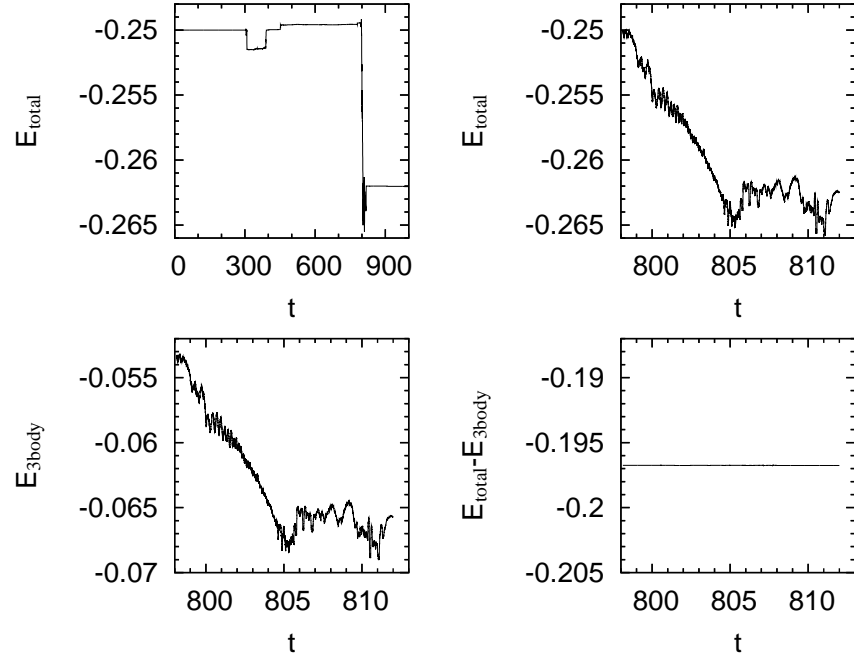


Figure 2.11: Time evolution of the total energy of the system (upper left), its enlargement at the impulsive increase of the energy error, E_{total} (upper right panel), the total energy, $E_{3\text{body}}$, of a hierarchical triple system present at the time $t \sim 800$ (lower left panel), and the difference between the total energy of the system, and the hierarchical triple system (lower right panel).

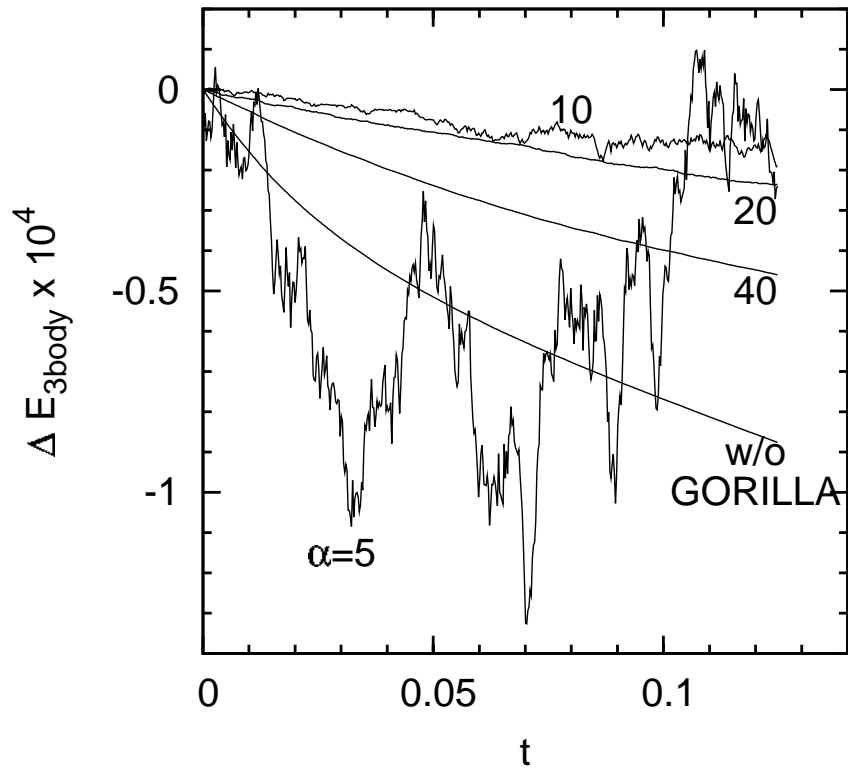


Figure 2.12: The time evolution of the hierarchical triple system in figure 2.6 with GORILLA of the apocentric conditions $\alpha = 5, 10, 20$, and 40 , and without GORILLA.

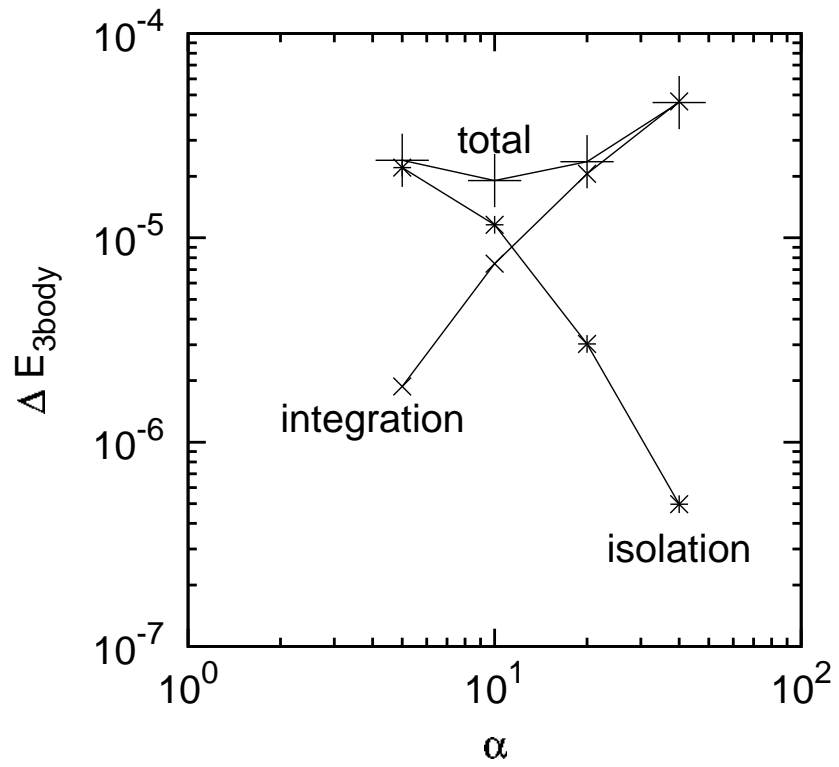


Figure 2.13: The total energy error, and energy errors from integration and from isolation at the time when simulations are finished in figure 2.12, with GORILLA of the apocentric conditions $\alpha = 5, 10, 20$, and 40.

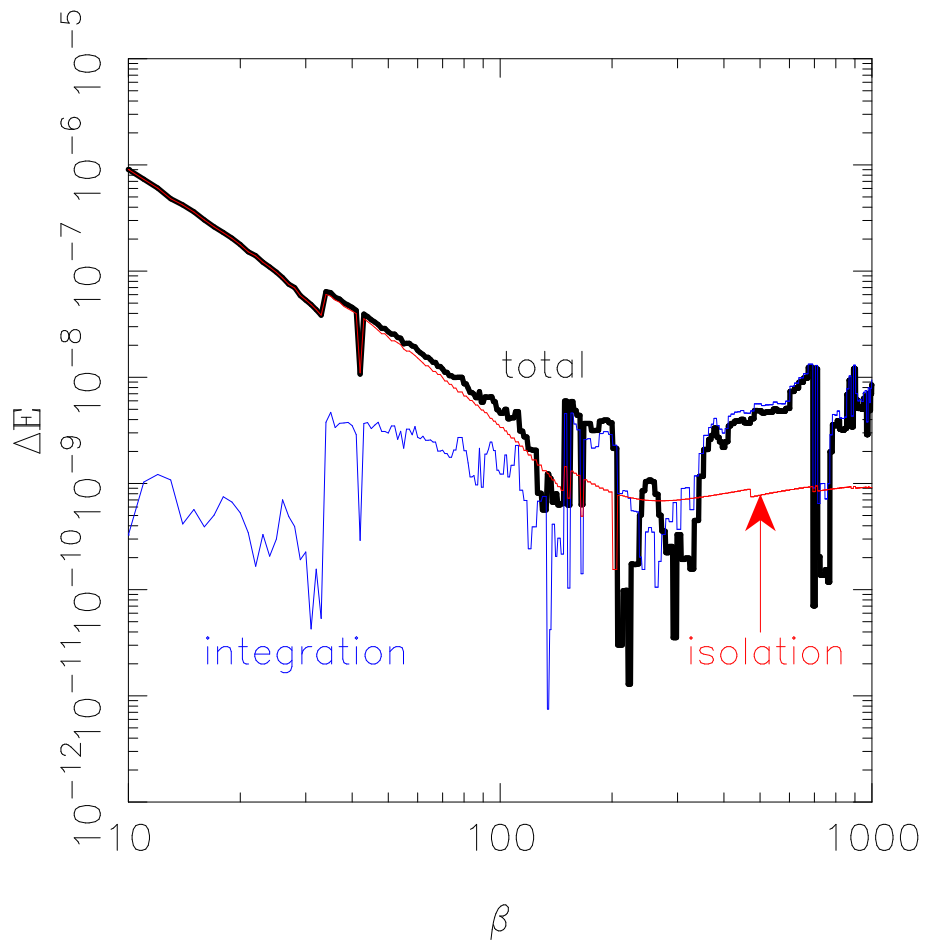


Figure 2.14: The total energy error (black), the energy error from integration (blue), and the energy error from isolation (red) as a function of the pericentric condition β .

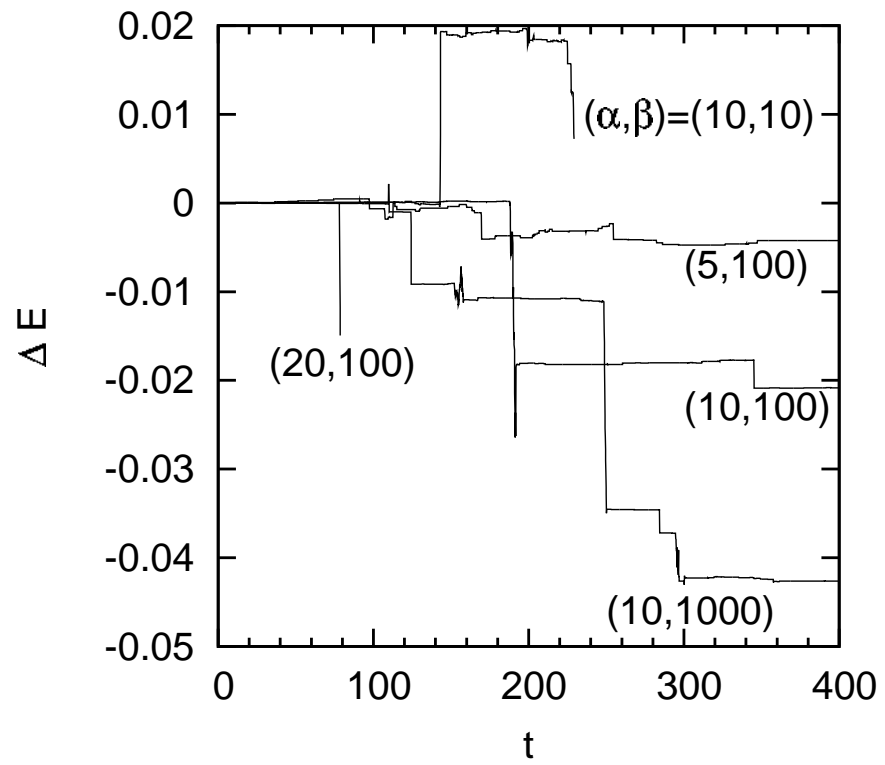


Figure 2.15: The time evolution of the energy error, ΔE of one run at each set of the apocentric condition α , and pericentric condition (β) indicated beside each curve.

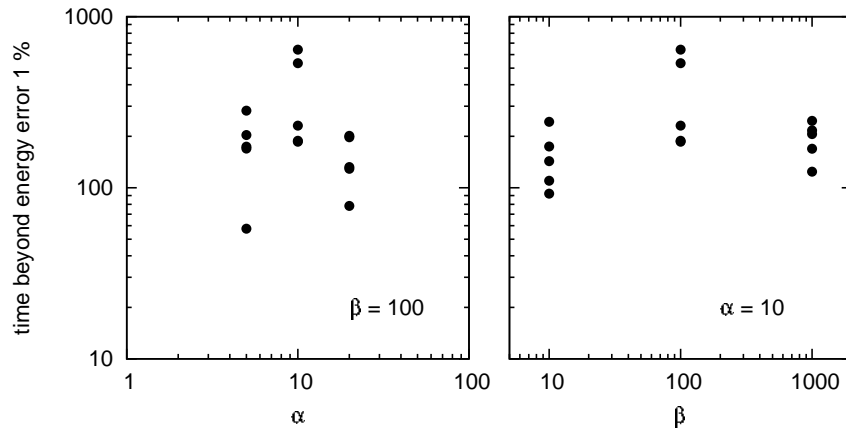


Figure 2.16: The time when energy errors are beyond 1 % as a function of the apocentric condition α (left), and the pericentric condition β (right).

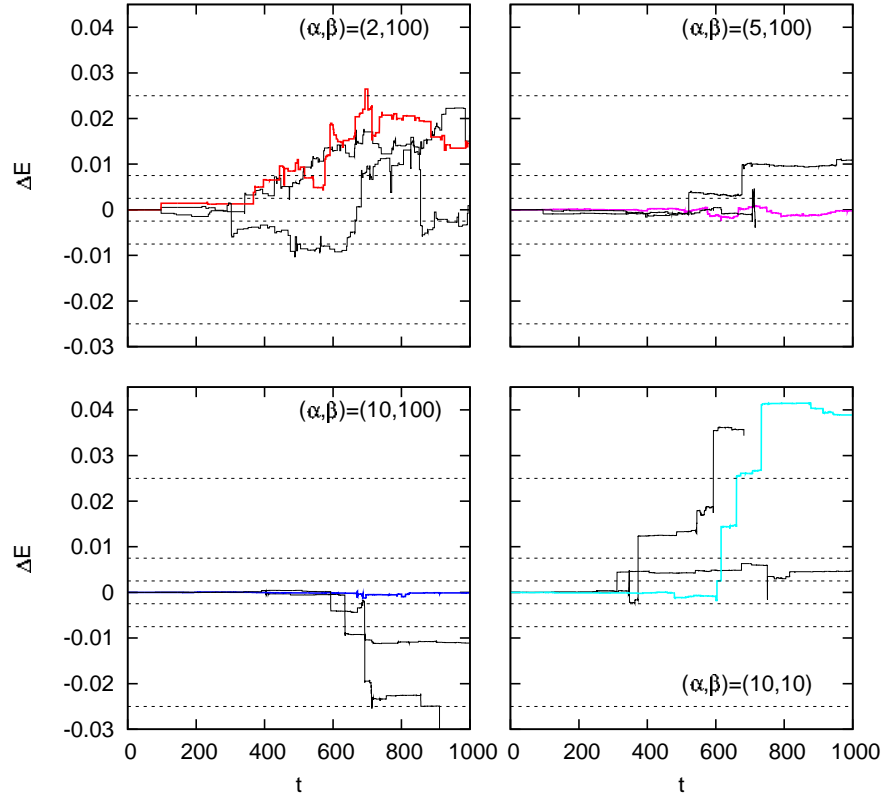


Figure 2.17: Time evolution of energy errors in N -body simulations of clusters with $N = 4096$, and $300kT_0$ primordial binaries. The apocentric and pericentric parameters are $(\alpha, \beta) = (2, 100)$ (upper left), $(5, 100)$ (upper right), $(10, 100)$ (lower left), and $(10, 10)$ (lower right).

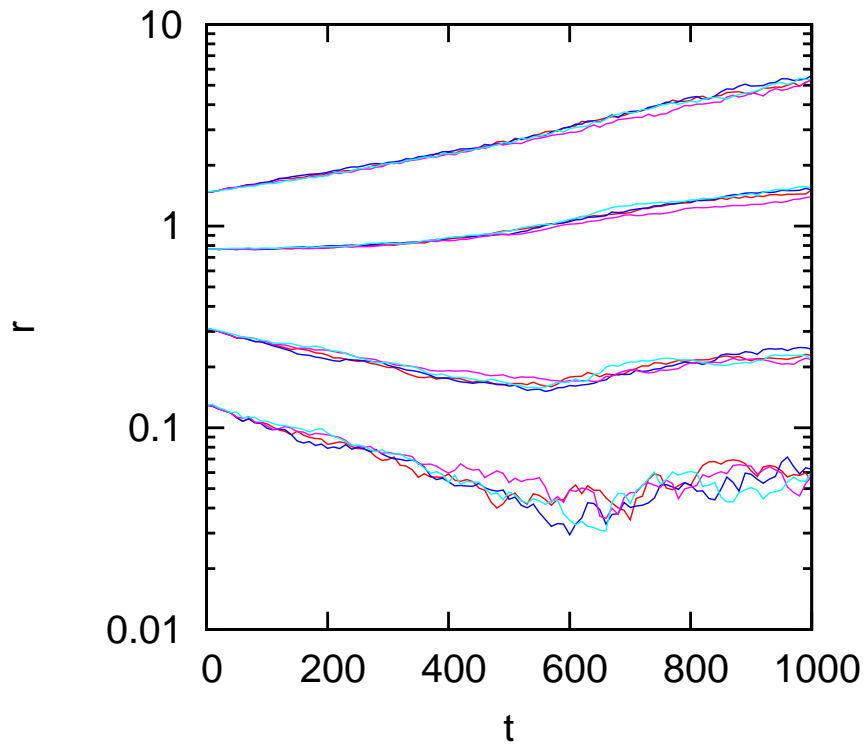


Figure 2.18: Time evolution of 1, 10, 50, and 80 % Lagrange radii from bottom up. The colors of the curves correspond to those of the curves in figure 2.17.

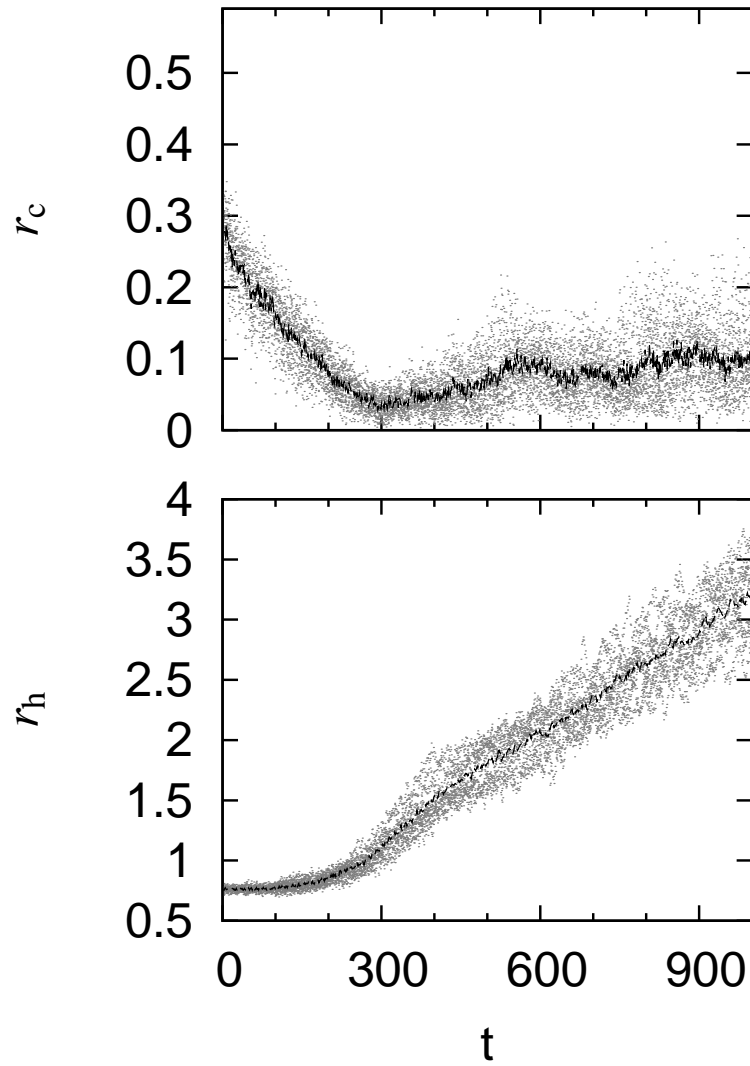


Figure 2.19: The time evolution of Core radius r_c (top), and half-mass radius r_h (bottom). Dots show radii of ten clusters with $N = 1024$ single stars. Solid lines show core radius and half-mass radius averaged over those of the ten clusters with $N = 1024$ single stars at each time.

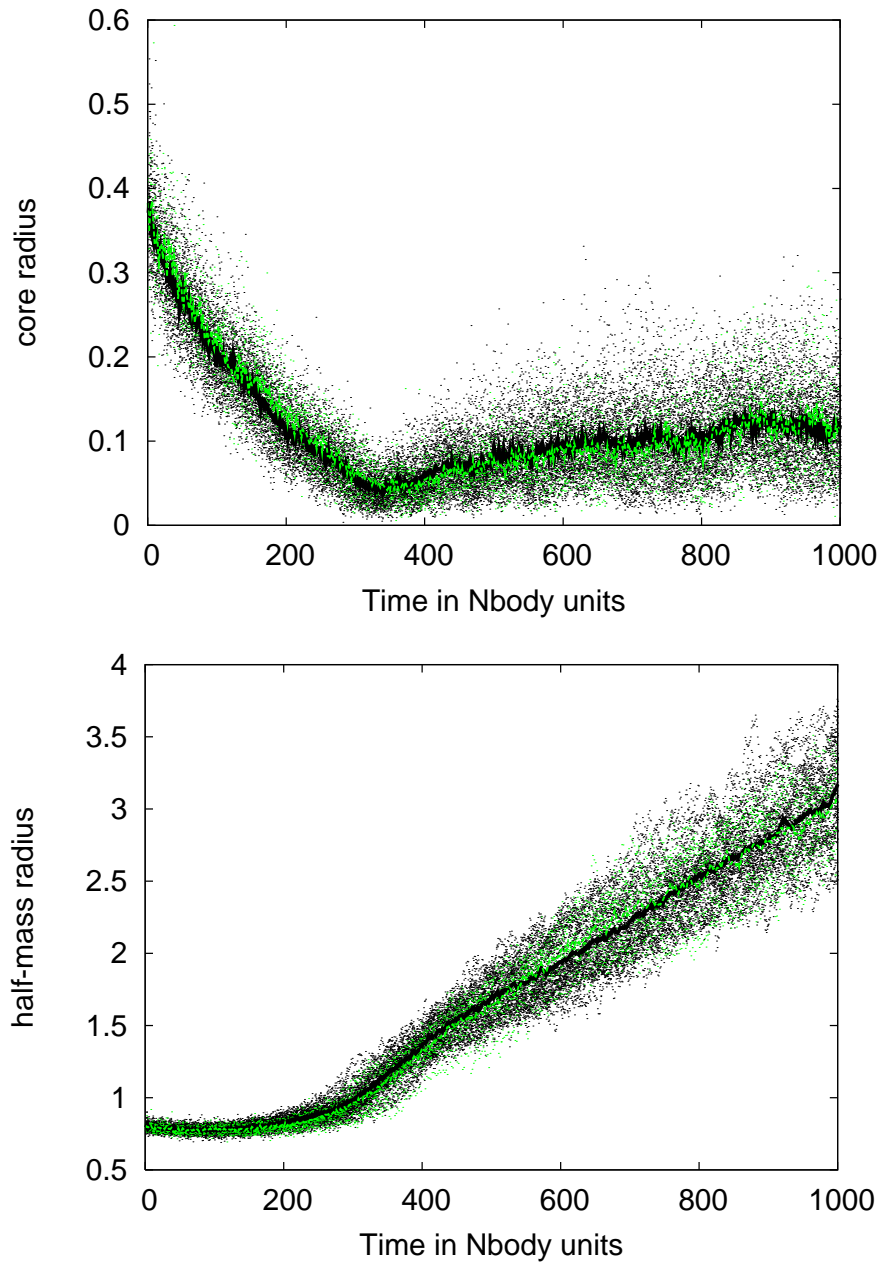


Figure 2.20: The time evolution of Core radius r_c (top), and half-mass radius r_h (bottom). Dots show radii of several ten clusters with $N = 1024$ single stars. Solid lines show core radius and half-mass radius averaged over those of these clusters with $N = 1024$ single stars at each time. All quantities are obtained by Anders et al. (2007), using kira (black), and NBODY4 (green/gray).

Chapter 3

Effect of Hardness of Primordial Binaries on Evolution of Star Clusters

3.1 Simulation methods

I investigate the evolution of star clusters with primordial binaries by means of N -body simulations of point-mass particles. I simulate eleven $N = 16384$ equal-mass cluster models as shown in table 3.1, each of which contains primordial binaries with equal binding energy. These cluster models have different binding energies of the primordial binaries, $E_{\text{bin},0}$, and mass fractions of the primordial binaries, $f_{\text{b},0}$. In table 1, $N_{\text{b},0}$ is the number of the primordial binaries. Additionally, I simulate two reference models as soft and hard limits; an $N = 16384$ equal-mass cluster model without primordial binaries, and a cluster model in which all binaries are replaced by stars with double mass in the case of $f_{\text{b},0} = 0.1$. The fifth and sixth columns in table 3.1 are the mass fraction of the double mass stars, $f_{\text{d},0}$, and the number of the double mass stars, $N_{\text{d},0}$, respectively. We adopt N -body standard units again. For $N = 16384$ cluster, $1kT_0 = 1.0 \times 10^{-5}$.

In all the cases, I use Plummer's model to generate the initial distribution of both single stars and center of mass of primordial binaries in the clusters. The eccentricity distribution of the primordial binaries is thermal distribution, $f(e) = 2e$. The other orbital elements of the primordial binaries, such as the inclination, the longitude of the ascending node, and the argument of pericenter with respect to the clusters, and the phase are distributed at random.

I use an N -body simulation code for the star cluster, GORILLA described in the previous section. The accuracy, and apocentric and pericentric parameters I adopt are shown in table 3.2. The apocentric and pericentric parameters become larger as the binding energy of the primordial binaries are larger, and

the number of the primordial binaries are larger. Energy error per one isolation are larger in binaries with larger binding energy. Hierarchical triple systems are more easily formed in clusters with the larger number of primordial binaries. My N -body simulations are performed on GRAPE-6A, a special-purpose computer designed to accelerate N -body simulations (Fukushige et al. 2005).

Figure 3.1 shows the time evolution of energy errors in the above cluster models. They are within 1 % of the energy that the total binding energy of binaries and high-order hierarchical systems is excluded from the total energy of the cluster (~ 0.0025). Naturally, they are within 1 % of the total energy of the clusters.

3.2 Core evolution and binary properties

We first see the core radii, r_c , and the half-mass radii, r_h , in the $f_{b,0} = 0.1$ models. Figure 3.2 shows the time evolution of the core radii and half-mass radii of seven $f_{b,0} = 0.1$ cluster models, and models No-binary and Double. I calculate the core radii as in Casertano and Hut (1985) with modifications described in McMillan et al.(1990). I calculate the core radii and half-mass radii at each time unit, and average these radii over 10 time units.

In models No-binary, $1kT_0 - 0.1$, and $3kT_0 - 0.1$, the clusters experience deep core collapse, and gravothermal oscillations occur. The core radii at the halts of the core collapse are $0.002 - 0.004$. In models $10kT_0 - 0.1$, $30kT_0 - 0.1$, and $100kT_0 - 0.1$, the core collapse stops halfway, although the cores contract more slowly. The core radii at the halts of the core collapse are $0.05 - 0.1$. In models $300kT_0 - 0.1$, and Double, the clusters also experience deep core collapse. In model Double, gravothermal oscillations occur. The core radii at the halts of the core collapse are $0.005 - 0.02$. Among the clusters that experience deep core collapse, the times when the core collapse stops and core bounce occurs are different. In models No-binary, and $1kT_0 - 0.1$, $t \sim 3400$, in model $3kT_0 - 0.1$, $t \sim 4700$, and in models $300kT_0 - 0.1$, and Double, $t \sim 1700 - 2100$.

Next, we see the evolution of binary properties throughout the rest of this subsection. Figure 3.3 shows in the thick curves the increase of the total binding energy of the binaries, $\Delta E_{\text{bin,tot}}(t)$, in the $f_{b,0} = 0.1$ models, and models No-binary and Double. The arrows indicate the times when the core collapse stops. The increase $\Delta E_{\text{bin,tot}}(t)$ is given by

$$\Delta E_{\text{bin,tot}}(t) = \sum_i^{N_b(t)} E_{\text{bin},i}(t) - \sum_i^{N_b(0)} E_{\text{bin},i}(0), \quad (3.1)$$

where $E_{\text{bin},i}(t)$ is the binding energy of i -th binary at time t , $N_b(t)$ is the number of the binaries at time t including binary escapers, and $\Delta E_{\text{bin,tot}}(t)$ corresponds to energy released by all the binaries. We can see that, in models No-binary, $1kT_0 - 0.1$, and Double, the binaries do not release energy until the core collapse stops. In model $3kT_0 - 0.1$, the binaries release energy from $t \sim 1000$. In the other models, the binaries release energy from $t \sim 0$.

Figure 3.3 shows in the thin curves the time evolution of the total energy of escapers, $E_{\text{esc,tot}}(t)$, in the $f_{\text{b},0} = 0.1$ models, and models No-binary and Double. The escapers are defined as stars, regardless of single stars, binaries, or hierarchical triple systems, satisfying both conditions as follows.

- (a) The sum of the kinetic and potential energy of the single star (or the center of mass of the binary or hierarchical triple system) is positive.
- (b) The distance between the star and the center of the cluster is more than 40 length units.

We can see that, in models No-binary, $1kT_0 - 0.1$, and Double, the total energy of escapers is small just before the halts of the core collapse, such that $E_{\text{esc,tot}}(t) \sim 1 \times 10^{-3}$. In model $300kT_0 - 0.1$, the thin curve is almost overlapped with the thick curve, which indicates that the escapers carry away almost all energy released by the binaries. In other models, $E_{\text{esc,tot}}(t)$ at the halts of core collapse is larger than those of models No-binary, $1kT_0 - 0.1$, and Double by an order of magnitude.

Figure 3.4 shows the time evolution of the number of binaries, N_{b} , in the models $f_{\text{b},0} = 0.1$, No-binary, and Double. For model Double, the number of the double mass stars is also plotted. In each panel, the thick curve shows the number of binaries (or double mass stars) within the cluster, and the thin curve shows the total number of binaries (or double mass stars) including escapers. The arrows indicate the times when the core collapse stops.

We can see that, in model No-binary, the binaries increase after deep core collapse. These binaries are the three-body binaries. In models $1kT_0 - 0.1$, and $3kT_0 - 0.1$, the numbers of the binaries rapidly decrease before deep core collapse. After deep core collapse, the total numbers of binaries including binary escapers increase. In these models, the three-body binaries are also formed. In models $10kT_0 - 0.1$, $30kT_0 - 0.1$, $100kT_0 - 0.1$, and $300kT_0 - 0.1$, the numbers of the binaries monotonically decrease. In model Double, the three-body binaries are formed after deep core collapse. The total number of these binaries including the escapers is 27 at $t = 5000$. The number of the binaries composed of the two double mass stars is 25. Two binaries are composed of one double and one single mass stars. Nearly all binaries are composed of the double mass stars. The number of the binaries within the cluster is 2, both of which are composed of the two double mass stars. In this model, the number of the double mass stars monotonically decreases.

Figure 3.5 shows the number distribution, N_{b} , of the binding energy of the binaries, E_{bin} , in unit of kT_0 in the $f_{\text{b},0} = 0.1$ models. The size of energy bin is 0.1 in $\log_{10} E_{\text{bin}}$, where the unit of E_{bin} is kT_0 . In models $1kT_0 - 0.1$, and $3kT_0 - 0.1$, I choose $t = 3000$, before which the deep core collapse has occurred, because I want to exclude three-body binaries. In the other models, I choose the times at which I stop the simulations. In all models, the peaks around the initial binding energies, E_{bin} , can be seen. The distributions of the binding energy spread towards the larger sides.

In figure 3.6, dots show the binding energies and distances from of the cluster center of all the binaries in models $1kT_0-0.1$, $3kT_0-0.1$, $10kT_0-0.1$, $30kT_0-0.1$, $100kT_0-0.1$, and $300kT_0-0.1$ at the time indicated in the panels. The dashed lines show the half-mass radii and twice the core radii at the time. Within the half-mass radii, the distributions of the binding energies are greatly changed from those at the initial time in all the models except models $1kT_0-0.1$, $3kT_0-0.1$, $10kT_0-0.1$, and $30kT_0-0.1$. The distributions of the binding energies in these models are similar. The distributions center on about $100kT_0$, and range from more than $10kT_0$ to $300kT_0$. On the other hand, outside the half-mass radii of these models, the distributions of the binding energies are little changed from the initial time, which is consistent with the fact that the peaks of the distributions are around the initial binding energies. In models $100kT_0-0.1$ and $300kT_0-0.1$, even inside the half-mass radii, the distributions of the binding energies are not changed. This is because the cross sections of the binaries for binary-single and binary-binary encounters are too small to change their binding energies during my simulation time.

Figure 3.7 shows the time evolution of the mass fraction, f_b , of the binaries inside the core radii (upper curves) and half-mass radii (lower curves) in the $f_{b,0} = 0.1$ models, and model No-binary. For model Double, mass fraction, f_d , of the double mass stars are shown. In model $1kT_0-0.1$, both the fractions inside the core and half-mass radii decrease from 0.1 to 0.02 at the time when the deep core collapse occurs. In model $3kT_0-0.1$, the fraction inside the core radius increases up to 0.3 at $t \sim 1000$, and decreases down to ~ 0.04 at the time when the deep core collapse occurs. In models $10kT_0-0.1$, $30kT_0-0.1$, $100kT_0-0.1$, $300kT_0-0.1$, and Double, the fraction inside the core radii increases until the core collapse stops. After that time, the fraction stops increasing.

Figure 3.8 shows the time evolution of the mean kinetic energy of the single stars, $E_{\text{kin,ave,s}}$, inside the core radii (solid curves) and the half-mass radii (dashed curves) in the $f_{b,0} = 0.1$ models, and models No-binary and Double. In models No-binary, $1kT_0-0.1$, $300kT_0-0.1$, and Double, at the moment of core collapse, the mean kinetic energies of the single stars in the cores increase about two times more than those at the initial time. On the other hand, they nearly keep constant during the evolution in models $3kT_0-0.1$, $10kT_0-0.1$, $30kT_0-0.1$, and $100kT_0-0.1$.

Figure 3.9 shows the time evolution of the mean kinetic energy of the binaries, $E_{\text{kin,ave,b}}$, inside the core radii in the $f_{b,0} = 0.1$ models. I do not show those inside the half-mass radii, since they are nearly the same as inside the core radii. The fluctuation is large in model $1kT_0-0.1$, since the number of the binaries is small. Except model $1kT_0-0.1$, the mean kinetic energy of the binaries in the core keep nearly constant during the evolution. In model $1kT_0-0.1$, the mean kinetic energy largely increases at the deep core collapse.

3.3 Interpretation

On both softer (models No-binary, $1kT_0 - 0.1$, and $3kT_0 - 0.1$) and harder (models $300kT_0 - 0.1$, and Double) hardness, the clusters undergo deep core collapse. Here, binaries with small binding energy are soft, and those with large binding energy are hard. On the other hand, in the intermediate hardness (models $10kT_0 - 0.1$, $30kT_0 - 0.1$, and $100kT_0 - 0.1$), the clusters exhibit shallower core collapse. The depth of the core collapse depends on the amount of energy heating core generated by the primordial binaries. The larger the amount of energy is, the shallower core collapse becomes, and vice versa.

The amount of the energy heating the core depends on whether the primordial binaries become harder or not through binary-single and binary-binary encounters, and whether the single stars and binaries heated by such encounters are ejected or not from the clusters. Whether the binaries become harder or not depends on whether the binding energy of the binaries is larger or not than a critical energy $E_{\text{crit,H}}$, which, in this case, corresponds to the average kinetic energy of the surrounding single stars, $E_{\text{kin,ave,s}}$ (Heggie's law). If $E_{\text{bin}} \lesssim E_{\text{crit,H}} \sim E_{\text{kin,ave,s}}$, the binaries are on average destroyed through binary-single encounters. Therefore, the binaries cannot heat the core. If $E_{\text{bin}} \gtrsim E_{\text{crit,H}}$, the binaries become harder and harder through series of binary-single encounters, and then heat the core. In Plummer's model, which is the initial condition of my clusters, the average kinetic energy of the single stars is about $2.5kT_0$, which can be seen in figure 3.8. Therefore,

$$E_{\text{crit,H}} \sim E_{\text{kin,ave,s}} \sim 2.5kT, \quad (3.2)$$

where kT is the average stellar kinetic energy in the whole cluster at a given time, and I assume that the structure of the cluster at any time is similar to those at the initial time.

Whether the single stars and binaries heated through encounters are ejected or not depends on whether the kinetic energies transformed from the binding energies of binaries are larger or not than the potential depth of the whole cluster. The increase of the binding energy at single binary-single encounter, ΔE_{bin} , is on average $\Delta E_{\text{bin}} \simeq 0.4E_{\text{bin}}$ (Heggie 1975). According to conservation of momentum, two-third of the energy released by the binaries goes to the single star, and the rest goes to the binary, on average. The condition to eject both the single star and binary is $\Delta E_{\text{bin}}/3 > 2m|\Phi_c|$, where m is the mass of the single mass stars, and Φ_c is the potential of the core. If I define a critical energy for ejection as $E_{\text{crit,E}}$, $0.4E_{\text{crit,E}}/3 > 2m|\Phi_c|$. In Plummer's model, $m|\Phi_c| \simeq 10kT$. Therefore, the ejection occurs when

$$E_{\text{bin}} > E_{\text{crit,E}} \sim \frac{6}{0.4}m|\Phi_c| = 150kT. \quad (3.3)$$

In summary, whether primordial binaries can heat the core or not are different among three ranges of hardness divided by two critical hardness $E_{\text{crit,H}}$ and $E_{\text{crit,E}}$: (a) $E_{\text{bin}} \lesssim E_{\text{crit,H}}$, (b) $E_{\text{crit,H}} \lesssim E_{\text{bin}} \lesssim E_{\text{crit,E}}$, and (c) $E_{\text{bin}} \gtrsim E_{\text{crit,E}}$,

which are illustrated in figure 3.10. Here, we can regard kT at the halt of the core contractions as kT_0 in all the model (figure 3.8). If $E_{\text{bin}} \lesssim E_{\text{crit,H}}$ (soft range), the primordial binaries are destroyed through encounters, and can not heat the core. If $E_{\text{crit,H}} \lesssim E_{\text{bin}} \lesssim E_{\text{crit,E}}$ (intermediate hard range), the primordial binaries become harder and harder and continually heat the core. If $E_{\text{bin}} \gtrsim E_{\text{crit,E}}$ (super hard range), the primordial binaries release their binding energy to the surrounding stars and binaries, but the stars and binaries are ejected from the cluster, and then the primordial binaries cannot heat the core. In the following sub-subsections, we see the simulation results for each range of hardness.

3.3.1 Soft range

In the soft range, $E_{\text{bin}} \lesssim E_{\text{crit,H}} (\sim 2.5kT)$, the primordial binaries are destroyed through encounters, and cannot heat the core. We can see, in figure 3.4 (the second left panel), the number of binaries for model $1kT_0 - 0.1$ rapidly decreases, and, in figure 3.3 (the second left panel), primordial binaries do not release energy from the beginning. After then, their evolutions are almost identical to the case without primordial binaries, and lead to deep core collapse. Figure 3.2 and 3.3 (the first and second left panels) show that the core evolution and energy generations are very similar between models No-binary and $1kT_0 - 0.1$.

Model $3kT_0 - 0.1$ exhibits a mixed behavior between soft and intermediate hard ranges. While the number of binaries rapidly decreases, shown in figure 3.4 (the third left panel), the binding energy are continually released, shown in figure 3.3 (the third left panel). A population whose binding energy is harder than initial value can be seen in figure 3.5 (the second left upper panel). Although that heating is not so large to stop core collapse, it makes the time to the core collapse longer, compared to the case without primordial binaries, shown in figure 3.2 (the first, second, and third left panels). Note that at the very beginning the number of binary in the core increase, shown in figure 3.7 (the third left panel), and then turns to decreasing, which is due to mass segregation of single star and binary, and sinking of binary to the core.

3.3.2 Intermediate hard range

In the intermediate range, $E_{\text{crit,H}} (\sim 2.5kT) \lesssim E_{\text{bin}} \lesssim E_{\text{crit,E}} (\sim 150kT)$, the primordial binaries continually heat the core, and becomes harder and harder. We can see in figure 3.3 (the fourth, fifth, and sixth left panels) the primordial binaries release the binding energy, and in figure 3.5 (panels $10kT_0 - 0.1$, $30kT_0 - 0.1$, and $100kT_0 - 0.1$), populations whose binding energy become harder from initial values can be seen. The continually released heat halts the core collapse halfway.

3.3.3 Super hard range

In the super hard range, $E_{\text{bin}} \gtrsim E_{\text{crit,E}} (\sim 150kT)$, the kinetic energy transformed from binding energy of primordial binaries through encounters is so large to be ejected from whole cluster immediately, and the primordial binaries cannot heat the core. Figure 3.3 (the second right panels) shows the released binding energy in total (in the thick curves), and those of escapers (in the thin curve) are very close in model $300kT_0 - 0.1$, which means almost all released energy from the primordial binaries is brought away from the cluster by the escapers. Therefore, the primordial binaries can neither heat the core, nor stop core collapse. Their evolutions become similar to the case in which binaries are replaced by the double mass stars, which is shown in figure 3.2 (first and second right panels). Note that the energy generation rate itself does not depend on the binding energy, E_{bin} , in the super hard range. While energy generation through a single encounter becomes larger for larger E_{bin} , encounter rate becomes smaller. Both are canceled out, which shown in Heggie and Hut (1993) quantitatively.

3.4 Comparison of core size between theoretical estimate and simulation results

In this section, I investigate whether the core radii of the clusters after halt of core contraction in the above simulations is in agreement with the core radii obtained by theoretical estimates or not. In section 3.4.1, I describe the theoretical formula of the core radii. I compare the theoretical formula with the clusters at the time when core contractions stop in my simulation in section 3.4.2, and with the clusters after core contractions stop in my simulation in section 3.4.3.

3.4.1 Theoretical formula

I theoretically estimate core size at the halt of core contraction, using energy balance between the energy carried away by stars escaping from the cluster at each unit time, dE_{h}/dt , and the energy which is provided for the core through binary interactions at each unit time, dE_{c}/dt , such as

$$\frac{dE_{\text{h}}}{dt} = \frac{dE_{\text{c}}}{dt}. \quad (3.4)$$

The argument here and hereafter is based on VC94.

The energy carried away by stars escaping from the cluster at each unit time, dE_{h}/dt , is given by

$$\frac{dE_{\text{h}}}{dt} = \frac{|E|}{\gamma t_{\text{rh}}} \approx \frac{0.2 GM^2}{\gamma t_{\text{rh}} r_{\text{h}}}, \quad (3.5)$$

where t_{rh} is the half-mass relaxation time, expressed as equation (1.1), and γ is a numerical coefficient relating the energy outflow rate to the half-mass relaxation time. I use the relation $\gamma \approx 10$, and $|E| \sim 0.2GM^2/r_{\text{h}}$, which comes from virial

theorem, $|E| \sim GM^2/4r_v$, where r_v is the virial radius, and $r_h \sim 0.8r_v$ in Plummer's model.

The energy which is provided for the core by binary interactions at each unit time, dE_c/dt , is expressed as

$$\frac{dE_c}{dt} = V_c \frac{G^2 m^3}{v_{s,c}} n_c^2 (A_{bs} + A_{bb}) \quad (3.6)$$

where V_c is the core volume, $v_{s,c}$ is one dimensional velocity dispersion of single stars in the core, n_c is the total number density of the single stars and binaries in the core, and A_{bs} and A_{bb} are, respectively, dimensionless efficiency factors for energy provided for a cluster through binary-single and binary-binary interactions. The core volume, V_c , is given by $V_c = (4\pi/3)\lambda r_c^3$, where λ is a free parameter nearly equal to unity.

Substituting equations (3.5) and (3.6) into equation (3.4), I express the ratio of the core to half-mass radii at the halt of core collapse as

$$\frac{r_c}{r_h} = \frac{0.0196\lambda}{\log_{10}(0.4N)} \left(\frac{v_{s,c}}{v_h} \right)^3 \left(\frac{\gamma}{10} \right) (2 - f_{b,c})^4 (A_{bs} + A_{bb}) \quad (3.7)$$

where $f_{b,c}$ is mass fraction of binaries in the core, v_h is the one dimensional half-mass velocity dispersion, and $|E| \sim 3Mv_h^2/2$ i.e. $3v_h^2/2 \sim GM/5r_h$. Here, I define the core radius as

$$r_c = \sqrt{\frac{9v_c^2}{4\pi G\rho_c}} = \sqrt{\frac{9v_{s,c}^2(2 - f_{b,c})^2}{16\pi Gmn_c}}, \quad (3.8)$$

where $v_c^2 = v_{s,c}^2(2 - f_{b,c})/2$ and $\rho_c = 2mn_c/(2 - f_{b,c})$ are, respectively, the average velocity dispersion and mass density in the core.

Such dimensionless efficiency factors are, respectively, expressed as

$$A_{bs} = \left(\frac{2(1 - f_{b,c})}{2 - f_{b,c}} \right) \left(\frac{f_{b,c}}{2 - f_{b,c}} \right) \int f(x) [g(x)h(x) + g'(x)] dx, \quad (3.9)$$

and

$$A_{bb} = \frac{1}{2} \left(\frac{f_{b,c}}{2 - f_{b,c}} \right)^2 \int f(x_1)f(x_2)G(x_1, x_2)H(x_1, x_2)dx_1dx_2, \quad (3.10)$$

where x , x_1 , and x_2 are the binding energy of the binaries in the unit of kT . The function $f(x)$ is the distribution function of the binding energies of the binaries in the core. The functions $g(x)$, $g'(x)$ and $G(x_1, x_2)$ are, respectively, the dimensionless hardening rates of the binary with the binding energy x which is not destroyed in a sea of single stars, the binary with the binding energy x which is destroyed in a sea of single stars, and the binary with the binding energy x_1 in a sea of binaries with the binding energy x_2 . The functions $h(x)$ and $H(x_1, x_2)$ are, respectively, the efficiency ratios of heating of the core to hardening of the binaries at each interaction between a single star and a binary

with the binding energy x , and that between binaries with the binding energies x_1 , and x_2 . The $h(x)$ and $H(x_1, x_2)$ become less than unity when single stars and binaries involved with encounters are ejected from the cluster immediately after the encounters. When the binaries are destroyed through binary-single encounters, $h(x) = 1$, since they are hardly ejected.

The dimensionless hardening rate $g(x)$ is expressed as

$$g(x) = 1.66 \left(\frac{x}{C} \right)^{-1} \int R_{\text{bs}}(x/C, \Delta) \Delta d\Delta, \quad (3.11)$$

where R_{bs} is the dimensionless rate of the interactions that the binary with the binding energy x hardens to the binding energy $(1 + \Delta)x$ in a sea of single stars, and $C (= 1.7)$ is a correction factor in order to set the unit of the binding energy to be $kT_c (= 1.7kT)$, which is one dimensional kinetic energy of single stars in the core. The integral of the dimensionless rate R_{bs} over Δ is described in equation (49) of Heggie and Hut (1993), and obtained as a function of the binding energy of the binary in the unit of kT_c .

The dimensionless hardening rate $g'(x)$ is expressed as

$$g'(x) = -1.66 \left(\frac{x}{C} \right)^{-1} R'_{\text{bs}}(x/C), \quad (3.12)$$

where R'_{bs} is the dimensionless rate of the interactions that the binary with the binding energy x is destroyed in a sea of single stars. The dimensionless rate R'_{bs} is described in equation (5.12) of Hut and Bahcall (1983), and also obtained as a function of the binding energy of the binary in the unit of kT_c .

The dimensionless hardening rate $G(x_1, x_2)$ is expressed as

$$G(x_1, x_2) = 1.66 \left(\frac{x_1 + x_2}{C} \right)^{-1} R_{\text{bb}}(x_1, x_2) \Delta, \quad (3.13)$$

where R_{bb} is the dimensionless rate of the interaction that the binary with the binding energies x_1 hardens to the binding energy $(1 + \Delta)(x_1 + x_2)$ in a sea of binaries with the binding energy x_2 when $x_1 > x_2$, and the binaries with the binding energy x_2 are destroyed. We consider only binary-binary interaction which results in the destruction of the softer binary, since Mikkola (1983a; 1983b; 1984a; 1984b) showed that the binary-binary interaction not involving the destruction of one binary has small contribution to the heating of the cluster. The dimensionless rate is averaged over Δ , since the number of binary-binary scattering experiments is much smaller than that of binary-single scattering experiments. The average of Δ in binary-binary interactions is about 0.5 (Mikkola).

The dimensionless rate R_{bb} is expressed as

$$R_{\text{bb}}(x_1, x_2) = \frac{\sqrt{2}}{3} \frac{1}{\pi a^2 v_{s,c}} \int v \sigma j(v) dv, \quad (3.14)$$

where a is semi-major axis of the binary with the binding energy $x_1 + x_2$, v is the relative velocity between binaries, $j(v)$ is the distribution of the relative velocity

between the binaries, and σ is cross section of the binary-binary interactions. Assuming that the velocity distribution of the single stars and binaries in the core is isotropic Maxwellian, and equipartition is achieved: $v_{b,c} = (1/\sqrt{2})v_{s,c}$, where $v_{b,c}$ is one dimensional velocity dispersion of the binaries, the relative velocity dispersion between the binaries $\sqrt{2}v_{b,c}$ is $v_{s,c}$, and $j(v)$ is expressed as

$$j(v) = \left(\frac{2}{\pi}\right)^{\frac{1}{2}} \frac{v^2}{v_{s,c}^3} \exp\left(-\frac{v^2}{2v_{s,c}^2}\right). \quad (3.15)$$

The cross section of the binary-binary interaction σ is expressed

$$\sigma = S \frac{G^2 m^3}{v^2 E_{\text{bin},2}}, \quad (3.16)$$

where $E_{\text{bin},2}$ is the binding energy of the softer binary, expressed as $x_2 m v_{s,c}^2 / C$, and S is a dimensionless coefficient. The cross section σ is derived, based on equation (2.7) in Gao et al. (1991). The dimensionless coefficient S depends on the relation between the binding energies of the binaries, x_1 and x_2 , as follows:

$$S = \begin{cases} 25.2 & (x_1 \sim x_2) \\ 15.9 & (x_1 \gg x_2) \end{cases}. \quad (3.17)$$

In summary, the dimensionless rate R_{bb} is expressed as

$$R_{\text{bb}}(x_1, x_2) = 0.479S \left(\frac{x_1 + x_2}{C}\right) \left(\frac{(x_1 + x_2)^2}{x_2}\right), \quad (3.18)$$

and the dimensionless hardening rate $G(x_1, x_2)$ is expressed as

$$G(x_1, x_2) = 0.398S \frac{x_1 + x_2}{x_2}. \quad (3.19)$$

I describe the forms of $h(x)$ and $H(x_1, x_2)$. When I obtain $h(x)$, I assume that at every binary-single encounter the binary increases its binding energy, E_{bin} , by $0.4E_{\text{bin}}$, and $2/3$ of the increment goes to the kinetic energy of the single star and the rest to the kinetic energy of the center of mass of the binary. The increment is the average value over all the binary-single encounters, which has been obtained by Heggie (1975). The single star will be ejected when $E_b/m|\Phi_c| > 15/4$. The binary will be ejected when $E_b/m|\Phi_c| > 15$. Since the ejection results in the mass loss of the core, the binding energy of the core decreases, i.e. the core is heated. The amount of the heating is $m|\Phi_c|$ when a single star is ejected, and $2m|\Phi_c|$ when a binary is ejected. Therefore, I can express $h(x)$ as

$$h(x) = \begin{cases} 1, & \text{if } x < \frac{15}{4} \frac{m|\Phi_c|}{kT}; \\ \frac{1}{3} + \frac{m|\Phi_c|}{\Delta E_{\text{bs}}}, & \text{if } \frac{15}{4} \frac{m|\Phi_c|}{kT} < x < 15 \frac{m|\Phi_c|}{kT}; \\ \frac{3m|\Phi_c|}{\Delta E_{\text{bs}}}, & \text{if } x > 15 \frac{m|\Phi_c|}{kT}. \end{cases} \quad (3.20)$$

I set $m|\Phi_c| = 10kT$ as described in section 3.2. Then, $h(x)$ is expressed as

$$h(x) = \begin{cases} 1, & \text{if } x < 38 ; \\ \frac{1}{3} + \frac{25}{x}, & \text{if } 38 < x < 150; \\ \frac{75}{x}, & \text{if } x > 150. \end{cases} \quad (3.21)$$

For $H(x_1, x_2)$, I assume that at every binary-binary interaction, $0.5(E_{\text{bin},1} + E_{\text{bin},2})$ is liberated, either binary is destroyed, and its $1/4$ goes to the kinetic energy of the center of mass of the surviving binary, and its $3/8$ goes to each single star which is a component of the destroyed binary. Then, $H(x_1, x_2)$ is expressed as

$$H(x_1, x_2) = \begin{cases} 1, & \text{if } (x_1 + x_2) < \frac{16}{3} \frac{m|\Phi_c|}{kT} ; \\ \frac{1}{4} + \frac{2m|\Phi_c|}{\Delta\bar{E}_{\text{bb}}}, & \text{if } \frac{16}{3} \frac{m|\Phi_c|}{kT} < (x_1 + x_2) < 16 \frac{m|\Phi_c|}{kT}; \\ \frac{4m|\Phi_c|}{\Delta\bar{E}_{\text{bb}}}, & \text{if } (x_1 + x_2) > 16 \frac{m|\Phi_c|}{kT}, \end{cases} \quad (3.22)$$

and substituting $m|\Phi_c| = 10kT$ I finally obtain

$$H(x_1, x_2) = \begin{cases} 1, & \text{if } (x_1 + x_2) < 53 ; \\ \frac{1}{4} + \frac{40}{x_1 + x_2}, & \text{if } 53 < (x_1 + x_2) < 160; \\ \frac{80}{(x_1 + x_2)}, & \text{if } (x_1 + x_2) > 160. \end{cases} \quad (3.23)$$

In figure 3.11 and 3.12, solid curves show the dimensionless heating rate of binary-single encounters in which the binaries survive ($g(x)h(x)$), and binaries are destroyed ($g'(x)$) as a function of the dimensionless binding energy of the binary, x , and those of binary-binary encounters ($G(x_1, x_2)H(x_1, x_2)$) as a function of the dimensionless binding energy of the softer binary, x_2 , where the binaries have the dimensionless binding energies x_1 and x_2 , and $x_1 = x_2$, $x_1 = 10x_2$, and $x_1 = 100x_2$. The solid curves except that of $g'(x)$ have two turnoff points. In more than x or x_2 of the turnoff point with the smaller x or x_2 , single stars which encounter with binaries, or was binary components destroyed by binary-binary encounters are ejected from the clusters. In more than x or x_2 of the turnoff point with the larger x or x_2 , binaries involved with binary-single and binary-binary encounters are ejected from the clusters.

From $g(x)h(x)$ in figure 3.11, with the dimensionless binding energy x increasing the dimensionless heating rate increases when $x < 50kT$, and decreases when $x > 50kT$. From $g'(x)$ in figure 3.11, binary-single encounters in which the binaries are destroyed do not contribute to the dimensionless heating rate of binary-single encounters when the dimensionless binding energy is more than $10kT$.

From figure 3.12, we see that if the dimensionless binding energy of the softer binary x_2 is more than about $50kT$, the dimensionless heating rate in

$x_1 = x_2$ is larger than those in $x_1 = 10x_2$ and $x_1 = 100x_2$. This is due to the dimensionless coefficient S in equation (3.16). The cross section of the binary-binary interaction σ is large if $x_1 \sim x_2$, and small if $x_1 \gg x_2$. Note that the dimensionless heating rate of binary-binary encounters is not correct if x_2 is soft, i.e. $x_2 < 3kT$. This is because the cross section of the binary-bury interaction σ is applicable only when the two binaries are hard.

3.4.2 Instant of halt of core contraction

I compare the core sizes of the clusters in my simulations with the core sizes derived from equation (3.7) in which the unit of the binding energies kT is equal to kT_0 , and the distribution functions of the binding energies $f(x)$ are δ functions. The theoretical formula of the core sizes is expressed as

$$\begin{aligned} \frac{r_c}{r_h} &= \frac{0.0196\lambda}{\log_{10}(0.4N)} \left(\frac{v_{s,c}}{v_h} \right)^3 \left(\frac{\gamma}{10} \right) (2 - f_{b,c})^4 \\ &\times \left\{ \frac{2f_{b,c}(1 - f_{b,c})}{(2 - f_{b,c})^2} [g(x)h(x) - g'(x)] \right. \\ &\left. + \frac{1}{2} \left(\frac{f_{b,c}}{2 - f_{b,c}} \right)^2 G(x_1, x_2)H(x_1, x_2) \right\}. \end{aligned} \quad (3.24)$$

Figure 3.13 shows the distributions of the binding energies of binaries in the whole clusters of models $10kT_0 - 0.1$, $30kT_0 - 0.1$, $100kT_0 - 0.1$, and $300kT_0 - 0.1$ at the time indicated in these panels, i.e. the time when the core contractions stop. All the distributions of the binding energies have steep peaks at the initial binding energies. Even inside the core radii, all the distributions of the binding energies may do so. The distributions of the binding energies of binaries in the core at the halt of the core contraction can be regarded as the initial distributions, i.e. δ functions.

The average kinetic energies of single stars within the half-mass radii are not different from the initial time to the halt of the core contraction (figure 3.8), which is confirmed by little changes of the half-mass radii during this time (figure 3.2). Therefore, we can regard $1kT = 1kT_0$.

In figure 3.14, The big black dots show r_c/r_h at the halts of core collapse of the clusters obtained in my simulations, as a function of the dimensionless binding energy of the primordial binaries at the initial time. The numbers beside the dots show the mass fraction of the binaries in the core at that time, obtained from figure 3.7. The error bars indicate the amplitude of gravothermal oscillations. The dots are the geometric means of the maximum and minimum r_c/r_h in the gravothermal oscillations. Solid curves show equation (3.24) when $f_{b,c} = 0.04, 0.1, 0.4, 1$ as a function of the dimensionless binding energy $x[kT_0]$. The numbers in italic format beside the curves show the mass fraction of the binaries in the core, $f_{b,c}$. Here, I adopt $v_s/v_h = \sqrt{2}$, and $\gamma = 10$. I adopt $\lambda = 0.45$ so that the simulation results of model $30kT_0 - 0.1$ agree with $f_{b,c} = 0.5$.

In the binding energy with less than $E_{\text{bin}} \lesssim E_{\text{kin,ave,s}} \sim 2.5kT_0$, the curves are not reliable, and should fall down to zero.

I compare the theoretical curves with the simulation results of models $10kT_0 - 0.1$, $30kT_0 - 0.1$, $100kT_0 - 0.1$, and $300kT_0 - 0.1$. The ratios in my simulations are in good agreement with the theoretical curves. The maximum difference is a factor of two at $x = 300$. Since the amount of the energy released by the binaries, and potential in the core are not accurate so much in this argument, the difference is negligible.

The ratio in model $1kT_0 - 0.1$, and $3kT_0 - 0.1$ is much larger than the theoretical curve of $f_{\text{b,c}} = 0.04$. This is because the core collapse of the cluster stop due to the energy that goes to the cluster from the three-body binaries composed of the single mass stars. The three-body binaries appear after the deep core collapse as discussed in section 3.1.

As is seen in figure 3.14, the theoretically estimated ratio, r_c/r_h , becomes smaller and smaller with the binding energy of the primordial binaries, E_{bin} . This is not in agreement with the minimum ratio of the core radius to the half-mass radius in model Double, $r_c/r_h = 0.005$, if I consider model Double as the hard limitation.

In model Double, three-body binaries composed of the double mass stars are formed at the halt of core collapse as discussed in section 3.1. The thick curve in model Double in figure 3.3 shows that the three-body binaries release energy. The deep core collapse stops due to the energy from the three-body binaries to the cluster.

If I consider model Double as the hard limitation again, the three-body binaries composed of the double mass stars correspond to quadruples in which the primordial binaries revolve around each other, and which are formed through the encounters of the three primordial binaries. In the case of more than a critical binding energy, these quadruples should be formed, and release the energy through the shrink of the orbits between the primordial binaries, which are the components of these quadruples. Eventually, the core collapse stops.

I estimate the critical binding energy. The critical binding energy is that of the point at which the theoretical curve of $f_{\text{b,c}} = 1.0$ and the dashed line in the lower right of figure 3.14, $r_c/r_h = 0.005$, cross. I adopt the theoretical curve of $f_{\text{b,c}} = 1.0$, since the mass fraction of the binaries in the core at the halt of core collapse becomes larger with increasing the binding energy of the binaries, and the mass fraction in model $300kT_0 - 0.1$ is 0.8, as seen in figure 3.7. I adopt $r_c/r_h = 0.005$ for the ratio in which the quadruples are formed, since the three-body binaries are formed at $r_c/r_h = 0.005$ in model Double. The critical value is $E_{\text{bin}} \sim 1000kT_0$. However, the critical value may be more than that value. In hard limit, theoretical curves underestimates r_c/r_h , neglecting the depth of the potential in the core when deep core collapse occurs.

3.4.3 After halt of core contraction

In models $10kT_0 - 0.1$, $30kT_0 - 0.1$, and $100kT_0 - 0.1$, I follow the evolution after the halt of the core contractions during at least 1000 time unit. During

this time, the ratio of the core radii to the half-mass radii grow smaller: the core radii slightly grow smaller (models $10kT_0 - 0.1$ and $30kT_0 - 0.1$) and larger (model $100kT_0 - 0.1$), and the half-mass radii grow larger. Considering the time evolutions of the distributions of the binding energies and mass fractions of the binaries, and the average kinetic energies of the single stars and binaries, I compare the core sizes in the simulation results with the theoretical formula: equation (3.7).

I estimate the average kinetic energy of the single stars and binaries as

$$1kT = 1kT_0 \left(\frac{r_{h,0}}{r_h} \right), \quad (3.25)$$

where $r_{h,0}$ is the half-mass radius at the initial time, and $r_{h,0} = 0.77$ in Plummer's model. Equation (3.25) is derived from virial theorem $1kT \propto r_h^{-1}$. Then, the average kinetic energies of the single stars and binaries at the time when the core contractions stop, and when the simulations are finished are $1kT = 0.80kT_0$ and $1kT = 0.52kT_0$ in $10kT_0 - 0.1$, $1kT = 0.87kT_0$ and $1kT = 0.53kT_0$ in $30kT_0 - 0.1$, and $1kT = 0.76kT_0$ and $1kT = 0.59kT_0$ in $100kT_0 - 0.1$.

Figure 3.15 shows the distributions of the binding energies of the binaries scaled by the total number of binaries within the whole clusters (left panels), the half-mass radii (middle panels), and twice the core radii (right panels) in models $10kT_0 - 0.1$ (top panels) at the time when the simulations are finished. $30kT_0 - 0.1$ (middle panels), and $100kT_0 - 0.1$ (bottom panels). From figure 3.15, we can see that the binaries with the initial binding energies do not exist within twice the core radii in models $10kT_0 - 0.1$ and $30kT_0 - 0.1$ when the simulations are finished. Assuming that the distributions of the binding energies within the whole clusters, the half-mass radii, and twice the core radii are little different at the halt of the core contractions, the distributions are greatly changed in models $10kT_0 - 0.1$ and $30kT_0 - 0.1$ after the halts of the core contractions. The assumption is good approximation, since the binaries with the initial binding energies are dominant at the halt of the core contractions.

In figure 3.16, crosses show core radii at the time when the core contraction stops, and when the simulations are finished, derived from the theoretical formula, and dashed curves show the time evolution of the core radii. For the core radii at the time when the core contraction stops, I use the distributions of the binding energies of the binaries within the whole cluster (figure 3.5). For the core radii at the time when the simulations are finished, I use the distributions of the binding energies of the binaries within the whole cluster, the half-mass radii, and twice the core radii from upper dots to bottom dots (figure 3.15). For the dimensionless coefficient S related to the cross section of binary-binary encounters, I use $S = 25.2$ if the binaries are in the same bin in figure 3.13 and 3.15, and $S = 15.9$ if the binaries are in different bins in figure 3.13 and 3.15.

From figure 3.16, the changes of the core radii in the simulation results after the halt of the core contractions are in good agreement with those in the theoretical estimates in models $10kT_0 - 0.1$, $30kT_0 - 0.1$, and $100kT_0 - 0.1$, particularly when I adopt the distributions of the binding energies within

twice the core radii. In models $10kT_0 - 0.1$ and $30kT_0 - 0.1$, the core radii slightly decrease after the halt of the core contraction both in the simulation and theoretical estimates. In model $100kT_0 - 0.1$, the core radius is not changed after the halt of the core contraction both in the simulation and theoretical estimates. In model $100kT_0 - 0.1$, the core radius seems to increase after $t = 2800$. However, the increase of the core radius may be fluctuation.

3.5 The initial mass fraction of the primordial binaries

In this section, I discuss the dependence of the core evolution on the initial mass fraction of the primordial binaries, $f_{b,0}$. I first show the time evolution of the core, r_c , and half-mass radii, r_h , and the mass fraction of the binaries inside the core radii and half-mass radii, f_b . I compare the ratio of the core radii to the half-mass radii in my simulation results with the theoretical estimate of the ratio with the respect of the mass fraction of the binaries in the core.

Figure 3.17 shows the time evolution of the core, r_c , and half-mass radii, r_h , of the clusters with $f_{b,0} = 0.03, 0.1, \text{ and } 0.3$ primordial binaries, each of which has the binding energy $E_{\text{bin},0} = 3kT_0, 10kT_0, \text{ and } 300kT_0$. In models $3kT_0 - 0.03$, and $3kT_0 - 0.1$, deep core collapse occurs, and in model $3kT_0 - 0.3$, core collapse stops halfway. In the $E_{\text{bin},0} = 30kT_0$, core collapse stops halfway. In the $E_{\text{bin},0} = 300kT_0$ models, deep core collapse occurs.

Figure 3.18 shows the time evolution of the mass fraction of the binaries inside the core and half-mass radii, f_b , of the clusters in the $f_{b,0} = 0.03, 0.1, \text{ and } 0.3$ models, each of which has the binding energy $E_{\text{bin},0} = 3kT_0, 10kT_0, \text{ and } 300kT_0$. In all of them, mass segregation occurs initially. However, the mass fraction of the binaries in the core decrease halfway in models $3kT_0 - 0.03, 3kT_0 - 0.1, 30kT_0 - 0.03, \text{ and } 300kT_0 - 0.03$. In models $30kT_0 - 0.03, \text{ and } 300kT_0 - 0.03$, the turning points correspond to the time when core collapse stops. In contrast, in models $3kT_0 - 0.03, \text{ and } 3kT_0 - 0.1$, the mass fractions of the binaries in the core decrease long before the core collapse.

In contrast to models $3kT_0 - 0.03, \text{ and } 3kT_0 - 0.1$, the core collapse of the cluster in model $3kT_0 - 0.3$ stops halfway. Since the cluster has many primordial binaries, the energy from the primordial binaries to the cluster is large enough to stop the core collapse.

I compare the ratio of the core radii to the half-mass radii in my simulation results with the theoretically estimated ratio in equation (3.7). The dots in figure 3.19 show the mass fraction of the binaries in the core at the halt of core collapse, $f_{b,c}$, of the clusters whose primordial binaries have binding energy, E_{bin} , at the initial time. The numbers beside the dots show the ratio of the core radii to the half-mass radii at the halt of core collapse. When gravothermal oscillations occur, the geometric means are shown. The triangles, circles, and squares show the models $f_{b,0} = 0.03, 0.1, \text{ and } 0.3$, respectively.

The curves in figure 3.19 show the ratio of the core radii to the half-mass

radii, r_c/r_h , of clusters whose primordial binaries have binding energy, E_{bin} , and whose mass fraction of the binaries in the core is $f_{b,c}$ at the halt of the core collapse. The numbers in italic format beside the curves indicate the values of r_c/r_h . If $E_{\text{bin}} \leq 2.5kT_0$, the curves are not reliable. This is the same reason as in figure 3.14.

In the clusters above the curve of $r_c/r_h = 0.002$, the core collapse stops halfway, and in the clusters below the curve of $r_c/r_h = 0.002$, the clusters experience deep core collapse. In the models $E_{\text{bin},0} = 3kT_0$, model $3kT_0 - 0.03$ and $3kT_0 - 0.1$ is below the curve, and model $3kT_0 - 0.3$ is above the curve. This is in good agreement with my simulation results. The ratios r_c/r_h in models $1kT_0 - 0.1$, $3kT_0 - 0.03$, and $3kT_0 - 0.1$ disagree with theoretical curves, since the core collapse stops due to energy heating core generated by the three-body binaries. In the models $E_{\text{bin},0} = 30kT_0$, the difference of r_c/r_h at the halts of core collapse between models $30kT_0 - 0.03$ and $30kT_0 - 0.1$ is larger than that between models $30kT_0 - 0.1$ and $30kT_0 - 0.3$. The dependence is reproduced by the theoretical curves in figure 3.19. Furthermore, r_c/r_h is nearly the same among the $E_{\text{bin},0} = 300kT_0$ models in my simulations. This is also reproduced by the theoretical curves. In the other models, the theoretical curves agree with my simulation results.

3.6 Comparison with previous studies

McMillan et al. (1990) and Heggie and Aarseth (1992) showed only large core radii at the halt of core contraction in clusters with primordial binaries whose binding energies have wide distribution. In clusters with primordial binaries whose binding energies have the distribution of δ function, I found that core radii at the halt of core contraction depend on hardness of primordial binaries in clusters: the core radii are small in soft and super hard ranges, and large in intermediate hard range. The difference of the core radii results from that of heating rate of each hardness of primordial binary. To show the difference of the heating rate is owing to setting of distribution functions of binding energy of the primordial binaries as δ functions.

My results suggest that the large core radii in McMillan et al. (1990) and Heggie and Aarseth (1992) is only due to heating of $10 - 100kT_0$ primordial binaries in their clusters which include primordial binaries from several kT_0 to several hundreds kT_0 in my units. From the time evolution of the core radius in the model $f_{b,0} = 0.03$ and $E_{b,0} = 30kT_0$ (the fourth left panel in figure 3.17), we see that core contraction stop halfway in clusters with small population of primordial binaries with intermediate hardness.

3.7 High-velocity escapers

I investigate escapers of each cluster in the $f_{b,0} = 0.1$ models. Figure 3.20 and 3.21 show the number distributions of the velocities of single escapers ($N_{\text{esc},\text{sin}}$),

and binary escapers ($N_{\text{esc,bin}}$) in the models $f_{\text{b},0} = 0.1$. Both sizes of velocity bin are 0.1 in $\log_{10} v_{\text{sin}}$ and $\log_{10} v_{\text{bin}}$. Note that in model Double, the single and binary escapers correspond to the escapers of the single and double mass stars, respectively. Except model Double, two peaks are present, although the higher peaks are small in models No-binary, $1kT_0 - 0.1$, and $3kT_0 - 0.1$. The population of the lower velocity escapers is driven by two-body relaxation, and that of the higher velocity escapers is ejected from the clusters through binary-single and binary-binary encounters. In the binary escapers, the escape velocities are similar to the higher population of the single escapers. They are also ejected from the clusters through binary-single and binary-binary encounters.

Figure 3.22 shows the velocity of single escapers in the top and , top 99, 90, and 50 % from top to bottom in as a function of the initial binding energy of the primordial binaries in the models $f_{\text{b},0} = 0.1$. Figure 3.23 shows those of the binary escapers, although top 99 % is omitted because of the small number of the binary escapers. The dashed lines in both figures show circular velocity of the binary as a function of the initial binding energy, E_{bin} .

The gradients of single escapers in the top, and top 99, and 90 % of all single escapers, and binary escapers in the top 90, and 50 % of all binary escapers are nearly the same as the gradient of the internal velocity of the binaries between models $100kT_0 - 0.1$ and $300kT_0 - 0.1$. This shows that almost binaries eject single stars and themselves from the clusters at the first encounters.

Consider a globular cluster whose virial radius is 10 pc, and whose mass is 10^6 solar mass. Then, one velocity unit is 24 km/s. When I apply my simulation results for the cluster, the highest velocity of the escapers is 500 km/s, which is the single escaper in model $300kT_0 - 0.1$.

Figure 3.24 shows the number distribution, $N_{\text{esc,bin}}$ of the binding energy of binary escapers in the $f_{\text{b},0}$ models. The size of energy bin is 0.1 in $\log_{10} E_{\text{bin}}$. In models $1kT_0 - 0.1$, $3kT_0 - 0.1$, $10kT_0 - 0.1$, $30kT_0 - 0.1$, and $100kT_0 - 0.1$, the binding energy distribution is largely changed from the initial conditions. On the other hand, in models $300kT_0 - 0.1$, the peak is at the initial binding energy. This shows that these primordial binaries are ejected from the clusters as soon as they encounter with single stars and other binaries. Figure 3.25 shows the binding energy of the binary escapers in the top, and top 90, and 50 % from top to bottom as a function of the initial binding energies in the $f_{\text{b},0} = 0.1$ clusters.

Additionally, I list the triple escapers in table 3.3. The second column is the velocity of the center of mass of the triple escapers, v_{tri} . The third and fourth columns are, respectively, the binding energy ($E_{\text{bin,in}}$ and $E_{\text{bin,out}}$) of the inner and outer binaries in unit of kT_0 .

Table 3.1: Initial models.

| Model name | $E_{\text{bin},0}$ | $f_{\text{b},0}$ | $N_{\text{b},0}$ | $f_{\text{d},0}$ | $N_{\text{d},0}$ |
|------------------|--------------------|------------------|------------------|------------------|------------------|
| $1kT_0 - 0.1$ | $1kT_0$ | 0.1 | 819 | 0 | 0 |
| $3kT_0 - 0.1$ | $3kT_0$ | 0.1 | 819 | 0 | 0 |
| $10kT_0 - 0.1$ | $10kT_0$ | 0.1 | 819 | 0 | 0 |
| $30kT_0 - 0.1$ | $30kT_0$ | 0.1 | 819 | 0 | 0 |
| $100kT_0 - 0.1$ | $100kT_0$ | 0.1 | 819 | 0 | 0 |
| $300kT_0 - 0.1$ | $300kT_0$ | 0.1 | 819 | 0 | 0 |
| $3kT_0 - 0.03$ | $3kT_0$ | 0.03 | 246 | 0 | 0 |
| $30kT_0 - 0.03$ | $30kT_0$ | 0.03 | 246 | 0 | 0 |
| $300kT_0 - 0.03$ | $300kT_0$ | 0.03 | 246 | 0 | 0 |
| $3kT_0 - 0.3$ | $3kT_0$ | 0.3 | 2458 | 0 | 0 |
| $30kT_0 - 0.3$ | $30kT_0$ | 0.3 | 2458 | 0 | 0 |
| No-binary | – | 0 | 0 | 0 | 0 |
| Double | – | 0 | 0 | 0.1 | 819 |

Table 3.2: Accuracy, and apocentric and pericentric parameters.

| Model name | η | η_s | α | β |
|------------------|--------|----------|----------|---------|
| $1kT_0 - 0.1$ | 0.01 | 0.0025 | 5 | 10 |
| $3kT_0 - 0.1$ | 0.01 | 0.0025 | 5 | 10 |
| $10kT_0 - 0.1$ | 0.01 | 0.0025 | 5 | 10 |
| $30kT_0 - 0.1$ | 0.01 | 0.0025 | 5 | 10 |
| $100kT_0 - 0.1$ | 0.01 | 0.0025 | 5 | 50 |
| $300kT_0 - 0.1$ | 0.01 | 0.0025 | 8 | 50 |
| $3kT_0 - 0.03$ | 0.01 | 0.0025 | 5 | 10 |
| $30kT_0 - 0.03$ | 0.01 | 0.0025 | 5 | 10 |
| $300kT_0 - 0.03$ | 0.01 | 0.0025 | 5 | 50 |
| $3kT_0 - 0.3$ | 0.01 | 0.0025 | 5 | 10 |
| $30kT_0 - 0.3$ | 0.01 | 0.0025 | 5 | 50 |
| No-binary | 0.01 | 0.0025 | 5 | 10 |
| Double | 0.01 | 0.0025 | 5 | 10 |

Table 3.3: The list of triple escapers.

| Model name | v_{tri} [standard units] | $E_{\text{bin,in}}$ [kT_0] | $E_{\text{bin,out}}$ [kT_0] |
|-----------------|-----------------------------------|--------------------------------|---------------------------------|
| $30kT_0 - 0.1$ | 4.7 | 8.5×10^2 | 3.0×10^1 |
| $100kT_0 - 0.1$ | 0.44 | 2.8×10^2 | 9.2×10^0 |
| | 1.2 | 5.7×10^2 | 7.4×10^0 |
| | 0.39 | 4.7×10^2 | 2.6×10^0 |
| | 1.7 | 6.2×10^2 | 1.5×10^0 |
| $300kT_0 - 0.1$ | 2.0 | 9.4×10^2 | 3.7×10^1 |

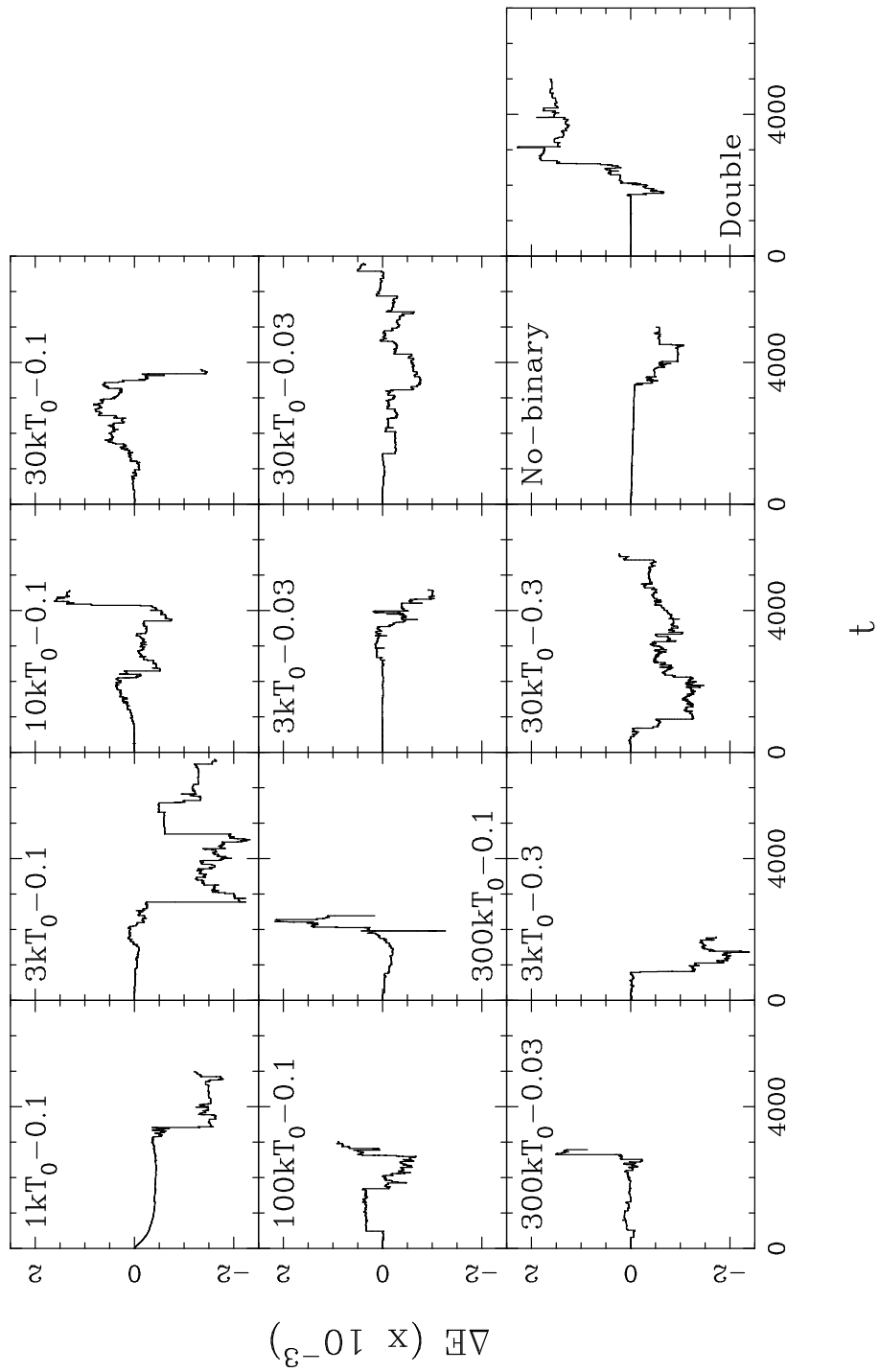


Figure 3.1: Time evolution of energy errors in cluster models in table 3.1.

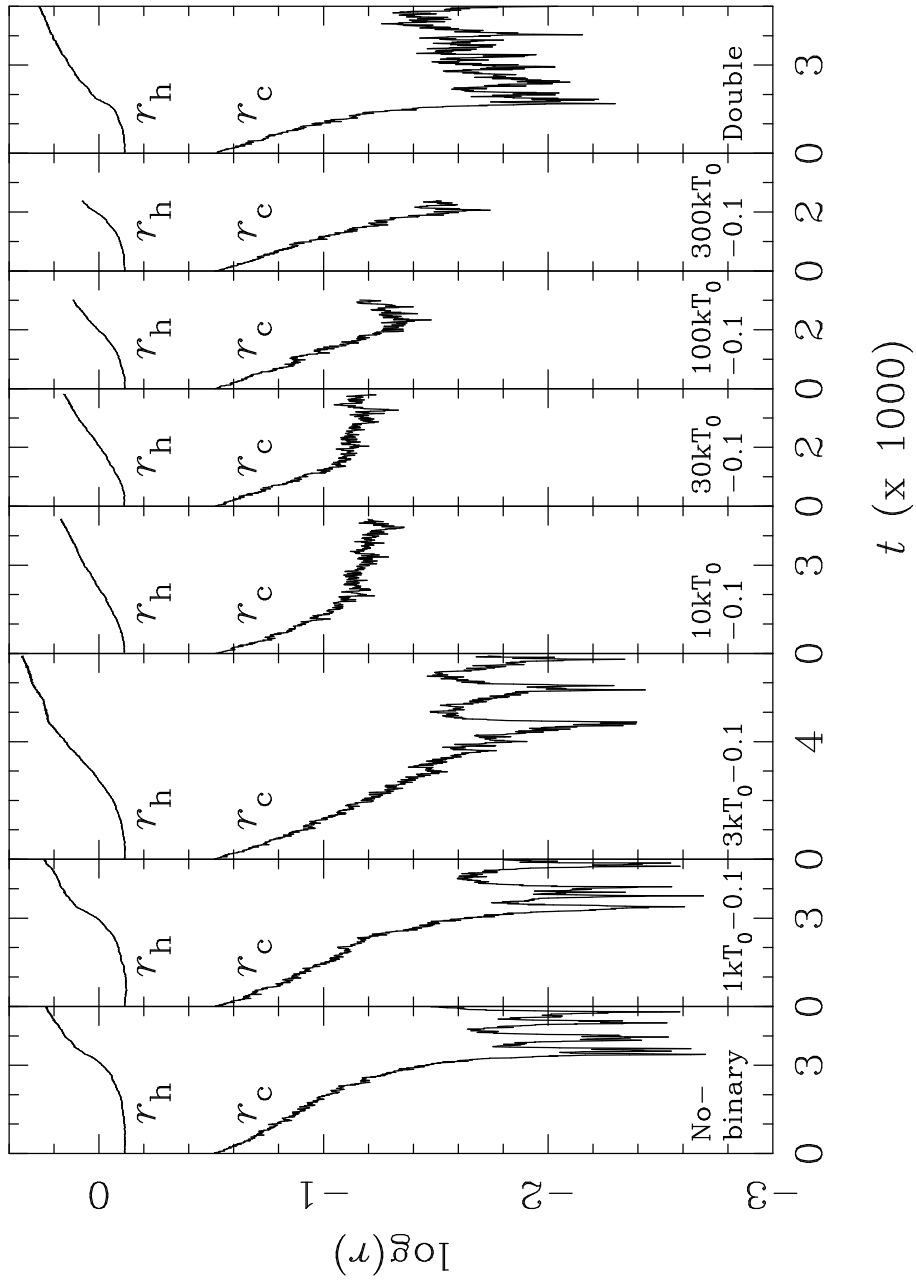


Figure 3.2: Time evolution of the core radii, r_c , and half-mass radii, r_h , of the clusters with $f_{b,0} = 0.1$ primordial binaries, and models No-binary and Double.

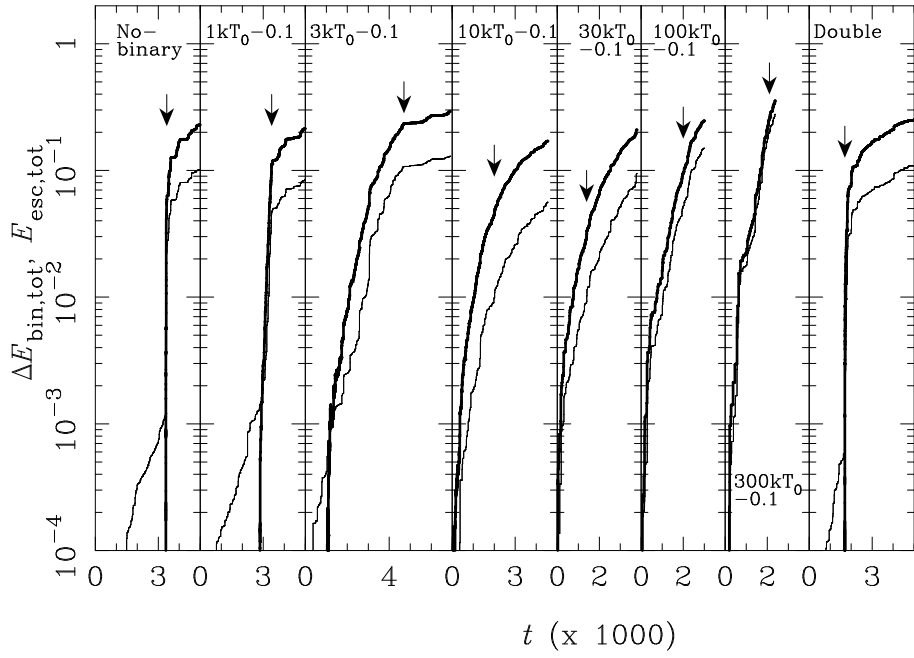


Figure 3.3: The time evolution of the increase of the total binding energy of the binaries, $\Delta E_{\text{bin,tot}}(t)$ (thick curves), which corresponds to energy generated by the binaries, and the total energy of escapers, $E_{\text{esc,tot}}(t)$, from the clusters (thin curves), which corresponds to energy not heating the clusters despite that it is generated by the binaries. The arrows indicate the times when the core collapse stops.

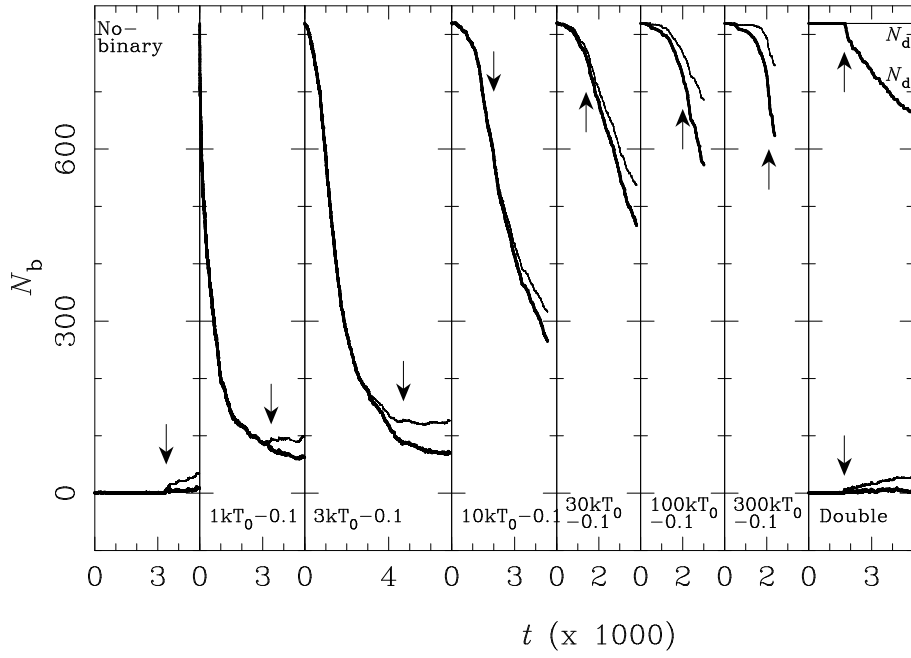


Figure 3.4: Time evolution of the number of binaries, N_b , in the $f_{b,0} = 0.1$ models, and models No-binary and Double. For model Double, the number of the double mass stars is also plotted. The thick curves indicate the numbers of binaries (or double mass stars) within the clusters, and the thin curves indicate the total numbers of binaries, (or double mass stars) including escapers. The arrows indicate the times when the core collapse stops.

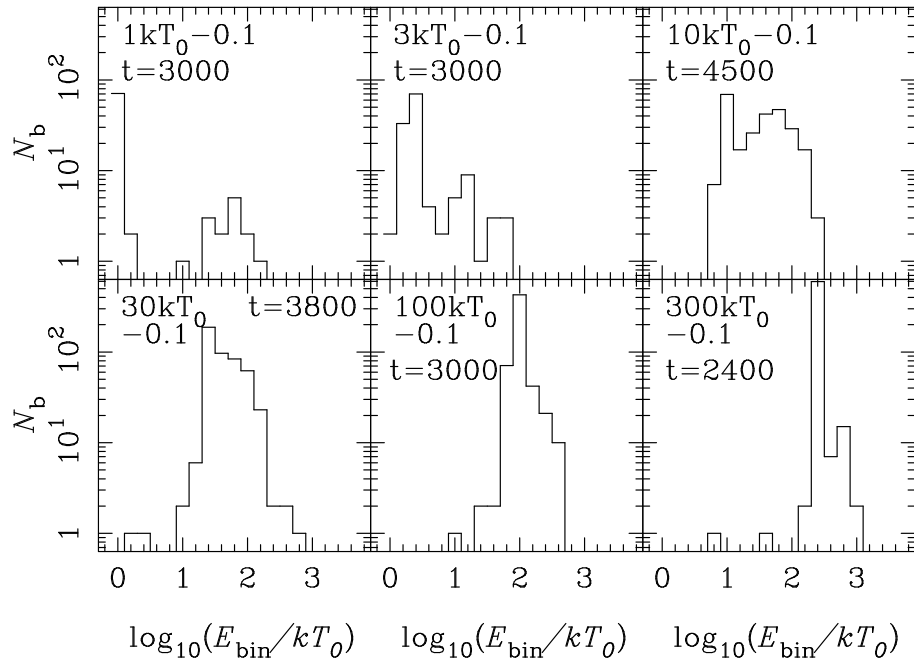


Figure 3.5: The number distribution, N_b , of the binding energy of the binaries, E_{bin} , in unit of kT_0 .

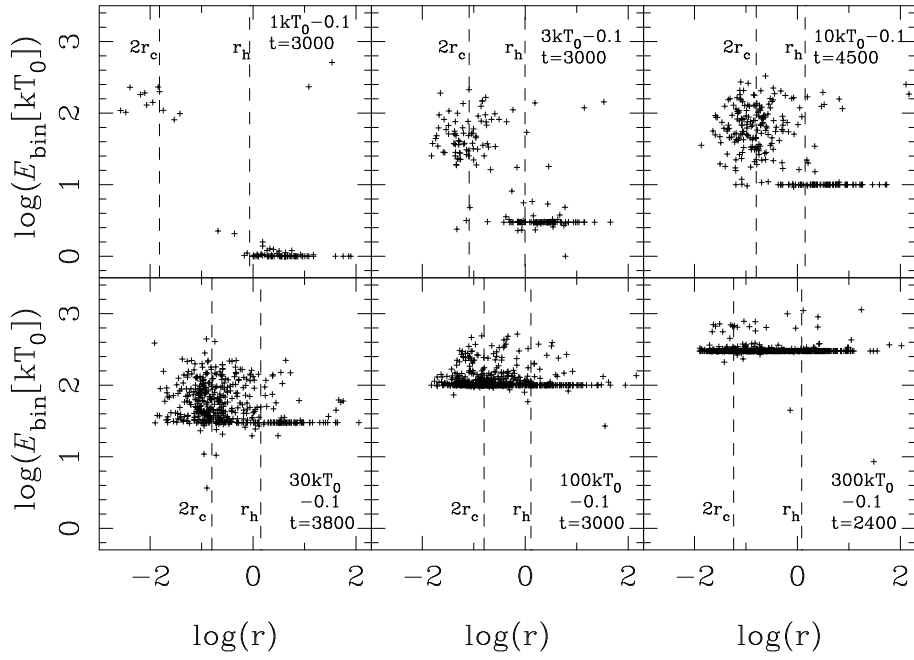


Figure 3.6: Binding energy and distance from cluster center of each binary at the time indicated in the panels. The dashed lines show the half-mass radii and twice the core radii at the time.

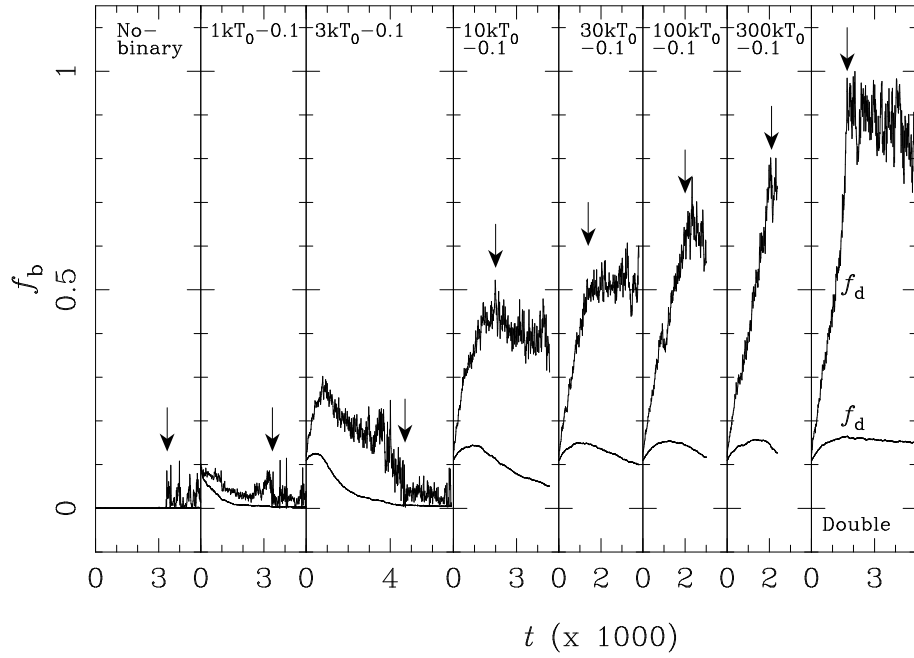


Figure 3.7: Time evolution of the mass fraction, f_b , of the binaries inside the core radii (the upper curves) and half-mass radii (the lower curves) in the $f_{b,0}$ models, and model No-binary. For model Double, figure 3.7 shows the mass fraction, f_d , of the double mass stars are shown. The arrows show the time when the core collapse stops.

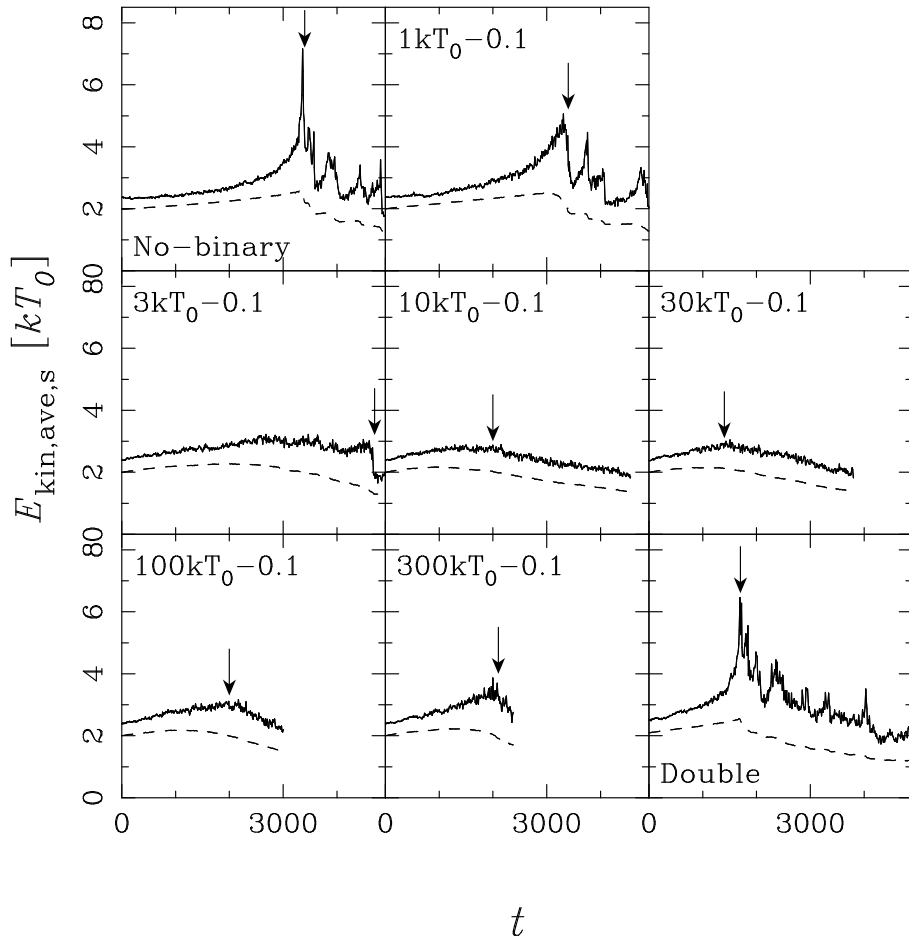


Figure 3.8: Time evolution of the mean kinetic energy of the single stars inside the core radii (solid curves), and the half-mass radii (dashed curves) in the $f_{b,0} = 0.1$ models, and models No-binary and Double. The arrows show the time when the core collapse stops.

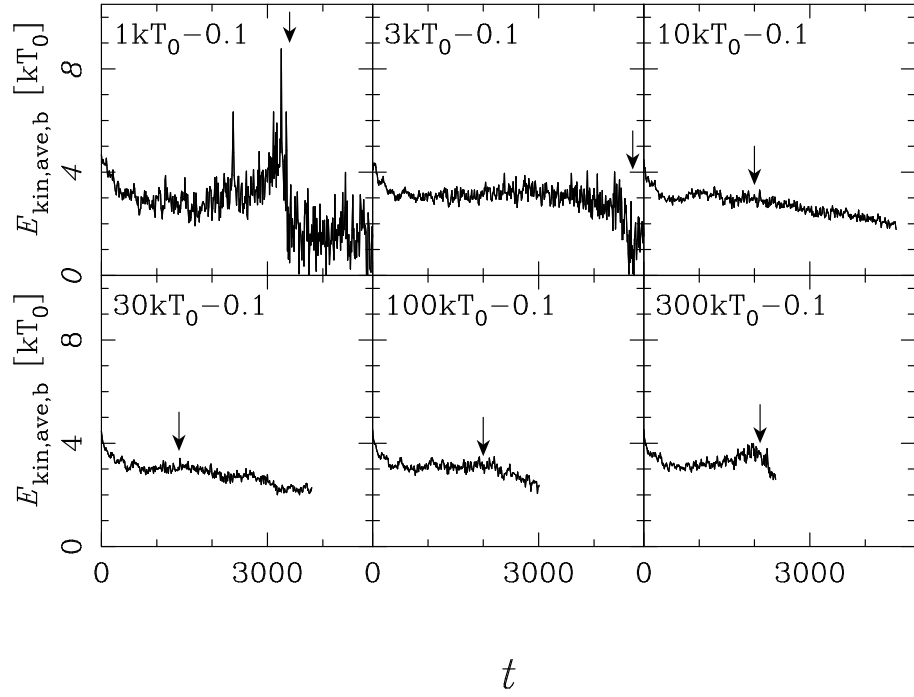


Figure 3.9: Time evolution of the mean kinetic energy of the binaries, $E_{\text{kin,ave,b}}$, inside the core radii in the $f_{\text{b},0} = 0.1$ models. The arrows show the time when the core collapse stops.

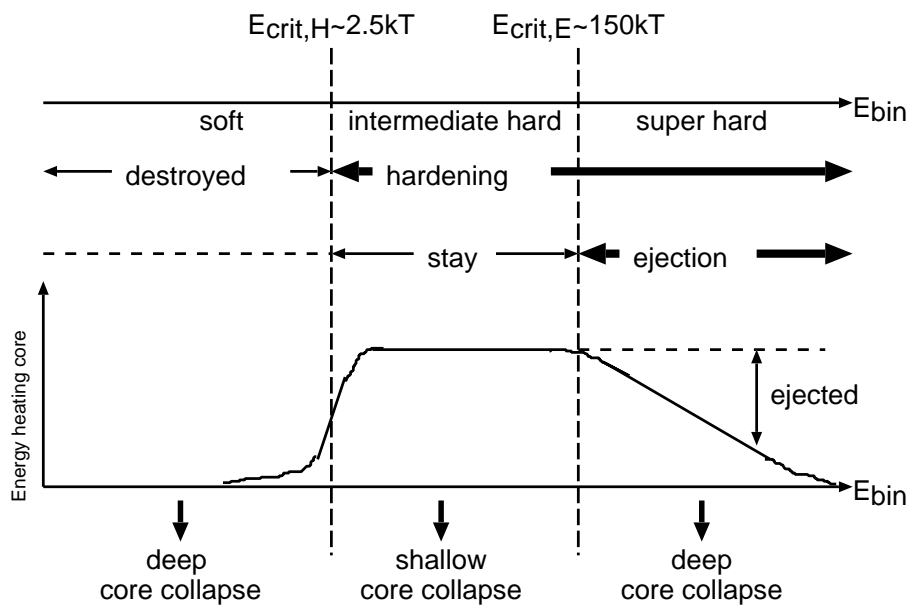


Figure 3.10: Interpretation of core evolution.

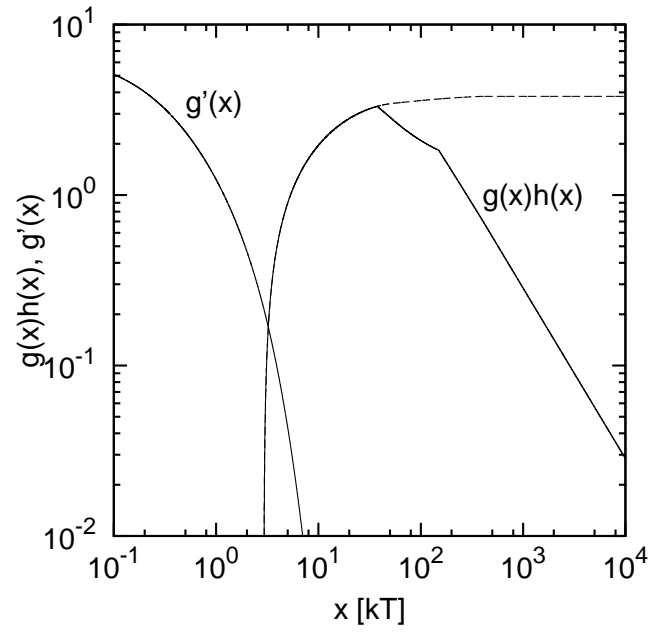


Figure 3.11: Dimensionless heating rate of binary-single encounters in which the binaries survives ($g(x)h(x)$) and are destroyed ($g'(x)$) as a function of x , where the binary have dimensionless binding energy x (solid curve). The dashed line shows the dimensionless hardening rates of the binary with the binding energy x in a sea of single stars, i.e. $g(x)$.

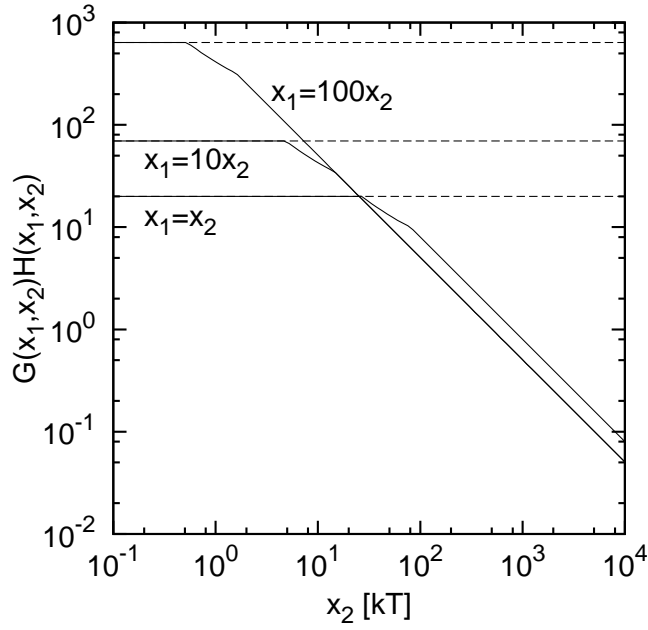


Figure 3.12: Dimensionless heating rate of binary-binary encounters, $G(x_1, x_2)H(x_1, x_2)$, as a function of x_2 , where the binaries have dimensionless binding energy x_1 and x_2 , and $x_1 = x_2$, $x_1 = 10x_2$, and $x_1 = 100x_1$ (solid curves). The dashed lines show the dimensionless hardening rates of the binary with the binding energy x_1 in a sea of binaries with the binding energy x_2 , i.e. $G(x_1, x_2)$.

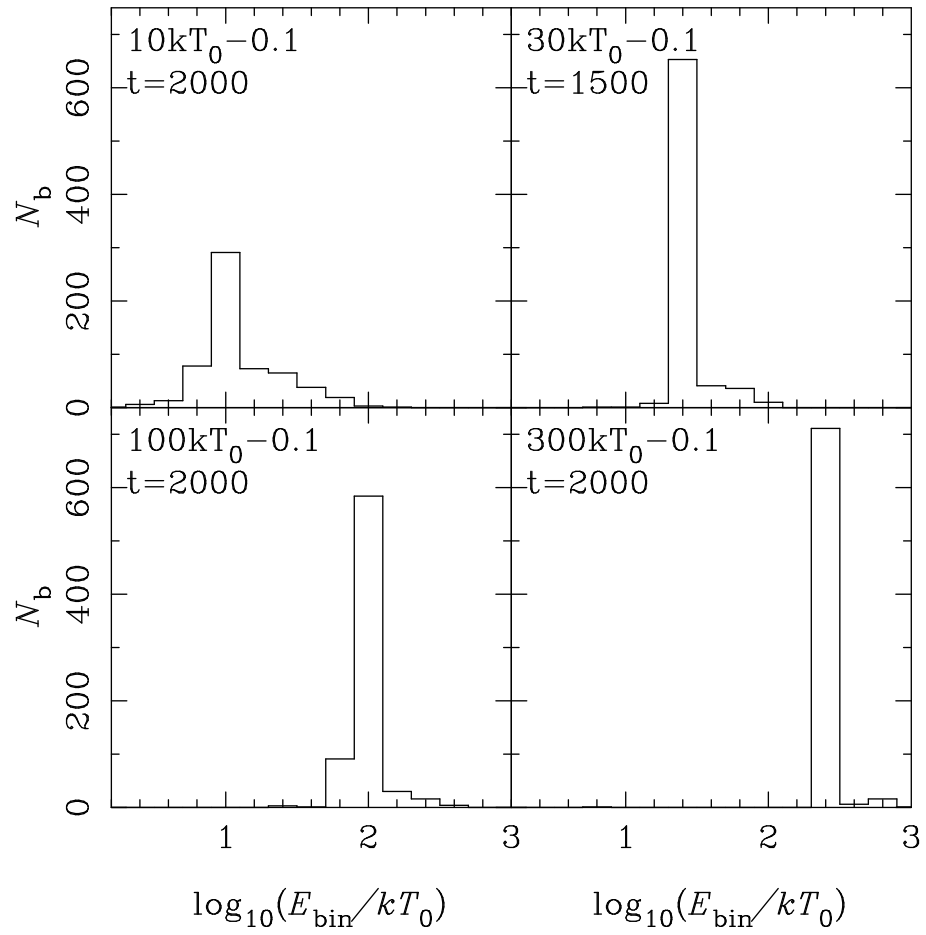


Figure 3.13: Distributions of the binding energies of binaries in the whole clusters at the time indicated in each panel, which is the time when the core contractions stop.

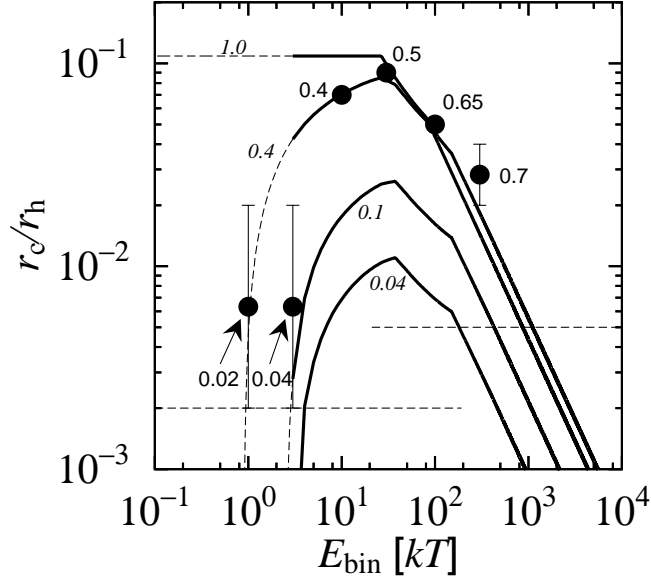


Figure 3.14: Ratio of core radii to half-mass radii at the halts of core collapse of the clusters whose primordial binaries have equal binding energy, E_{bin} , and whose cores contain the mass fraction of the primordial binaries in the core, $f_{\text{b},c}$. The dots show the ratio of the core radii to the half-mass radii at the halt of core collapse in my simulation. The numbers beside the dots are $f_{\text{b},c}$ at that time. The four curves draw equation (3.7) when $f_{\text{b},c} = 0.04, 0.1, 0.4,$ and 1.0 . The values of $f_{\text{b},c}$ are beside the curves in italic format. The dashed lines, $r_c/r_h = 0.002,$ and $0.005,$ show the ratio of core radii to half-mass radii at the halts of core collapse in model No-binary and Double, respectively.

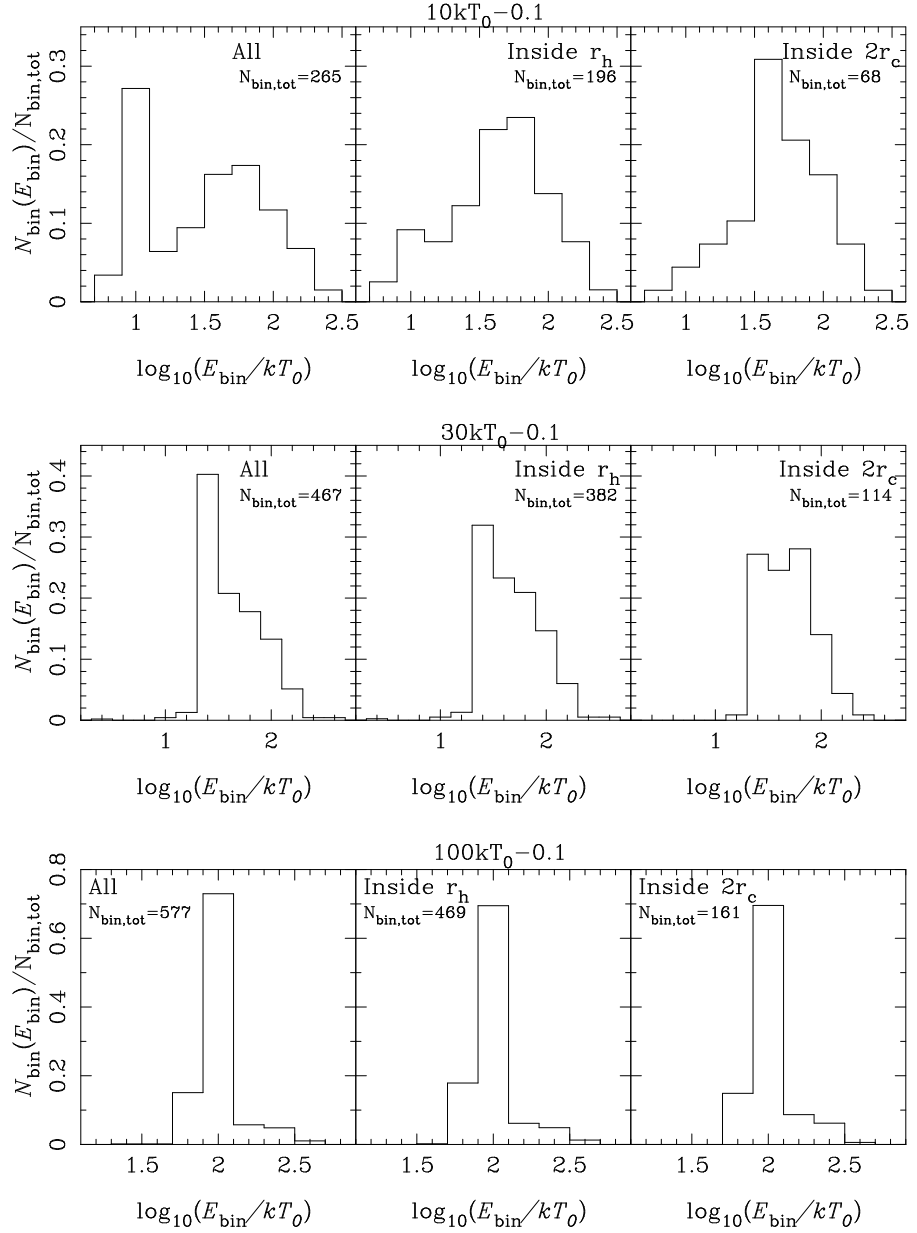


Figure 3.15: the distributions of the binding energies of the binaries scaled by the total number of binaries within the whole clusters (left panels), the half-mass radii (middle panels), and twice the core radii (right panels) in models $10kT_0 - 0.1$ (top panels) at the time when the simulations are finished. $30kT_0 - 0.1$ (middle panels), and $100kT_0 - 0.1$ (bottom panels). The total numbers of the binaries are indicated in these panels. The size of bins is 0.2 in $\log_{10} E_{\text{bin}}$, where the unit of E_{bin} is kT_0 .

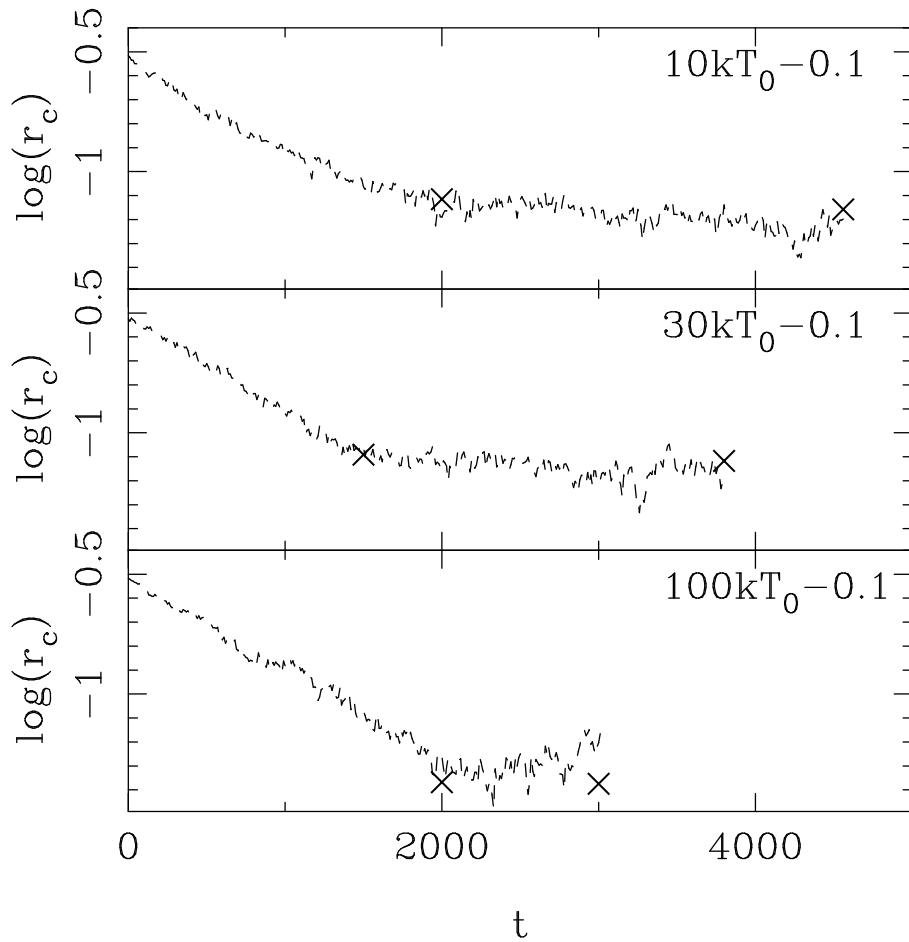


Figure 3.16: Time evolution of core radii in my simulation (dashed curves), and theoretical estimate (crosses). The time of theoretical estimate is the time when the core contraction stops, and the time when the simulations are finished. I use the distributions of the binding energies of binaries within the whole clusters, half-mass radii, and twice the core radii for the three core radii at the time when the simulations are finished, which are theoretically estimated, from top to bottom. I use the distributions of the binding energies of binaries within the whole clusters for the core radii at the time when the core contraction.

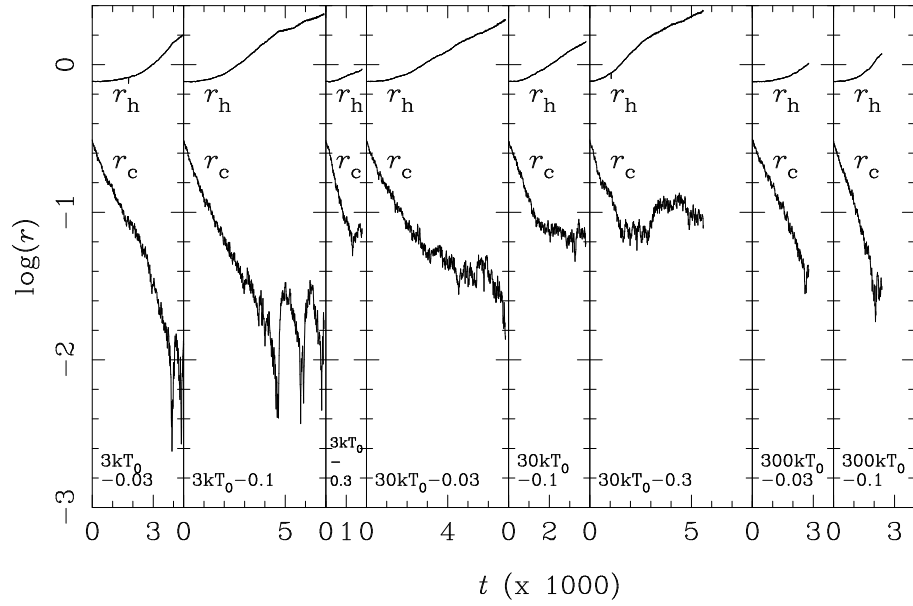


Figure 3.17: Time evolution of the core, r_c , and half-mass radii, r_h , of the clusters with $f_{b,0} = 0.03, 0.1$, and 0.3 primordial binaries, each of which has the binding energy $E_{\text{bin},0} = 3kT_0, 10kT_0$, and $300kT_0$. The way of calculation of the core radii is the same as that in figure 3.2.

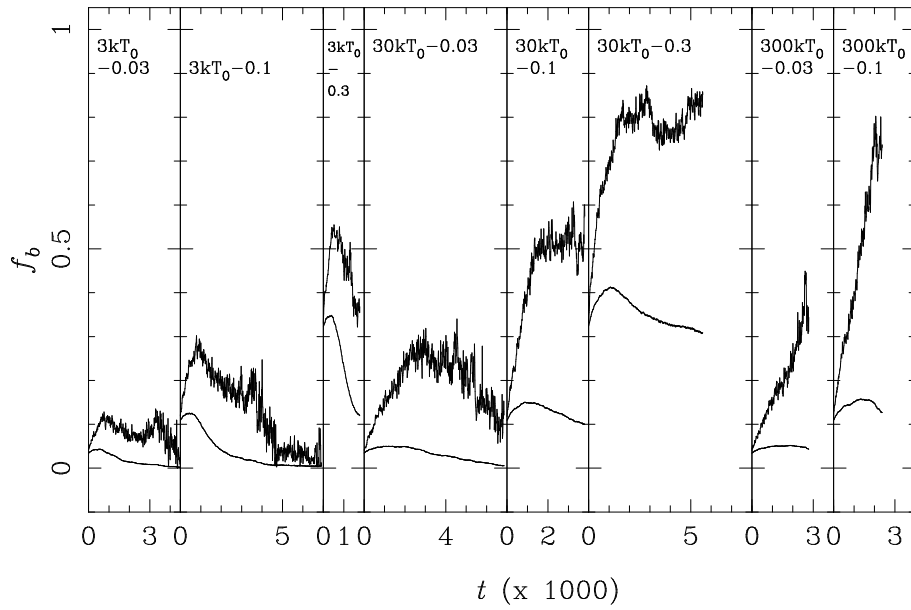


Figure 3.18: Time evolution of the mass fraction of the binaries inside the core and half-mass radii of the clusters, f_b , with $f_{b,0} = 0.03, 0.1$, and 0.3 primordial binaries, each of which has the binding energy $E_{\text{bin},0} = 3kT_0, 10kT_0$, and $300kT_0$.

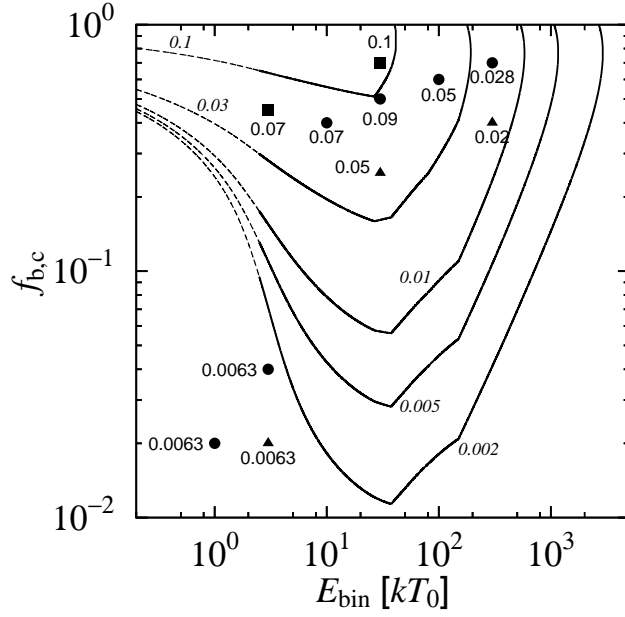


Figure 3.19: Contours of the ratio of core radii to half-mass radii at the halt of core contraction in clusters whose mass fraction of primordial binaries in the core is $f_{b,c}$, and distribution function of the primordial binaries is $\delta(x - E_{bin})$, which are obtained from equation (3.24). The numbers in italic show the ratio of the core radii to the half-mass radii. The dashed curves are possibly not correct, since the heating rate through binary-binary interactions in hard binaries is extended to the soft range. The dots show simulation results. The vertical axis shows $f_{b,c}$ at the halt of core contraction, the horizontal axis shows E_{bin} at the initial time, and the numbers beside the dots is the ratio of core radii to the half-mass radii at the halt of the core contraction. The shapes of the dots show the initial mass fraction of the primordial binaries in the clusters, $f_{b,0}$. The triangles, circles, and squares show the models $f_{b,0} = 0.03$, 0.1 , and 0.3 , respectively.

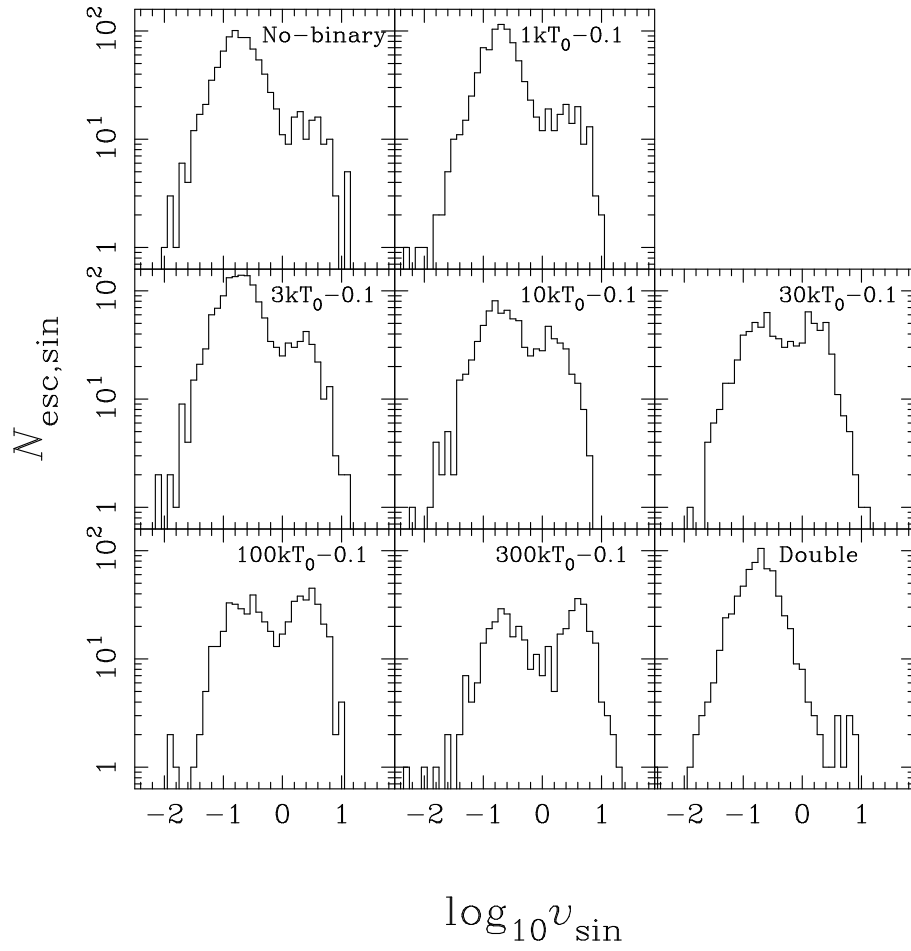


Figure 3.20: The number distribution of the velocities of single escapers in the models $f_{b,0} = 0.1$. The velocity is in N -body standard units. Bin sizes of the velocity is 0.1 in logarithmic scale.

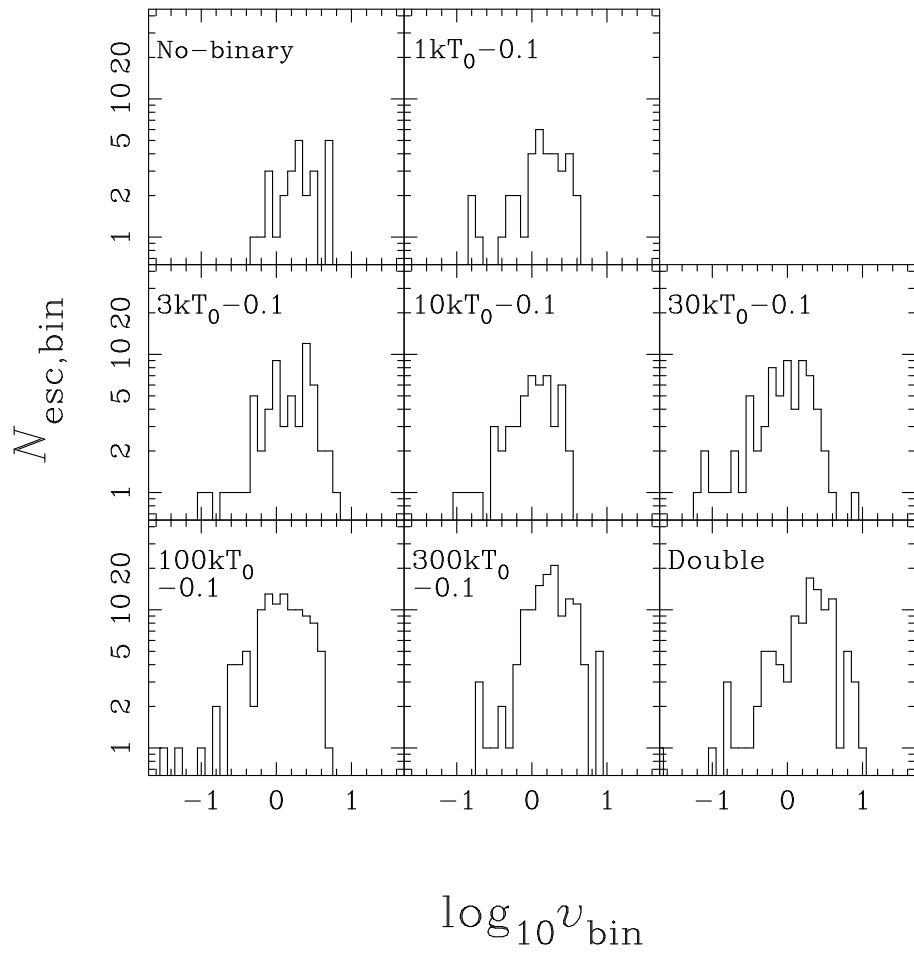


Figure 3.21: The number distribution of the velocities of binary escapers in the models $f_{b,0} = 0.1$. The velocity is in N -body standard units. Bin sizes of the velocity is 0.1 in logarithmic scale.

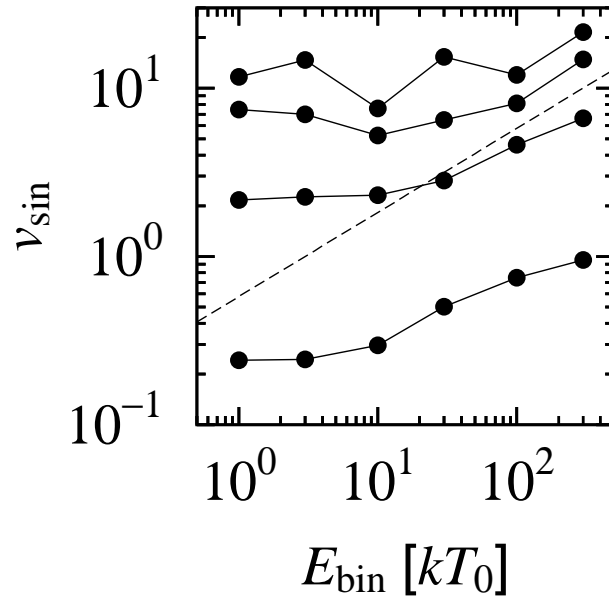


Figure 3.22: The velocity of single escapers in the top, and the top 1, 10, and 50 % of all from top to bottom as a function of initial binding energy of primordial binaries in the $f_{\text{b},0} = 0.1$ clusters. The dashed line shows circular velocity of a binary as a function of its binding energy.

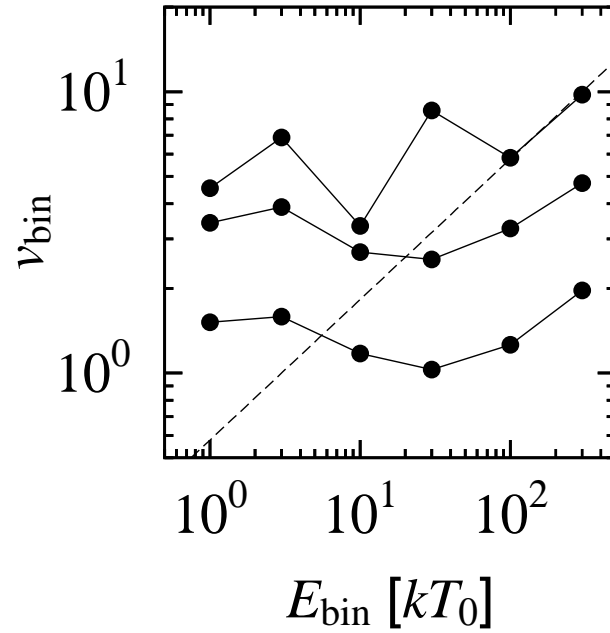


Figure 3.23: The velocity of binary escapers in the top, and the top 10, and 50 % of all from top to bottom as a function of initial binding energy of primordial binaries in the $f_{\text{b},0} = 0.1$ clusters. The dashed line shows circular velocity of a binary as a function of its binding energy.

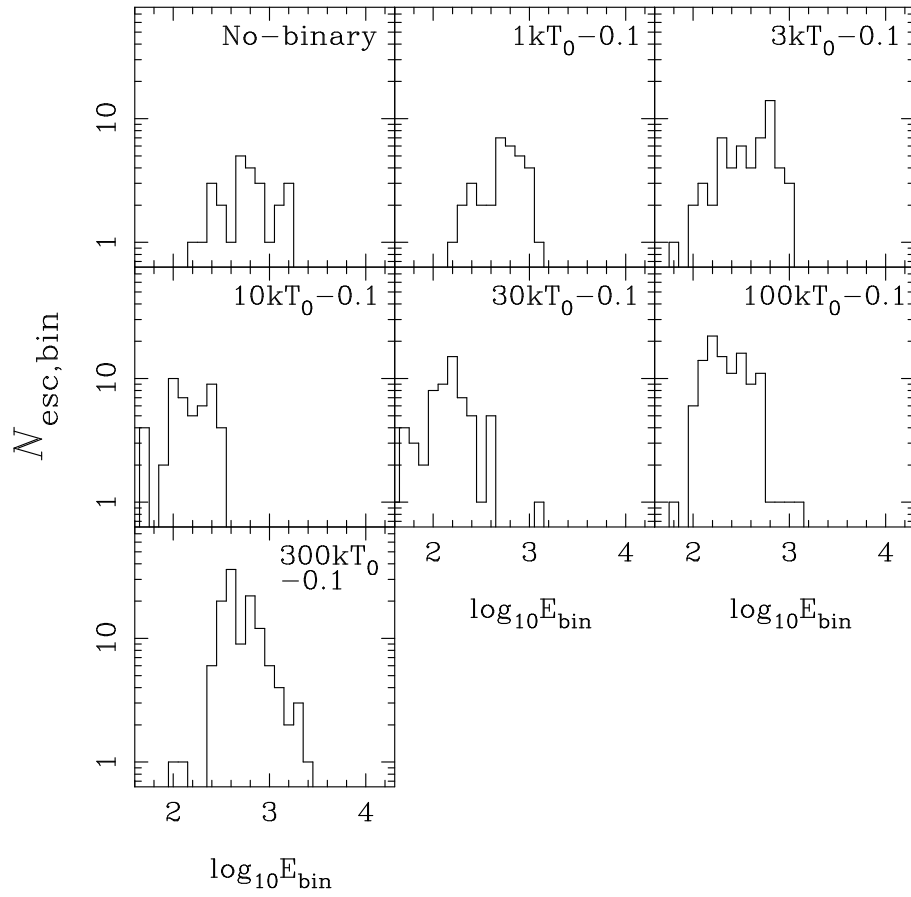


Figure 3.24: The number distribution of the binding energy of binary escapers in the models $f_{b,0} = 0.1$. The binding energy is in the unit of kT_0 . The bin size of the binding energy is 0.1 in logarithmic scale.

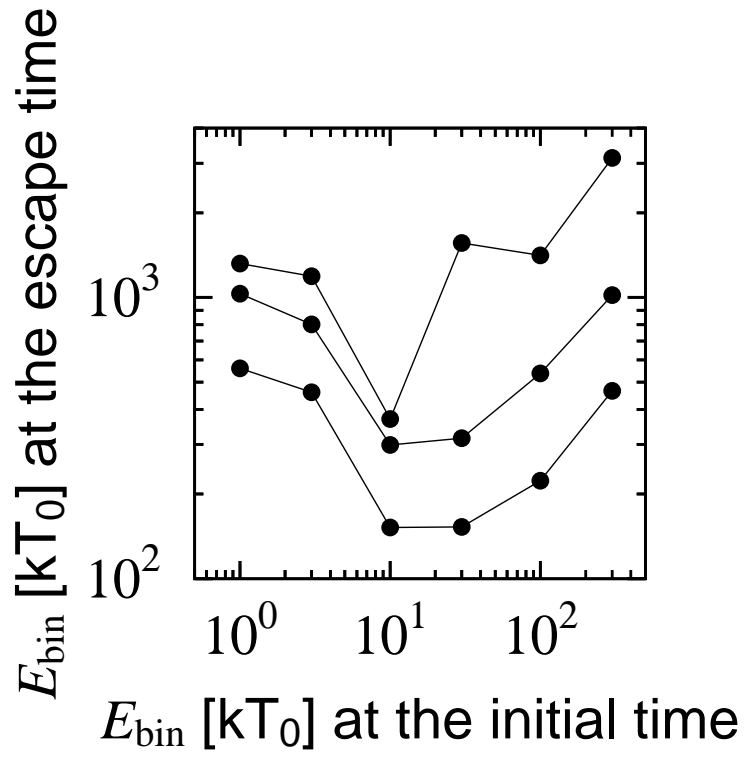


Figure 3.25: The binding energy of binary escapers in the top, and top 10, and 50 % of all from top to bottom as a function of initial binding energy of primordial binaries in the $f_{b,0} = 0.1$ clusters. The units of vertical and horizontal axes are kT_0 in logarithmic scale.

Chapter 4

Example of Application to Astrophysics: Estimate of Double Neutron Star Merger Rate

4.1 Evolution of neutron stars in globular clusters

Neutron stars are the most massive star in the globular clusters during last half the lives of the globular clusters ($\sim 5 \times 10^9$ years), since until first half their lives elapse, stars with more than $1.4M_{\odot}$ lose all or most of their initial masses due to their stellar evolutions. There are only neutron stars and binaries whose total masses are comparable to those of the neutron stars in the cluster cores due to mass segregation. The binaries in the core become DNSs after several encounters with single neutron stars. This is because more massive stars tend to be replaced with less massive stars composing the binaries through these encounters. The DNSs further encounter with single stars and other binaries, and grow harder and harder. Eventually, the DNSs are ejected from the clusters as high-velocity binary escapers through one encounter with a single star or another binary.

4.2 Previous works on DNS merger rate

Nowadays, we have to spend at least several years performing N -body simulation of the dynamical evolution of clusters with $N \sim 10^6$ during a Hubble time. We can not estimate the merger rate of DNSs which are formed in one globular cluster, directly from the results of the N -body simulations of the clusters. We need some modellings of formations of DNSs in globular clusters. In what

follows, I describe modellings which are constructed by previous works: Grindlay et al. (2006) and Ivanova et al. (2008).

Grindlay et al. (2006) estimated the number of DNSs formed in one globular cluster which undergoes core collapse once as

$$N_{\text{DNS}} = \int \Gamma_{\text{DNS}} dt, \quad (4.1)$$

where Γ_{DNS} is the formation rate of the DNSs. The formation rate of the DNSs, Γ_{DNS} , is expressed as

$$\Gamma_{\text{DNS}} = n_{\text{NS}} \sigma_{\text{DNS}} v_c N_{\text{pr}}, \quad (4.2)$$

where n_{NS} is the number density of neutron stars in the cluster core, σ_{DNS} is cross section of a binary with one neutron star and one less massive star for encounters that the less massive star is replaced with a single neutron star, v_c is velocity dispersion in the core, and N_{pr} is the number of binaries including one neutron star in the core. The Cross section, σ_{NS} , is derived from three-body scattering experiments in which a binary with one neutron star and one less massive star encounters with a single neutron star. From their experiments, $\sigma_{\text{DNS}} = 0.8 \text{AU}^2$, and from observations, they set $N_{\text{pr}} = 20$. Even if core collapse proceeds, the velocity dispersion in the core, v_c is not rarely changed. Therefore, they set $v_c = 10 \text{km/s}$.

Toward the core collapse of the cluster, the number density, n_{NS} , is dramatically changed. They set the evolution of the number density n_{NS} as

$$\int_0^{t_{\text{cc}}} n dt \sim \int_{t_{\text{cc}} - \tau_0}^{t_{\text{cc}}} n dt \sim 20 n_{\text{NS},0} \tau_0, \quad (4.3)$$

where t_{cc} is the time of the core collapse, τ_0 is the time remaining until core collapse, and $n_{\text{NS},0}$ is the number density of neutron stars at the time τ_0 . They set $n_{\text{NS},0} = 10^6 \text{pc}^{-3}$ and $\tau_0 \sim 100 \text{Myr}$, which means that almost stars in the core are neutron stars.

Ivanova et al.(2008) modelled clusters as those divided into two zones, core and halo, whose number densities are fixed. These clusters contain $\sim 10^6$ stars, all of which belong to binaries. They adopted Kroupa (2002) as initial mass function, and Belczynski et al. (2008) as stellar and binary evolution models. They set probability that a star with mass m is in the cluster core after a time t as

$$p(t) = \frac{1}{t_{\text{sc}}} \exp\left(-\frac{t}{t_{\text{sc}}}\right), \quad (4.4)$$

where t_{sc} is the characteristic mass segregation timescale, expressed as

$$t_{\text{sc}} \sim 10 C_{\text{sc}} \left(\frac{\langle m \rangle_{\text{h}}}{m}\right) t_{\text{rh}}. \quad (4.5)$$

Here, $\langle m \rangle_{\text{h}}$ is the average stellar mass in the cluster halo, and they set $C_{\text{sc}} \langle m \rangle_{\text{h}} = 3M_{\odot}$. Whether each star and binary encounter with other single stars and binaries is decided stochastically, obeying cross sections for single-single, binary-single, and binary-binary encounters which are proportional to the sum of the

stellar radii, the apocenter separation of the binary and the stellar radius, and the apocenter separations of the binaries, respectively. If a star or binary encounter with other objects, two-body, three-body, or four-body scattering experiments are performed. They investigated 70 cluster models among which the number density of stars in the core ranges from 10^3pc^{-3} to 10^6pc^{-3} , half-mass relaxation time ranges from 1Gyr to 3Gyr, and so on. In these 70 cluster models, only 14 DNSs are formed.

4.3 Our model for DNS evolution

In order to estimate the DNS merger rate from my simulation results, I have to decide which stars in my cluster models are neutron stars, considering theoretically the motions of the neutron stars in real globular clusters. This is because all the stars in my cluster models have equal mass, we can not distinguish which stars are neutron stars and other stars without any theoretical consideration.

I model that all the high-velocity single and binary escapers consist of neutron stars unless all the neutron stars in the clusters are completely depleted. This modelling is based on the assumption that all binaries hard enough to eject themselves and single stars through binary-single and binary-binary encounters consist of neutron stars, since hard binaries experience several encounters through which they are hardened.

Then, DNS merger rate per a globular cluster, N_{DNS} , is estimated results as follows:

$$N_{\text{DNS}} = \begin{cases} f_{\text{gw}} C_{\text{N}} n_{\text{hv,b}} T_{\text{sim}} & (C_{\text{N}}(n_{\text{hv,s}} + 2n_{\text{hv,b}})T_{\text{sim}} < N_{\text{NS}}) \\ f_{\text{gw}} N_{\text{NS}} \frac{n_{\text{hv,b}}}{n_{\text{hv,s}} + 2n_{\text{hv,b}}} & (C_{\text{N}}(n_{\text{hv,s}} + 2n_{\text{hv,b}})T_{\text{sim}} > N_{\text{NS}}) \end{cases}, \quad (4.6)$$

where $n_{\text{hv,s}}$ and $n_{\text{hv,b}}$ are, respectively, the number of high-velocity single and binary escapers per initial half-mass relaxation time in my cluster models, T_{sim} is the simulation time in the unit of initial half-mass relaxation time in my cluster models, f_{gw} is a fraction of DNSs merging within a Hubble time in the total DNSs, C_{N} is N -scaling factor which is required for scaling the number of stars in my cluster models to that in real globular clusters, and N_{NS} is the total number of neutron stars in real globular clusters. If neutron stars are completely depleted, the lower expression in the right-hand side of equation (4.6) is applied for N_{DNS} , and if not, the upper expression is done so.

Note that these high-velocity single escapers may include other than neutron stars. The binaries which are involved by binary-single and binary-binary encounters resulting in high-velocity single escapers may not be the DNSs. The binaries do not experience several encounters before the encounter resulting in the high-velocity single escapers, since single stars are ejected through softer binary interactions than the binaries themselves are ejected. I overestimate the depletion of neutron stars due to high-velocity single escapers. Therefore, I underestimate N_{DNS} when I adopt the lower expression in the right-hand side of equation (4.6).

I derive N -scaling factor C_N , which is expressed as

$$C_N = \frac{N_{\text{hv}}(N)}{N_{\text{hv}}(16384)} = \frac{N}{16384}, \quad (4.7)$$

where $N_{\text{hv}}(N)$ is the total number of high-velocity single and binary escapers at each half-mass relaxation time in a cluster with the number of stars, N . The reason for the second equality in equation (4.7) is as follows. The number of high-velocity escapers is proportional to the number of binary-single and binary-binary encounters. Energy generated from these binaries through such encounters is balanced with energy outflow from inside of half-mass radius to outside of half-mass radius, if the core contraction stops. The energy outflow does not depend on N . On the other hand, the energy generated through each encounter is inversely proportional to N . Therefore, the number of such encounters is proportional to N .

I express the number of neutron stars in the globular clusters N_{NS} as follows:

$$N_{\text{NS}} = 1000 \left(\frac{N}{10^6} \right), \quad (4.8)$$

which is consistent with observations of pulsars, and X-ray sources in massive globular clusters (e.g. 47 Tuc; Terzan 5). The retention factor of the neutron stars in the globular clusters is about 10 %, since $8 - 9^3$ neutron stars are formed in the globular cluster if we adopt Miller and Scalo (1979) or Kroupa (2001) whose upper limit of stellar mass is $15M_{\odot}$ and lower limit is $0.1M_{\odot}$ as the initial mass function of the globular cluster.

4.4 Results

In the first and second columns of table 4.1, I summarize the number of high-velocity single escapers $n_{\text{hv},s}$ and binary escapers $n_{\text{hv},b}$ per initial half-mass relaxation time in my cluster models, which are obtained from figure 3.20 and figure 3.21. The initial half-mass relaxation time in my cluster models is 200 in N -body time unit, and I assume that escape velocities of the high-velocity single escapers are more than 1 in N -body unit, and all binary escapers have high velocity. In the third column of table 4.1, I describe T_{sim} .

Using the distribution of the binding energies of the ejected binaries (figure 3.24), I estimate the fraction of the DNSs which merge within a Hubble time in the total DNSs, f_{gw} . The time until the DNSs merge through gravitational wave radiation is expressed as

$$t_{\text{gw}} = 1 \times 10^{18} \left(\frac{m_{\text{DNS}}}{1M_{\odot}} \right)^{-3} \left(\frac{a}{1\text{AU}} \right)^4 g(e) \text{years}, \quad (4.9)$$

where m_{DNS} is the total mass of the DNS, typically $2.8M_{\odot}$, a is the semi-major axis of the DNS, e is the eccentricity of the DNS, and $g(e)$ is expressed as

$$g(e) = \frac{(1 - e^2)^{7/2}}{1 + (73/24)e^2 + (37/96)e^4}. \quad (4.10)$$

When a is less than 0.02AU, t_{gw} is less than a Hubble time, $\sim 10^{10}$ years, even if $e = 0$. On the other hand, the semi-major axis is expressed as

$$a = 2 \times 10^{-2} \left(\frac{r_v}{3\text{pc}} \right) \left(\frac{x}{100kT} \right)^{-1} \left(\frac{N}{10^6} \right) \text{AU}, \quad (4.11)$$

where r_v is the virial radius of the cluster, and x is the binding energy of the binary in the unit of kT . Therefore, when the cluster has 3pc virial radius, and $N = 10^6$, which is typical globular cluster, DNSs with more than $100kT$ merge within a Hubble time. Since from figure 3.24 the binding energies of most ejected binaries are more than $100kT$, $f_{\text{gw}} = 1$ in all my cluster models as seen in the fourth column of table 4.1.

In the fifth column of table 4.1, I describe the number of the DNSs which merge within a Hubble time in my cluster models when I scale my cluster models to those with 3pc virial radii and $N = 10^6$. Since in all my cluster models, neutron stars are completely depleted, I apply the lower expression of equation (4.6) for DNS merger rate per a globular cluster, N_{DNS} . From table 4.1, the DNSs which merge within a Hubble time are 140 – 280 per one globular cluster, and have little dependence on the distributions of the binding energies of the primordial binaries. The DNSs which merge within a Hubble time depend on the number of the neutron stars retained by the globular clusters.

Since about 150 globular clusters are in our Galaxy, about 3×10^4 DNSs which merge within a Hubble time are in our Galaxy. This DNS merger rate in our Galaxy is comparable to Kim et al. (2005)'s estimate from observed DNSs that the DNS merger rate is about 15 per 10^6 years. The DNS merger rate in our Galaxy constrained by the observations can be almost explained only by the dynamical formation of the DNSs in the galactic globular clusters without any binary evolution of progenitors of the neutron stars, such as tidal interactions, mass transfer, and common envelop evolution (e.g. Belczynski et al. 2007).

4.5 Comparison with previous works

The DNS merger rate per a globular cluster in my estimate is larger than Grindlay et al. (2006)'s, and Ivanova et al. (2008)'s estimates by two and three order and of magnitudes, respectively. The discrepancy between Grindlay et al. (2006)'s and our results arises from the number of progenitors of DNSs. They assumed that the progenitors are only binaries consisting of one neutron star and one other star, not binaries consisting of other than neutron stars. Furthermore, the binaries with one neutron star are typically 20 in each massive globular cluster. The numbers of the progenitors in each massive globular cluster seems lower limits.

The discrepancy between Ivanova et al. (2008)'s and our results comes from the modellings of mass segregation. In the modelling of mass segregation of Ivanova et al. (2008), mass segregation weakens. The neutron stars are not concentrated in the cluster core. The encounters involving neutron stars become small. Therefore, the number of DNSs formed in the clusters is small.

Table 4.1: The number of high-velocity single and binary escapers at each initial half-mass relaxation time, $n_{\text{hv},s}$ and $n_{\text{hv},b}$, the simulation time in the unit of the initial half-mass relaxation time, T_{sim} , a fraction of double neutron stars (DNS) which merge within a Hubble time in total DNS, and the number of DNS which merge within a Hubble time in one typical globular cluster.

| Model name | $n_{\text{hv},s}$ | $N_{\text{hv},b}$ | T_{sim} | f_{gw} | N_{DNS} |
|-----------------|-------------------|-------------------|------------------|-----------------|------------------|
| No-binary | 4.9 | 1.0 | 25 | 1 | 140 |
| $1kT_0 - 0.1$ | 5.7 | 1.4 | 25 | 1 | 160 |
| $3kT_0 - 0.1$ | 8.9 | 2.1 | 28 | 1 | 160 |
| $10kT_0 - 0.1$ | 9.3 | 2.2 | 23 | 1 | 160 |
| $30kT_0 - 0.1$ | 15 | 3.7 | 19 | 1 | 170 |
| $100kT_0 - 0.1$ | 18 | 9.6 | 15 | 1 | 260 |
| $300kT_0 - 0.1$ | 17 | 11 | 12 | 1 | 280 |

Chapter 5

Summary

I develop a new N -body simulation code equipped with special treatments for binaries, whose name is GORILLA. By means of GORILLA, we can follow the evolution of clusters within the energy error $\sim 1\%$ during few relaxation time after gravothermal core collapse. The structural parameter of the clusters (for example Lagrange radii) are not affected very much by the energy error up to 10% . My results by means of GORILLA agrees with Anders et al. (2007), who have performed the same simulations as mine by means of NBODY4 and kira.

I study systematically the dependence of cluster evolution on the binding energy of primordial binaries. By means of GORILLA, I simulate the core evolution of the clusters, each of which contains primordial binaries with equal binding energy.

I find that in both soft (models $1kT_0-0.1$, and $3kT_0-0.1$) and hard ($300kT_0-0.1$) hardness, the clusters experiences deep core collapse. In models $1kT_0-0.1$, and $3kT_0-0.1$, the ratios of the core radii to the half-mass radii are 0.002 at the halt of core collapse, and in model $300kT_0-0.1$ the ratios are 0.02 . On the other hand, in models $10kT_0-0.1$, $30kT_0-0.1$, and $100kT_0-0.1$, core collapse stops halfway, and the ratios of the core radii to the half-mass radii are $0.05-0.1$ at that time. The depth of the core collapse depends on the amount of energy heating core generated by the primordial binaries.

The amount of the energy heating the core depends on whether the binaries can become harder or not through binary-single and binary-binary encounters, and whether the single stars and binaries heated by such encounters are ejected or not from the clusters. In model $1kT_0-0.1$, the primordial binaries are destroyed through encounters, and can not heat the core. In model $3kT_0-0.1$, the primordial binaries heat the core, but it makes the time to the core collapse longer, compared to the case without primordial binaries, since that heating is not so large to stop core collapse. In models $10kT_0-0.1$, $30kT_0-0.1$, and $100kT_0-0.1$, the primordial binaries continually heat the core, and becomes harder and harder. In model $300kT_0-0.1$, the kinetic energy transformed from binding energy of primordial binaries through encounters is so large to be ejected from whole cluster immediately, and the primordial binaries can not heat the

core.

I theoretically estimate the ratio of core radius to half-mass radius at the halt of core collapse. I compare the theoretical estimate with my simulation results. In models $10kT_0 - 0.1$, $30kT_0 - 0.1$, $100kT_0 - 0.1$, and $300kT_0 - 0.1$, my simulation results are in good agreement with the theoretical estimates. In models $1kT_0 - 0.1$, and $3kT_0 - 0.1$, the ratios are much larger than those of theoretical estimates, since the core collapse stops due to energy heating core generated by the three-body binaries in these models.

After the halt of the core contraction, the core radii slightly decrease in models $10kT_0 - 0.1$ and $30kT_0 - 0.1$, and is not changed in model $100kT_0 - 0.1$, while the half-mass radii in these models are expanding. The decrease of the ratio of the core radii to the half-mass radii is due to the overall hardening of the binaries which comes from the decrease of the average stellar kinetic energy. The slight decrease of the core radii in models $10kT_0 - 0.1$ and $30kT_0 - 0.1$ is due to the hardening of the binaries through binary-single and binary-binary encounters.

I also investigate the dependence of cluster evolution on the initial mass fraction of the primordial binaries, $f_{b,0}$. I find that core collapse stops halfway in model $3kT_0 - 0.3$, in contrast to model $3kT_0 - 0.1$. This is because more primordial binaries in model $3kT_0 - 0.3$ becomes harder than those in model $3kT_0 - 0.1$. The ratios of the core radii to the half-mass radii in models $30kT_0 - 0.1$ (0.09), and $30kT_0 - 0.1$ (0.1) are two times larger than that in models $30kT_0 - 0.03$ (0.05). The ratios in the $E_{\text{bin},0} = 300kT_0$ are similar, and 0.02–0.03. These ratios are in good agreement with the theoretical estimates.

From the high-velocity single and binary escapers in my simulations, I estimate the merger rate of double neutron stars (DNSs) which are formed in one globular clusters. The number of the DNSs which merge within a Hubble time are about 200, which does not depend on the initial distributions of the binding energies of the primordial binaries. Since 150 globular clusters are in our Galaxy, about 3×10^4 DNSs merge within a Hubble time in our Galaxy, which is comparable to Kim et al. (2005)'s estimates from the observations of the DNSs. The DNS merger rate in our Galaxy constrained by the observations is almost explained only by the dynamical formation of the DNSs in the galactic globular clusters without any binary evolution, such as tidal interactions, mass transfer, and common envelop evolution (e.g. Belczynski et al. 2007).

Appendix A

Algorithm of GORILLA

I describe step-by-step the algorithm of the time integrator part in section A.1, and that of GORIMO in section A.2.

A.1 Time integrator part

For the time integrator part, I adopt the fourth-order Hermite integrator with individual timestep scheme (Makino, Aarseth 1992), and block timestep scheme (McMillan 1986). Indexes are attached to all the particles. In the time integrator part, particle i has its own time, t_i , its timestep, Δt_i , mass, m_i , position, \mathbf{r}_i , and, velocity, \mathbf{v}_i , at time t_i , and acceleration, \mathbf{a}_i , and first-order time derivative of acceleration, \mathbf{j}_i ($= d\mathbf{a}_i/dt$), calculated at time t_i . Since I adopt the block timestep scheme, $\Delta t_i = \Delta t_{\max}/2^{q-1}$, where Δt_{\max} is the maximum timestep, and q is a positive integer.

In this part, particles not in isolation, the centers of mass of binaries which are in isolation but do not belong to any hierarchical triple system in isolation, and the centers of mass of hierarchical triple systems in isolation are integrated. As far as in this subsection, such particles and centers of mass are collectively called particles, and the list of these particles is called integration list.

In the time integrator part, the orbital motions of particles in the integration list are solved as follows.

Step 1 Search the integration list for the particles with a minimum $t_i + \Delta t_i$. Set the global time, t , to be this minimum, $t_i + \Delta t_i$. I put together all the particles with $t_i + \Delta t_i$ equal to t , and call them particles i .

Step 2 Predict the positions, $\mathbf{r}_{p,j}$, and the velocities, $\mathbf{v}_{p,j}$, of all the particles in the integration list at time t using \mathbf{r}_j , \mathbf{v}_j , \mathbf{a}_j , and \mathbf{j}_j . The formulas are as follows:

$$\mathbf{r}_{p,j} = \frac{(t - t_j)^3}{6} \mathbf{j}_j + \frac{(t - t_j)^2}{2} \mathbf{a}_j + (t - t_j) \mathbf{v}_j + \mathbf{r}_j \quad (\text{A.1})$$

and

$$\mathbf{v}_{p,j} = \frac{(t - t_j)^2}{2} \mathbf{j}_j + (t - t_j) \mathbf{a}_j + \mathbf{v}_j, \quad (\text{A.2})$$

where j runs through all particles in the integration list.

Step 3 Calculate the acceleration, \mathbf{a}_i , and its time derivative, \mathbf{j}_i , for particles i at time t , using the predicted positions and velocities, as follows:

$$\mathbf{a}_i = - \sum_j Gm_j \frac{\mathbf{r}_{ij}}{|\mathbf{r}_{ij}|^3} \quad (\text{A.3})$$

and

$$\mathbf{j}_i = - \sum_j Gm_j \left[\frac{\mathbf{v}_{ij}}{|\mathbf{r}_{ij}|^3} + \frac{3(\mathbf{v}_{ij} \cdot \mathbf{r}_{ij})\mathbf{r}_{ij}}{|\mathbf{r}_{ij}|^5} \right], \quad (\text{A.4})$$

where

$$\mathbf{r}_{ij} = \mathbf{r}_{p,i} - \mathbf{r}_{p,j}, \quad (\text{A.5})$$

$$\mathbf{v}_{ij} = \mathbf{v}_{p,i} - \mathbf{v}_{p,j}. \quad (\text{A.6})$$

Step 4 Calculate second-order time derivative, $\mathbf{s}_i (= d^2\mathbf{a}_i/dt^2)$, and third-order time derivative, $\mathbf{c}_i (= d^3\mathbf{a}_i/dt^3)$, of the acceleration, \mathbf{a}_i , using a Hermite interpolation as follows:

$$\mathbf{s}_{0,i} = \frac{-6(\mathbf{a}_{0,i} - \mathbf{a}_{1,i}) - \Delta t_i(4\mathbf{j}_{0,i} + 2\mathbf{j}_{1,i})}{\Delta t_i^2}, \quad (\text{A.7})$$

and

$$\mathbf{c}_{0,i} = \frac{12(\mathbf{a}_{0,i} - \mathbf{a}_{1,i}) + 6\Delta t_i(\mathbf{j}_{0,i} + \mathbf{j}_{1,i})}{\Delta t_i^3}, \quad (\text{A.8})$$

where the subscripts indicate the time at which the accelerations and the derivatives are evaluated. If they are '0', the time is t_i , and if they are '1', the time is $t_i + \Delta t_i$, i.e. the global time, t . Add the corrections to the positions and velocities of particles i as follows:

$$\mathbf{r}_i(t_i + \Delta t_i) = \mathbf{r}_{p,i} + \frac{\Delta t_i^4}{24} \mathbf{s}_{0,i} + \frac{\Delta t_i^5}{120} \mathbf{c}_{0,i}, \quad (\text{A.9})$$

and

$$\mathbf{v}_i(t_i + \Delta t_i) = \mathbf{v}_{p,i} + \frac{\Delta t_i^3}{6} \mathbf{s}_{0,i} + \frac{\Delta t_i^4}{24} \mathbf{c}_{0,i}. \quad (\text{A.10})$$

Step 5 Update t_i , and calculate the new timestep, $\Delta t_{1,i}$, given by

$$\Delta t_{1,i} = \begin{cases} 2\Delta t_{0,i} & (\Delta t_{\text{crit}} \geq 2\Delta t_{0,i}; t_i/(2\Delta t_{0,i}): \text{integer}) \\ \Delta t_{0,i} & (\Delta t_{\text{crit}} \geq 2\Delta t_{0,i}; t_i/(2\Delta t_{0,i}): \text{not integer}) \\ \Delta t_{\text{max}}/2^{q-1} & (\Delta t_{\text{crit}} < 2\Delta t_{0,i}) \end{cases} \quad (\text{A.11})$$

where $\Delta t_{0,i}$ is the old timestep, q is a positive integer satisfying $\Delta t_{\text{crit}}/2 < \Delta t_{\text{max}}/2^{q-1} \leq \Delta t_{\text{crit}}$, and Δt_{crit} is given by

$$\Delta t_{\text{crit}} = \sqrt{\eta \frac{|\mathbf{a}_{1,i}| |\mathbf{s}_{1,i}| + |\mathbf{j}_{1,i}|^2}{|\mathbf{j}_{1,i}| |\mathbf{c}_{1,i}| + |\mathbf{s}_{1,i}|^2}}, \quad (\text{A.12})$$

where η is accuracy parameter, $\mathbf{s}_{1,i} = \mathbf{s}_{0,i} + \Delta t_{0,i} \mathbf{c}_{0,i}$, and $\mathbf{c}_{1,i} = \mathbf{c}_{0,i}$.

Step 6 Send the global time, t , and all the particle data to GORIMO.

Step 7 Receive data from GORIMO.

Step 8 Go to step 1.

A.2 GORIMO

In this subsection, I describe the procedures of the special treatments for binaries, which proceed in GORIMO. The tasks of GORIMO are divided into three. First is to change two particles into those in isolation, second is the inversion of the first special treatment, and third is to send the information on the outcome of the first and second special treatments to the time integrator part, whose procedures are described in step 6-1, 6-2, and 6-3, respectively.

Step 6-1

Step 6-1.1 Search the integration list for pairs of two particles (or the center of mass of two particles in isolation and one particles) isolated enough, and with the times equal to the global time, t . If such pairs exist, I proceed to step 6-1.2, otherwise to step 6-2. Such pairs satisfy either isolation conditions as follows, and hereafter the indexes of the two particles (or the center of mass of two particles in isolation and one particles) in such pairs are set to be k and l .

Isolation conditions (A)

1. $E_{\text{bin},kl} > 1kT_0$
2. $|\mathbf{r}_3 - \mathbf{r}_{\text{cm},kl}| > \alpha r_{\text{apo},kl}$
3. $r_{\text{peri},kl} > \alpha \max(s_k, s_l)$

Isolation conditions (B) (only for pairs of two particles)

1. Do not satisfy isolation conditions (A), and $E_{\text{bin},kl} > 0$
2. $e_{kl} > 0.95$
3. $|\mathbf{r}_3 - \mathbf{r}_{\text{cm},kl}| > \beta \mathbf{r}_{\text{rel},kl}$
4. $\mathbf{r}_{\text{rel},kl} \cdot \mathbf{v}_{\text{rel},kl} \leq 0$

Isolation conditions (C) (only for pairs of two particles)

1. $E_{\text{bin},kl} \leq 0$
2. $\Delta t_k \leq \Delta t_{\text{max}}/2^{36}$ and $\Delta t_l \leq \Delta t_{\text{max}}/2^{36}$

3. $|\mathbf{r}_3 - \mathbf{r}_{\text{cm},kl}| > \beta \mathbf{r}_{\text{rel},kl}$
4. $\mathbf{r}_{\text{rel},kl} \cdot \mathbf{v}_{\text{rel},kl} \leq 0$

Here, $E_{\text{bin},kl}$ is the binding energy of particles k and l , expressed as

$$E_{\text{bin},kl} = - \left(\frac{1}{2} \frac{m_k m_l}{m_k + m_l} |\mathbf{v}_{\text{rel},kl}|^2 - \frac{G m_k m_l}{|\mathbf{r}_{\text{rel},kl}|} \right), \quad (\text{A.13})$$

where $\mathbf{v}_{\text{rel},kl} = \mathbf{v}_k - \mathbf{v}_l$. Here, \mathbf{r}_3 is the position of the nearest particle (or center of mass of two particles and hierarchical triple systems in isolation) from the center of mass of particles k and l , $\mathbf{r}_{\text{cm},kl}$. The separations between particles k and l at the apocenter, $r_{\text{apo},kl}$, and pericenter, $r_{\text{peri},kl}$, are, respectively, expressed as

$$r_{\text{apo},kl} = a_{kl}(1 + e_{kl}), \quad (\text{A.14})$$

and

$$r_{\text{peri},kl} = a_{kl}(1 - e_{kl}), \quad (\text{A.15})$$

where a_{kl} is the semi-major axis of particles k and l , expressed as

$$a_{kl} = \frac{G m_k m_l}{2|E_{\text{bin},kl}|}, \quad (\text{A.16})$$

and e_{kl} is the eccentricity of particles k and l , expressed as

$$e_{kl} = \sqrt{1 - \frac{E_{\text{bin},kl} |\mathbf{r}_{\text{rel},kl} \times \mathbf{v}_{\text{rel},kl}|}{G^2 m_k m_l (m_k + m_l)}}. \quad (\text{A.17})$$

Here, s_i ($i = k, l$) is the size of particle (or center of mass of two particles and hierarchical triple system) i . Particle i has $s_i = 0$, and the center of mass of two particles in isolation has s_i equal to the separation at the apocenter between the two particles. Through dimensionless quantities α (called apocentric parameter) and β (called pericentric parameter), I decide the strictness of isolation. I discuss appropriate apocentric and pericentric parameters in subsection 2.2.

Step 6-1.2 Calculate the data of the center of mass of all the pairs satisfying either isolation conditions, which are required for the time integrator part. The data of each center of mass are the time, $t_{\text{cm},kl}$, timestep, $\Delta t_{\text{cm},kl}$, mass, $m_{\text{cm},kl}$, position, $\mathbf{r}_{\text{cm},kl}$, velocity, $\mathbf{v}_{\text{cm},kl}$, acceleration, $\mathbf{a}_{\text{cm},kl}$, and first-order time derivative of the acceleration, $\mathbf{j}_{\text{cm},kl}$. The time, $t_{\text{cm},kl}$, mass, $m_{\text{cm},kl}$, and velocity, $\mathbf{v}_{\text{cm},kl}$, are, respectively, expressed as

$$t_{\text{cm},kl} = t, \quad (\text{A.18})$$

$$m_{\text{cm},kl} = m_k + m_l, \quad (\text{A.19})$$

and

$$\mathbf{v}_{\text{cm},kl} = \frac{m_k \mathbf{v}_k + m_l \mathbf{v}_l}{m_k + m_l}. \quad (\text{A.20})$$

The position, $\mathbf{r}_{\text{cm},kl}$, is calculated as equation (2.2). The acceleration, $\mathbf{a}_{\text{cm},kl}$, and the first-order time derivative of the acceleration, $\mathbf{j}_{\text{cm},kl}$, are calculated in the same way as \mathbf{a}_i and \mathbf{j}_i in step 3. The timestep, $\Delta t_{\text{cm},kl}$, is expressed as

$$\Delta t_{\text{cm},kl} = \begin{cases} \min(\Delta t_k, \Delta t_l) & (\Delta t_{\text{crit},s} \geq \min(\Delta t_k, \Delta t_l)) \\ \Delta t_{\text{max}}/2^{q-1} & (\Delta t_{\text{crit},s} < \min(\Delta t_k, \Delta t_l)) \end{cases}, \quad (\text{A.21})$$

where q is a positive integer satisfying $\Delta t_{\text{crit},s}/2 < \Delta t_{\text{max}}/2^{q-1} \leq \Delta t_{\text{crit},s}$, and $\Delta t_{\text{crit},s}$ is given by

$$\Delta t_{\text{crit},s} = \eta_s \frac{|\mathbf{a}_{\text{cm},kl}|}{|\mathbf{j}_{\text{cm},kl}|}. \quad (\text{A.22})$$

Here, η_s is start-up accuracy parameter.

Step 6-1.3 Keep the data of the particles in all the pairs in GORIMO. The data of the particles in each pair are as follows.

- The time of particles k and l (t_k and t_l).
- The mass of particles k and l (m_k and m_l).
- The relative position, $\mathbf{r}_{\text{rel},kl}$, and the relative velocity, $\mathbf{v}_{\text{rel},kl}$ of particles k and l at the current time, t .
- The name of the isolation conditions satisfied by particles k and l .

Step 6-2

Step 6-2.1 List the centers of mass of two particles and hierarchical triple systems in isolation with the times equal to the global time, t , and operate each center of mass according to the following steps. Hereafter, the indexes of particles of which each center of mass is composed are k and l .

Step 6-2.2 Calculate the relative position, $\mathbf{r}_{\text{rel},kl}$, and the relative velocity, $\mathbf{v}_{\text{rel},kl}$, of particles k and l at the current time, t , by solving equation (2.7) as follows.

Step 6-2.2.1 Calculate the eccentric anomaly, u_{kl} , of particles k and l at the current time t , solving Kepler equation expressed as

$$\begin{cases} u_{kl} - e_{kl} \sin u_{kl} = \sqrt{\frac{G(m_k + m_l)}{a_{kl}^3}}(t - t_{\text{peri},kl}) & (E_{\text{bin},kl} > 0) \\ e_{kl} \sinh u_{kl} - u_{kl} = \sqrt{\frac{G(m_k + m_l)}{a_{kl}^3}}(t - t_{\text{peri},kl}) & (E_{\text{bin},kl} < 0) \end{cases}, \quad (\text{A.23})$$

where a_{kl} is the semi-major axis, e_{kl} is the eccentricity, and $t_{\text{peri},kl}$ is the nearest time at the passage of the pericenter from the time t_0 when particles k and l have been in isolation. I obtain

a_{kl} , and e_{kl} , using the relative position, $\mathbf{r}_{\text{rel},0,kl}$ and the relative velocity $\mathbf{v}_{\text{rel},0,kl}$ between particles k and l at the time t_0 according to equation (A.16) and (A.17). I obtain $t_{\text{peri},kl}$, according to the following expression:

$$t_{\text{peri},kl} = \begin{cases} t_0 - \sqrt{\frac{a_{kl}^3}{G(m_k + m_l)}} (u_{0,kl} - e_{kl} \sin u_{0,kl}) \\ \quad (E_{\text{bin},kl} > 0) \\ t_0 - \sqrt{\frac{a_{kl}^3}{G(m_k + m_l)}} (e_{kl} \sinh u_{0,kl} - u_{0,kl}) \\ \quad (E_{\text{bin},kl} < 0) \end{cases}, \quad (\text{A.24})$$

where $u_{0,kl}$ is the eccentric anomaly at the time t_0 , given by

$$u_{0,kl} = \begin{cases} \arccos [(1 - |\mathbf{r}_{\text{rel},0,kl}|/a_{kl})/e_{kl}] \\ \quad (E_{\text{bin},kl} > 0, \mathbf{r}_{\text{rel},0,kl} \cdot \mathbf{v}_{\text{rel},0,kl} > 0) \\ -\arccos [(1 - |\mathbf{r}_{\text{rel},0,kl}|/a_{kl})/e_{kl}] \\ \quad (E_{\text{bin},kl} > 0, \mathbf{r}_{\text{rel},0,kl} \cdot \mathbf{v}_{\text{rel},0,kl} < 0) \\ \cosh^{-1} [(1 - |\mathbf{r}_{\text{rel},0,kl}|/a_{kl})/e_{kl}] \\ \quad (E_{\text{bin},kl} < 0) \end{cases}. \quad (\text{A.25})$$

The solution methods of the Kepler equation are an iterative method of Kepler equation (e.g. Murray, Dermott 1999) when $E_{\text{bin},kl} > 0$, and Newton's method when $E_{\text{bin},kl} < 0$. I stop the iteration if $|X_n - X_{n-1}| < 10^{-6}[\text{rad}]$, and decide X_n as the solution, where X_n is n -th order approximation of the solution.

Step 6-2.2.2 Calculate the relative position, $\mathbf{r}_{\text{rel},kl}^* = (x_{kl}^*, y_{kl}^*)$, and the relative velocity, $\mathbf{v}_{\text{rel},kl}^* = (v_{x,kl}^*, v_{y,kl}^*)$, between particles k and l at the current time t , where figure A.1 shows the coordinate system of (x^*, y^*) . They are given by

$$x_{kl}^* = \begin{cases} a_{kl}(\cos u_{kl} - e_{kl}) & (E_{\text{bin},kl} > 0) \\ -a_{kl}(\cosh u_{kl} - e_{kl}) & (E_{\text{bin},kl} < 0) \end{cases}, \quad (\text{A.26})$$

$$y_{kl}^* = \begin{cases} a_{kl} \sqrt{1 - e_{kl}^2} \sin u_{kl} & (E_{\text{bin},kl} > 0) \\ a_{kl} \sqrt{e_{kl}^2 - 1} \sinh u_{kl} & (E_{\text{bin},kl} < 0) \end{cases}, \quad (\text{A.27})$$

$$v_{x,kl}^* = \begin{cases} -\frac{\sin u_{kl}}{1 - e_{kl} \cos u_{kl}} \sqrt{\frac{G(m_k + m_l)}{a_{kl}}} & (E_{\text{bin},kl} > 0) \\ \sinh u_{kl} \sqrt{\frac{Ga_{kl}(m_k + m_l)}{x_{kl}^{*2} + y_{kl}^{*2}}} & (E_{\text{bin},kl} < 0) \end{cases}, \quad (\text{A.28})$$

and

$$v_{y,kl}^* = \begin{cases} \frac{\cos u_{kl}}{1 - e_{kl} \cos u_{kl}} \sqrt{\frac{G(m_k + m_l)(1 - e_{kl}^2)}{a_{kl}}} & (E_{\text{bin},kl} > 0) \\ \cosh u_{kl} \sqrt{\frac{G a_{kl} (m_{kl} + m_l)(e_{kl}^2 - 1)}{x_{kl}^{*2} + y_{kl}^{*2}}} & (E_{\text{bin},kl} < 0) \end{cases} \quad (\text{A.29})$$

Step 6-2.2.3 Rotate the coordinate of the relative position and velocity of particle k and l from $\mathbf{r}_{\text{rel},kl}^*$ and $\mathbf{v}_{\text{rel},kl}^*$ to $\mathbf{r}_{\text{rel},kl}$ and $\mathbf{v}_{\text{rel},kl}$ as follows:

$$\mathbf{r}_{\text{rel},kl} = \mathbf{R}_z(-\Omega_{kl})\mathbf{R}_x(-I_{kl})\mathbf{R}_z(-\omega_{kl})\mathbf{r}_{\text{rel},kl}^* \quad (\text{A.30})$$

and

$$\mathbf{v}_{\text{rel},kl} = \mathbf{R}_z(-\Omega_{kl})\mathbf{R}_x(-I_{kl})\mathbf{R}_z(-\omega_{kl})\mathbf{v}_{\text{rel},kl}^*, \quad (\text{A.31})$$

where $R_x(\theta)$ and $R_z(\theta)$ are, respectively, the matrices rotating vectors by θ around x and z axes expressed as

$$\mathbf{R}_x(\theta) = \begin{pmatrix} 1 & 0 & 0 \\ 0 & \cos \theta & \sin \theta \\ 0 & -\sin \theta & \cos \theta \end{pmatrix}, \quad (\text{A.32})$$

and

$$\mathbf{R}_z(\theta) = \begin{pmatrix} \cos \theta & \sin \theta & 0 \\ -\sin \theta & \cos \theta & 0 \\ 0 & 0 & 1 \end{pmatrix}. \quad (\text{A.33})$$

Here, I_{kl} , Ω_{kl} , and ω_{kl} are the inclination, longitude of the ascending node, and argument of the pericenter with respect to the cluster, shown in figure A.2. They are conservative quantities, and obtained using $\mathbf{r}_{\text{rel},0,kl} = (x_0, y_0, z_0)$ and $\mathbf{v}_{\text{rel},0,kl} = (v_{x,0}, v_{y,0}, v_{z,0})$. The inclination, I_{kl} , is expressed as

$$I_{kl} = \arccos \left(\frac{h_{z,kl}}{|\mathbf{h}_{kl}|} \right), \quad (\text{A.34})$$

where $\mathbf{h}_{kl} = (h_{x,kl}, h_{y,kl}, h_{z,kl})$ is the angular momentum of particles k and l , given by

$$\mathbf{h}_{kl} = \mathbf{r}_{\text{rel},0,kl} \times \mathbf{v}_{\text{rel},0,kl}. \quad (\text{A.35})$$

The longitude of the ascending node, Ω_{kl} , is expressed as

$$\Omega_{kl} = \begin{cases} \arccos [-h_{y,kl}/(|\mathbf{h}_{kl}| \sin I_{kl})] & [h_{x,kl}/(|\mathbf{h}_{kl}| \sin I_{kl}) > 0] \\ -\arccos [-h_{y,kl}/(|\mathbf{h}_{kl}| \sin I_{kl})] & [h_{x,kl}/(|\mathbf{h}_{kl}| \sin I_{kl}) < 0] \end{cases}. \quad (\text{A.36})$$

The argument of the pericenter, ω_{kl} , is expressed as

$$\omega_{kl} = \begin{cases} \arccos \left\{ \frac{[|\mathbf{h}_{kl}|/G(m_k + m_l)] \bar{v}_{y,0} - \bar{x}_0/|\mathbf{r}_{\text{rel},0,kl}|}{e_{kl}} \right\} \\ \left(\frac{[|\mathbf{h}_{kl}|/G(m_k + m_l)] \bar{v}_{x,0} + \bar{y}_0/|\mathbf{r}_{\text{rel},0,kl}|}{e_{kl}} < 0 \right) \\ - \arccos \left\{ \frac{[|\mathbf{h}_{kl}|/G(m_k + m_l)] \bar{v}_{y,0} - \bar{x}_0/|\mathbf{r}_{\text{rel},0,kl}|}{e_{kl}} \right\} \\ \left(\frac{[|\mathbf{h}_{kl}|/G(m_k + m_l)] \bar{v}_{x,0} + \bar{y}_0/|\mathbf{r}_{\text{rel},0,kl}|}{e_{kl}} > 0 \right) \end{cases}, \quad (\text{A.37})$$

where (\bar{x}_0, \bar{y}_0) and $(\bar{v}_{x,0}, \bar{v}_{y,0})$ are the relative position and velocity between particle k and l in the coordinate system on the orbital plane in which \bar{x} axis is oriented in the direction from particle l to the ascending node, shown in figure A.2, and \bar{y} axis is perpendicular to \bar{x} axis. Here, \bar{x}_0 , \bar{y}_0 , $\bar{v}_{x,0}$, and $\bar{v}_{y,0}$ are given by

$$\bar{x}_0 = x_0 \cos \Omega_{kl} + y_0 \sin \Omega_{kl}, \quad (\text{A.38})$$

$$\bar{y}_0 = (-x_0 \cos \Omega_{kl} + y_0 \sin \Omega_{kl}) \cos I_{kl} + z_0 \sin I_{kl}, \quad (\text{A.39})$$

$$\bar{v}_{x,0} = v_{x,0} \cos \Omega_{kl} + v_{y,0} \Omega_{kl}, \quad (\text{A.40})$$

and

$$\bar{v}_{y,0} = (-v_{x,0} \sin \Omega_{kl} + v_{y,0} \cos \Omega_{kl}) \cos I_{kl} + v_{z,0} \sin I_{kl}. \quad (\text{A.41})$$

Step 6-2.3 Transform $\mathbf{r}_{\text{cm},kl}$ and $\mathbf{r}_{\text{rel},kl}$ to \mathbf{r}_k and \mathbf{r}_l as follows:

$$\mathbf{r}_k = \mathbf{r}_{\text{cm},kl} + \frac{m_l}{m_k + m_l} \mathbf{r}_{\text{rel},kl}, \quad (\text{A.42})$$

and

$$\mathbf{r}_l = \mathbf{r}_{\text{cm},kl} - \frac{m_k}{m_k + m_l} \mathbf{r}_{\text{rel},kl}, \quad (\text{A.43})$$

and $\mathbf{v}_{\text{cm},kl}$ and $\mathbf{v}_{\text{rel},kl}$ to \mathbf{v}_k and \mathbf{v}_l as follows:

$$\mathbf{v}_k = \mathbf{v}_{\text{cm},kl} + \frac{m_l}{m_k + m_l} \mathbf{v}_{\text{rel},kl}, \quad (\text{A.44})$$

and

$$\mathbf{v}_l = \mathbf{v}_{\text{cm},kl} - \frac{m_k}{m_k + m_l} \mathbf{v}_{\text{rel},kl}, \quad (\text{A.45})$$

where $\mathbf{r}_{\text{cm},kl}$ and $\mathbf{v}_{\text{cm},kl}$ are sent from the time integrator part.

Step 6-2.4 Judge whether particles k and l satisfy the isolation conditions satisfied by them at the time t_0 . If they satisfy the isolation conditions, I proceed to step 6-3, otherwise to step 6-2.4.

Step 6-2.5 Calculate the data of particle k and l . The data are the times (t_k and t_l), the timesteps (Δt_k and Δt_l), acceleration (\mathbf{a}_k and \mathbf{a}_l), and first-order time derivative of the acceleration (\mathbf{j}_k and \mathbf{j}_l), which I obtain in the same way as those of the center of mass of particles k and l in step 6-1.1.

Step 6-3 Send the data of the particles and centers of mass in the integration list to the time integrator part.

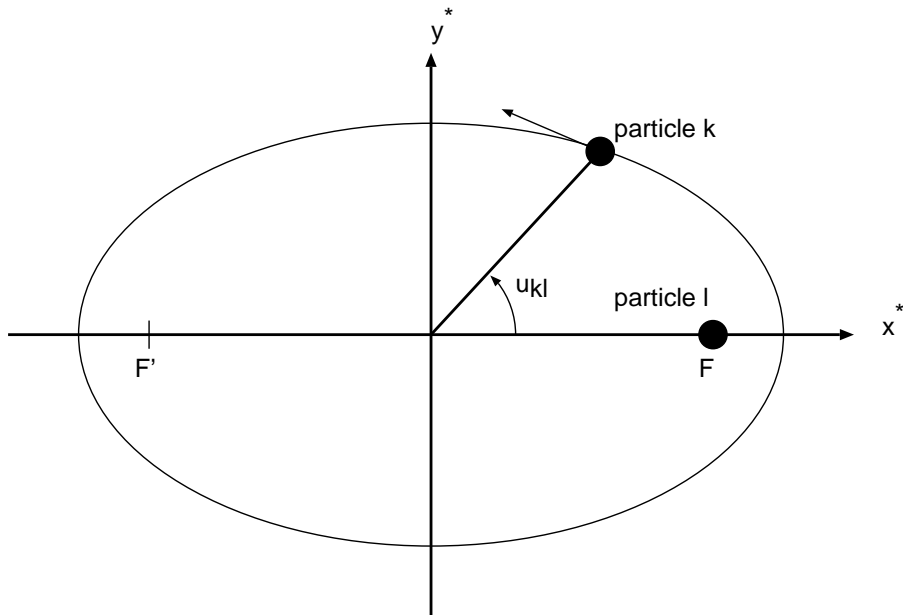


Figure A.1: The orbital plane of the relative motion between particles k and l . The elliptic curve shows the relative orbit of particle k with respect to particle l . Coordinate system of (x^*, y^*) is set, such that the origin is put on the middle point between two focus (F , and F') of the orbital ellipse, the two focus are on x^* axis which is oriented the pericenter of the orbit of particle k , and y^* is oriented in the direction of the velocity of particle k at the pericenter. The angle between x^* axis and the line from the origin to particle k is eccentric anomaly, u_{kl} .

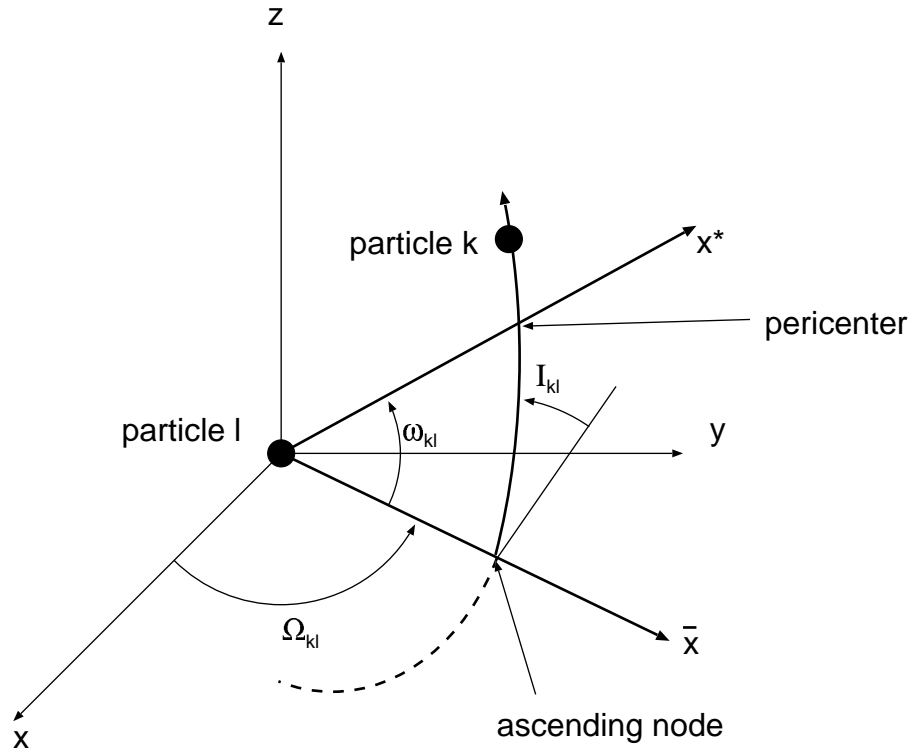


Figure A.2: The relative motion of particle k with respect to particle l in coordinate system (x, y, z) whose origin is put on particle l . The angle between $x - y$ plane and the orbital plane is called inclination, denoted by I_{kl} . Two coordinate systems (\bar{x}, \bar{y}) and (x^*, y^*) are set on the orbital plane. The \bar{x} axis is oriented from the origin in the direction of the ascending node of particle k . The angle between the x and \bar{x} axes is called longitude of ascending node, denoted by Ω_{kl} . The x^* axis is oriented from the origin in the direction of the pericenter of particle k . The angle between the \bar{x} and x^* axes is called argument of pericenter, denoted by ω_{kl} .

Bibliography

- [1] Aarseth, S. 1963, Monthly Notices of the RAS, 126, 223
- [2] Aarseth, S. 1971, Astronomy and Astrophysics Supplement, 13, 324
- [3] Aarseth, S. 1975, IAU Circulars, 69, 57
- [4] Aarseth, S. 1980, IAU Circulars, 85, 325
- [5] Aarseth, S. 2003, Gravitational N -body Simulations (Cambridge: Cambridge University Press), ch.2
- [6] Aarseth, S., & Heggie, D. C. 1993, Astronomical Society of the Pacific Conference Series, 48, 701
- [7] Anders, P., Lamers, H. J. G. L. M. & Baumgardt, H. 2008, IAU Circulars, 246, 187
- [8] Antonov, V. A. 1962, Vestnik Leningradskogo Universiteta, 7, 135
- [9] Baumgardt, H., & Makino, J. 2003, Monthly Notices of the RAS, 340, 227
- [10] Baumgardt, H., Makino, J., & Ebisuzaki, T. 2004, Astrophysical Journal, 613, 1143
- [11] Baumgardt, H., Makino, J., & Hut, P. 2005, Astrophysical Journal, 620, 238
- [12] Belczynski, K., Taam, R. E., Kalogera, V., Rasio, F. A., & Bulik, T. 2007, Astrophysical Journal, 662, 504
- [13] Belczynski, K., Kalogera, V., Rasio, F. A., Taam, R. E., Zezas, A., Bulik, T., Maccarone, T. J., & Ivanova, N. 2008, Astrophysical Journal, 174, 223
- [14] Bettwieser, E., & Sugimoto, D. 1983, Monthly Notices of the RAS, 208, 493
- [15] Casertano, S., & Hut, P. 1985 Astrophysical Journal, 298, 80
- [16] Cohn, H. 1980, Astrophysical Journal, 242, 765

- [17] Cohn, H., Hut, P., & Wise, M. 1989, *Astrophysical Journal*, 342, 814
- [18] Fregeau, J. M., Gurkan, M. A., Joshi, K. J., & Rasio, F. A. 2003, *Astrophysical Journal*, 593, 772
- [19] Fregeau, J. M., & Rasio, F. A. 2006, astro-ph/0608261
- [20] Fukushige, T., Makino, J., & Kawai, A. 2005, *Publications of the ASJ*, 57, 1009
- [21] Gao, B., Goodman, J., Cohn, H., & Murphy, B. 1991, *Astrophysical Journal*, 370, 567
- [22] Giannone, G., & Molteni, D. 1985, *Astronomy and Astrophysics*, 143, 321
- [23] Giersz, M., & Spurzem, R. 2000, *Monthly Notices of the RAS*, 317, 581
- [24] Giersz, M., & Spurzem, R. 2003, *Monthly Notices of the RAS*, 343, 781
- [25] Goodman, J., & Hut, P. 1989, *Nature*, 339, 40 (GH89)
- [26] Grindlay, J., Portegies Zwart, S., & McMillan, S. L. W. 2006, *Nature*, 2, 116
- [27] Gunn, J. E., & Griffin, R. F. 1979, *Astronomical Journal*, 84, 752
- [28] Hachisu, I, & Sugimoto, D. 1978, *Progress of Theoretical Physics*, 60, 1, 123
- [29] Harris, W., E. 1996, *Astronomical Journal*, 112, 1487
- [30] Harris, W., E. 2001, *Star clusters*, Saas-Fee Advanced Course 28. Lecture Notes 1998, Swiss Society for Astrophysics and Astronomy
- [31] Henon, M. 1975, *IAU Circulars*, 69, 133
- [32] Heggie, D. C. 1975, *Monthly Notices of the RAS*, 173, 729
- [33] Heggie, D. C., & Aarseth, S. 1992, *Monthly Notices of the RAS*, 257, 513
- [34] Heggie, D. C., & Hut, P. 1993, *Astrophysical Journal*, 85, 347
- [35] Heggie, D. C., & Mathieu, R. D. 1986, in *Lecture Notes in Physics Vol. 267*, ed. P. Hut & S. McMillan (Berlin: Springer-Verlag), 233
- [36] Heggie, D. C., Trenti, M., & Hut, P. 2006, *Astrophysical Journal*, 368, 677
- [37] Hut, P., & Bahcall, J. N. 1983, *Astrophysical Journal*, 268, 319
- [38] Ivanova, N., Heinke, C. O., Rasio, F. A., Belczynski, K., & Fregeau, J. M. 2008, *Monthly Notices of the RAS*, 386, 553
- [39] Kim, C., Kalogera, V., Lorimer, D. R., Ihm, M., & Belczynski, K. 2005, *ASP Conference Series*, 328, 83

- [40] King, I. 1966, *Astronomical Journal*, 71, 64
- [41] Kroupa, P. 2001, *Monthly Notices of the RAS*, 322, 231
- [42] Kroupa, P. 2002, *Science*, 295, 82
- [43] Kustaanheimo, P., & Stiefel, E. 1965, *J. Reine Angew. Math.*, 218, 204
- [44] Lynden-Bell, D., & Wood, R. 1968, *Monthly Notices of the RAS*, 138, 495
- [45] Makino, J. 1991, *Astrophysical Journal*, 369, 200
- [46] Makino, J. 1991, *Publications of the ASJ*, 43, 859 (Makino 1991b)
- [47] Makino, J. 1996, *Astrophysical Journal*, 471, 796
- [48] Makino, J., Fukushige, T., Koga, M., & Narumi, K. 2003, *Publications of the ASJ*, 55, 1163
- [49] Makino, J. & Aarseth, S. 1992, *Publications of the ASJ*, 44, 141
- [50] McMillan, S. L. W. 1986, *Astrophysical Journal*, 307, 126
- [51] McMillan, S. L. W., & Hut, P. 1996, *Astrophysical Journal*, 467, 348
- [52] McMillan, S. L. W., Hut, P., & Makino, J. 1990, *Astrophysical Journal*, 362, 522
- [53] McMillan, S. L. W., Hut, P., & Makino, J. 1991, *Astrophysical Journal*, 372, 111
- [54] Mikkola, S. 1983, *Monthly Notices of the RAS*, 203, 1107 (Mikkola 1983a)
- [55] Mikkola, S. 1983, *Monthly Notices of the RAS*, 205, 733 (Mikkola 1983b)
- [56] Mikkola, S., 1984a, *Monthly Notices of the RAS*, 207, 115 (Mikkola 1984a)
- [57] Mikkola, S., 1984a, *Monthly Notices of the RAS*, 208, 75 (Mikkola 1984b)
- [58] Miller, G. E., & Scalo, J. M. 1979, *Astrophysical Journal Supplement*, 41, 513
- [59] Murray, C. D., & Dermott, S. F. 1999, *Solar System Dynamics* (Cambridge:Cambridge University Press), 34
- [60] Nitadori, K., & Makino, J. 2008, *New Astronomy*, 13, 498
- [61] Portegies Zwart, S. F., McMillan, S. L. W., Hut, P. & Makino, J. 2001, *Monthly Notices of the RAS*, 321, 199
- [62] Shara, M. M., & Hurley, J. R. 2006, *Astrophysical Journal*, 646, 464
- [63] Spitzer, L. 1987, *Dynamical Evolution of Globular Clusters* (Princeton:Princeton University Press)

- [64] Spitzer, L., & Mathieu, R. D. 1980, *Astrophysical Journal*, 241, 618
- [65] Sugimoto, D., & Bettwieser, E. 1983, *Monthly Notices of the RAS*, 204, 19
- [66] Vesperini, E., & Chernoff, D. F. 1994, *Astrophysical Journal*, 431, 231
- [67] Wielen, R. 1974, in L.N. Mavridis (ed.), *Proceedings of the First European Astronomical Meeting (Athens 1972)*, Springer-Verlag, Berlin-Heidelberg-New York, 2, 326
- [68] Wielen, R. 1975, *IAU Circulars*, 69, 119